Post- and Pre-stack attribute analysis and inversion of Blackfoot 3Dseismic dataset

A Thesis Submitted to the College of

Graduate Studies and Research

in Partial Fulfillment of the

Requirements for the degree of

MASTER OF SCIENCE

in

Geophysics

Department of Geological Sciences

University of Saskatchewan

Saskatoon

by

Abdulsalam Swisi

PERMISSION TO USE

In presenting this thesis in partial fulfillment of the requirements for a postgraduate degree from the University of Saskatchewan, I agree that the libraries of this University may make it freely available for inspection. I further agree that permission for copying of this thesis in any manner, in whole or in part, for scholarly purposes may be granted by the professor who supervised my thesis work or, in his absence, by the department Head of the Department or the Dean of the College in which my thesis work was done. It is understood that any copy or publication or use of this thesis or parts thereof for financial gain shall not be allowed without my written permission. It is also understood that due recognition shall be given to me and to the University of Saskatchewan in any use which may be made of any material in my thesis.

Request for permission to copy or to make other use of material in this thesis in whole or part should be addressed to:

Head of the Department of Geological Sciences

114 Science Place

University of Saskatchewan

Saskatoon, Saskatchewan S7N 5E2

Abstract

The objective of this research is comparative analysis of several standard and one new seismic post- and pre-stack inversion methods and Amplitude Variation with Offset (AVO) attribute analysis in application to the CREWES Blackfoot 3D dataset. To prepare the data to the inversion, I start with processing the dataset by using ProMAX software. This processing, in general, includes static and refraction corrections, velocity analysis and stacking the data. The results show good quality images, which are suitable for inversion.

Five types of inversion methods are applied to the dataset and compared. Three of these methods produce solutions for the post-stack Acoustic Impedance (AI) and are performed by using the industry-standard Hampson-Russell software. The fourth method uses our in-house algorithm called SILC and implemented in IGeoS seismic processing system. In the fifth approach, the pre-stack gathers are inverted for elastic impedance by range-limited stacking of the common-midpoint (CMP) gathers in offsets and/or angles and then performing independent inversion of angle stack. Further, simultaneous inversion is applied to pre-stack seismic data to invert for both the *P*- and *S*-wave impedances. These impedances are used to extract the Lamé parameters multiplied by density (LMR), and used to extract the ratios between the *P*- and *S*-wave velocities. In addition, CMP gathers are used to produce AVO attribute images, which are good indicators of gas reservoirs. Finally, the results of the different inversion techniques are interpreted and correlated with well-log data and used to characterize the reservoir.

The different inversion results show clearly the reservoir with its related low impedance within the channel. The post-stack inversion gives the best results; in particular, the model-based inversion shows smoothed images of it while SILC provides a different, higher-resolution image. The elastic impedance also gives results similar to the post-stack inversion. Pre-stack inversion and AVO attributes give reasonable results in cross sections near the center of study area. In other areas, performance of pre-stack inversion is poorer, apparently because of reflection aperture limitations.

ACKNOWLEDGMENTS

SYMBOLS AND ABBREVIATIONS

Symbol	Definition
2D, 2-D	Two-Dimensional
3C	Three-Component
3D, 3-D	Three-Dimensional
A	Intercept (AVO attribute)
AGC	Automatic Gain Control (trace equalization procedure)
AI	Acoustic Impedance; in simultaneous inversion, also denoted Z_P
AVA	Amplitude Variation with Angle
AVO	Amplitude Variation with Offset
B	Gradient (AVO attribute)
C	Curvature (AVO attribute)
CCP	Common Conversion Point
CMP	Common Mid- Point
DMO	Dip Move-Out
EI	Elastic Impedance
F/X	Frequency-space (in 2D)
FF	Fluid Factor
FK, $f\text{-}k$	Frequency-wavenumber
FXY	Frequency-space (in 3D)
GLI3D	Generalized Linear Inverse 3D (refraction statics program by Hampson-Russell)
IGeoS	Integrated GeoScience (software package)
H-R	Hampson-Russell
LMR	Lambda, Mu, -Rho (λ, μ, ρ) –Lamé parameters
LR	$\lambda\rho$ attribute
MR	$\mu\rho$ attribute
NMO	Normal Move-Out
QC	Quality Control
R	Reflectivity
RMS	Root-Mean-Square
σ	Poisson's ratio
SILC	Seismic Inversion of by well-Log Calibration
V_P	P-wave velocity

V_S	S-wave velocity
VSP	Vertical Seismic Profiling
Z_P	P-wave (acoustic) impedance, also denoted AI
Z_S	S-wave impedance
P	Density

CONTENTS

LIST OF TABLES

LIST OF FIGURES

1 Introduction

1.1 Use of impedance and AVO attributes in interpretation

Since the 1970's, Acoustic Impedance (AI) has become a primary quantity used in seismic reflectivity inversion and interpretation (Lindseth, 1979). The key attractive property making AI so useful is its direct correlation with rock properties measured in the laboratory and in the field, since it is the product of density and acoustic velocity. By contrast to seismic reflectivity, which occurs at the contacts of contrasting strata, AI takes on constant values within rock layers, allowing a straightforward and intuitive correlation with geology and stratigraphy.

The impedance is extracted from seismic reflection data by a process usually called inversion. Seismic inversion tries to transform the spiked seismic reflectivity at geological boundaries (caused by changes in the lithology or physical state) into meaningful mechanical layer properties (impedances). In the acoustic (*P*-wave) case, the inversion algorithm transforms the reflection amplitudes into AI, which is the product of density and P-wave velocity, $AI = \rho V_P$. In well-log measurements, both of these properties can be measured, and therefore impedance logs can be obtained and directly compared to the seismic AI. Through the process of seismic inversion, we can transform seismic sections to AI sections, which represent the lithological properties of the layers rather than interface properties. Therefore, transformation to AI simplifies the lithological and stratigraphic interpretation and plays an important role in seismic interpretation and reservoir characterization, such as identification of fluid-filled and porous zones.

The AI is typically inverted from stacked seismic data, which approximate the normal-incidence reflectivity. However, pre-stack Amplitude Variations with incidence Angle (AVA) also contain a wealth of information about the mechanical properties of the reflector. Ostrander (1982) sparked the initial interest in pre-stack seismic attributes when he pointed out that gas-sand reflection coefficients change in an anomalous manner with increasing offsets and showed how to utilize this behaviour as a direct hydrocarbon indicator. The AVA method is generally, the Amplitude Variation with Offset (AVO) method, and was further developed (Ostrander, 1982) to assist in identifying the fluid content of the

reservoir. The AVO method started with production of models and comparison of these models to the common-offset stacks gathered from real seismic data (Russell and Hampson, 1991). The Aki and Richards' (2002) equation for seismic reflectivity was combined by Smith and Gidlow (1987) with mudrock line (Castagna et al., 1985) to emphasize the anomalies in seismic data that could be useful indicators of hydrocarbon reservoirs.

Today, AVO analysis and inversion of seismic data are routinely used to derive seismic attributes which are used as hydrocarbon indicators. Such attributes usually are: the acoustic impedance ($Z_P = AI = \rho V_P$), shear impedance ($Z_S = \rho V_S$), elastic impedance (*EI*), Lamé parameters (*LMR*) and the ratio of compressional- and shear-wave velocities (V_P/V_S) (Singh, 2007). The elastic impedance is defined as an extension of the convolutional model to non-zero incident angles (Connolly, 1999). The LMR attributes attempt capturing the intrinsic mechanical properties of the rock, such as the products of their elastic modules (λ and μ) with density (ρ). From these attributes, we can derive the *P*- and *S*-wave velocities and densities which can be further used to describe the properties of rock matrix and pore fluid. Thus, from true-amplitude processing of seismic traces, we can extract the reflectivities and impedances, and by adding the measured velocities, the density can be further estimated.

In the AVO analysis, pre- and post-stack techniques should be carefully differentiated (Russell, 1988). Post-stack seismic inversion methods use stacked (zero-offset) seismic data to produce images of the AI in depth or time. Pre-stack (AVO) inversion uses the variations of reflection amplitudes within the individual Common Midpoint Gathers (CMP) in order to determine the complete set of elastic properties (V_P, V_S, ρ), or equivalently, elastic constant properties (λ, μ, ρ) of the subsurface. From these properties, the petrophysical properties and fluid/gas saturation may be further inferred. In addition, CMP gathers can be used to directly invert for the P- and S-wave impedances and to extract other attributes such as V_P/V_S ratios. Both of these methods depend on the theoretical relationships between the physical properties and the seismic amplitudes. In summary, variations of the amplitudes of post and pre-stack seismic data are valuable for hydrocarbon investigation, especially in relation to gas reservoirs.

1.2 Objectives and structure of this thesis

This project focuses on comparing several techniques used to identify and characterize a thin reservoir in Blackfoot area by using 3D seismic dataset and geophysical logs from eleven wells in the area. A new impedance inversion technique recently proposed by Morozov and Ma (in press) called Seismic Inversion by well-Log Calibration (SILC) is also applied to the seismic data and compared to the conventional techniques. The specific objectives of this study are:

1. Process the seismic data and prepare them to inversion and AVO analysis. This results in:
   a. Stacked data;
   b. Range-limited stacked data;
   c. CMP gathers for pre-stack inversion.
2. Identify and pick horizons.
3. Use correlation to tie between seismic and wells in the area.
4. By using post-stack data, apply inversion methods to extract the AI by using:
   a. Model-based inversion;
   b. Band-limited inversion (also called iterative or recursive);
   c. Coloured inversion;
   d. Seismic Inversion by well-Log Calibration (SILC).
5. From range-limited stacked data:
   a. Perform elastic impedance for near and far angle stack.
6. From CMP gathers:
   a. Apply simultaneous inversion to extract the P-impedance, S-impedance, V_P/V_S ratio and LMR parameters;
   b. Create volumes of attributes such as the AVO intercept (A), gradient (B) and Fluid Factor (FF).
7. Visualize and interpret the images, correlate with the available well logs and known gas reservoirs within the area.

Based on this comparative analysis, I make conclusions and recommendations regarding the effectiveness of the different attributes for identifying the gas reservoir and for measuring its parameters.

This thesis is organized as follows. In Chapter 1, I give an introduction to the use of impedance and AVO attributes in interpretation, as well as detailed objectives of the study, an overview the Blackfoot 3C-3D dataset, and a description describe the geological background and a brief outline of the seismic data processing. Chapter 2 discusses the methods and theories used in this research, such as the AVO attributes, post-stack inversion, elastic impedance, pre-stack inversion and elastic parameters (λ, μ and ρ). Chapter 3 gives a further discussion of the implementation of the methods and their parameters for the Blackfoot 3D dataset. Four post-stack AI methods and one pre-stack EI inversion methods are applied to our seismic data in this Chapter. EI, AVO, and LMR attributes are also discussed in Chapter 3. In Chapter 4, I present the results and discussions, as well as make conclusions from this study and offer some suggestions for future research.

1.3   Blackfoot 3C-3D dataset overview

The Blackfoot field is located south-east of Strathmore, Alberta, Canada in Township 23, Range 23W4 (Figure1.3.1). Extensive seismic work has been done in this field by Pan Canadian Petroleum and the CREWES (the Consortium for Research in Elastic-Wave Exploration Seismology) project at the University of Calgary. The 3C-3D seismic dataset was recorded in October 1996. The goal of this experiment was to demonstrate that 3C-3D seismic data (*P-P, P-S*) can be used to enhance the conventional 3D P-wave structural and stratigraphic images, to discriminate the lithology, and to study anisotropy (Lawton, 1996). This survey was recorded in two overlapping patches: the first patch targeted the clastic Glauconitic channel, and the second one went deeper to consider the reef-prone Beaverhill lake carbonate. In the present study, we only consider the first patch, which focused on the Glauconitic channel.
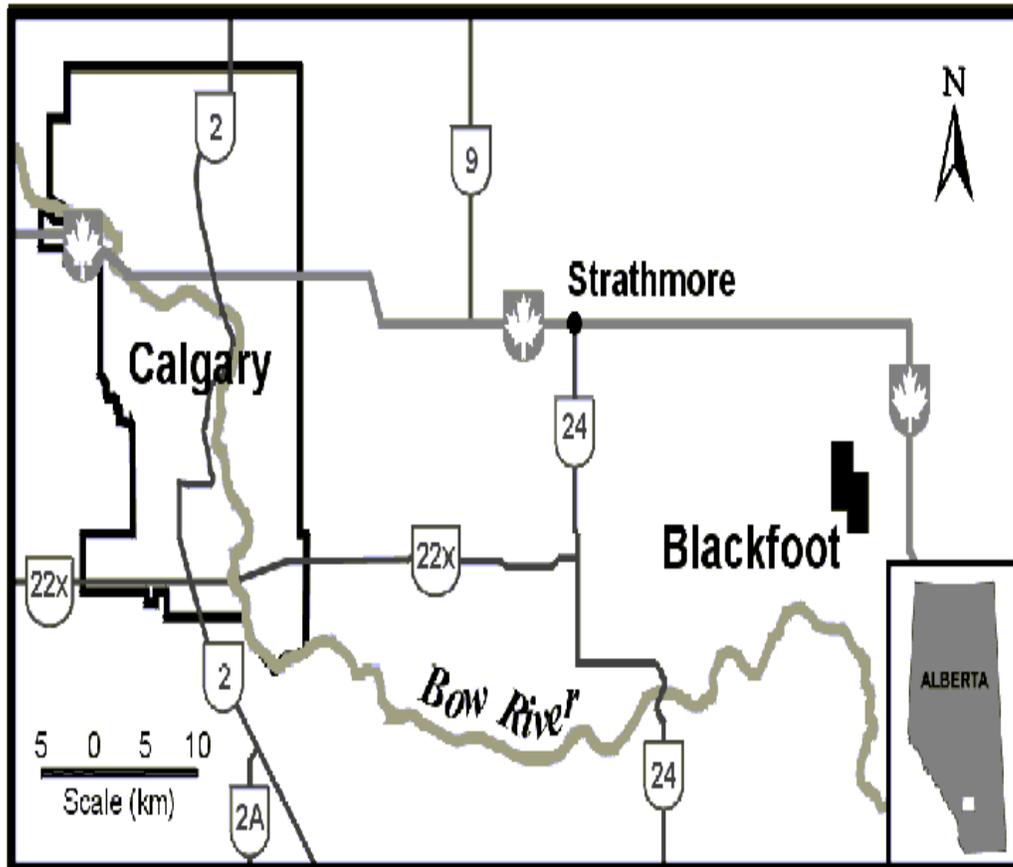
Figure 1.3.1. Location of Blackfoot area

The Blackfoot dataset was processed by Pulsonic Geophysical and Sensor Geophysical. Filtering and deconvolution was the initial test done on the data; and the bandwidth of the data was found to be 5-90 Hz for the vertical-component data and 5-50 Hz for horizontal data. The following two processing flows show the processing steps for the vertical and horizontal data (Simin et al, 1996).

Table 1.3.1. Pulsonic's vertical processing flow

SEG-D reformatted demultiplex input
Component separation
3D geometry assignment
Trace edits
Surface-consistent amplitude balance
Surface consistent deconvolution
Horizontal component rotation
Elevation and refraction statics
Residual surface-consistent statics
Asymptotic CCP macro-bin sort
Velocity analysis
3D NMO correction
Velocity specific filter
FK median filter
Trace mute
3D converted wave DMO
3D CCP bin stack
F/X migration
Spectral balance
FXY deconvolution
Band-pass filter
Time-variant scaling

Table 1.3.2. Pulsonic's radial flow processing

SEG-D reformatted demultiplex input
Component separation
3D geometry assignment
Trace edits
Surface-consistent amplitude balance
Surface consistent deconvolution
Horizontal component rotation
Elevation and refraction statics
Residual surface-consistent statics
Asymptotic CCP macro-bin sort
Velocity analysis
3D NMO correction
Velocity-specific filter
FK median filter
Trace mute
3D converted wave DMO
3D CCP bin stack
F/X migration
Spectral balance
FXY deconvolution
Band-pass filter
Time-variant scaling

A 3C-3D VSP (vertical seismic profiling) dataset was recorded simultaneously from the same shots used for the 3C-3D surface survey (Figure1.3 2) (Zhang and Stewart, 1996). The 3C-3D VSP data were recorded from 431 source locations, and these data were processed by Western Atlas. These data provided further seismic information data in the time-depth domain that could be used in combination with surface seismic data to identify and correlate reflectors. These data were also used to produce 2-D seismic images near the borehole (Gulati et al., 1997).
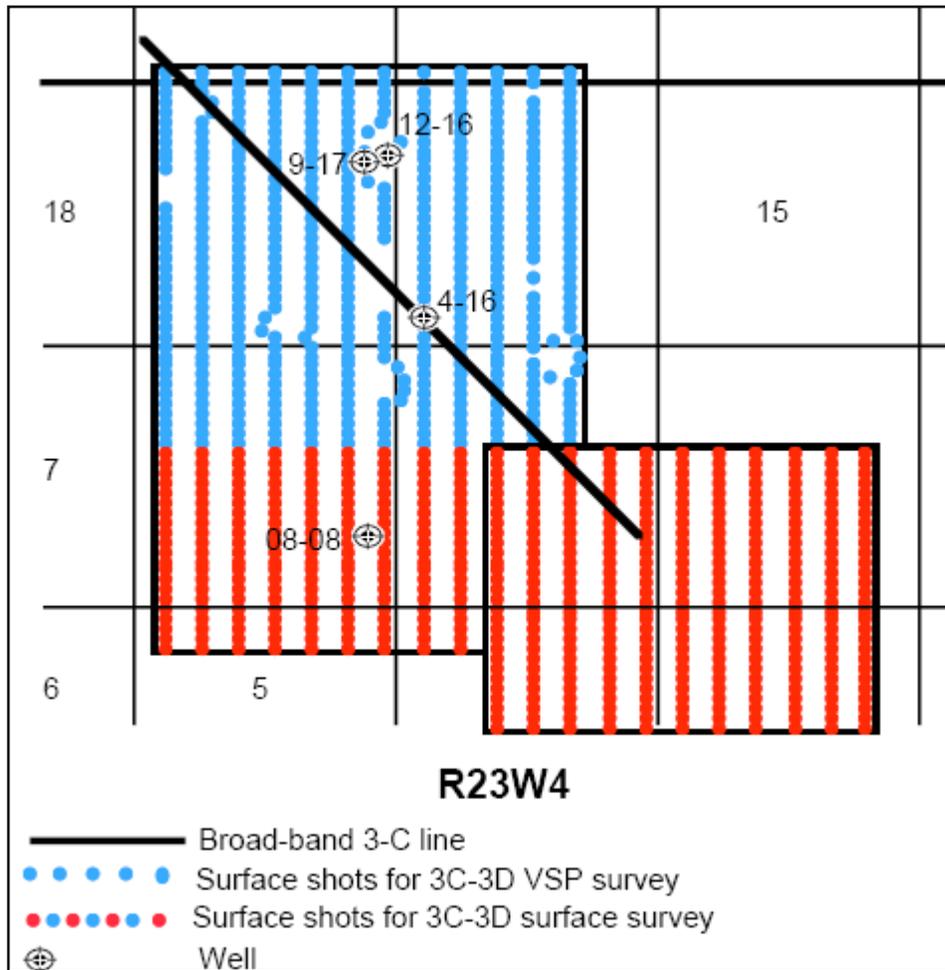
Figure 1.3.2. Map of Blackfoot surveys showing shot points of the full 3C-3D survey, selected wells and a previous broad-band 2D line (Zhang, 1996).

The Blackfoot area also contains a number of wells. Sonic and density logs were recorded in several of these wells (04-16-023-23W4, 08-08-023-023-W4 and 09-17-023-23W4). Well 08-08-023-023-W4 is a multi zone-gas producer from the top channel and oil

from the base. Well-log data were used to correlate the seismic data and to guide the AVO analysis and inversion.

From 1995, extensive research work was done on the Blackfoot field, primarily by members of the CREWES project. Using the Blackfoot data, CREWES has produced several reports in different research areas, such as AVO analysis, simultaneous *P-P* and *P-S* inversion, processing, 3C-3D VSP and converted-wave seismic exploration (Xu and Bancroft, 1997; Larsen et al., 1998; Simin et al, 1996; Gulti et al., 1997; and Stewart et al., 1999).

In this study, I only utilize the conventional (vertical-component) 3D seismic data and eleven well-log datasets. Figure 1.3.3 shows the base map of the shots, receivers and CMP of the Blackfoot area used in this study. The dataset contains 708 shots into a fixed recording spread of 690 channels. The fold is 140 at the centre of the spread, as shown in Figure 1.3.4. Acquisition parameters used in this patch are described in Table 1.3.3.

Table 1.3.3. Blackfoot 3D acquisition parameters (Glauconitic patch)

Source Parameters	
Line orientation	North-South
Source interval	60m
Source line interval	210m
Number of source lines	12
Total number of source points	708
Source depth	18m
Receiver parameters	
Line orientation	East-West
Receiver interval	60m
Receiver line interval	255m
Number of receiver lines	15
Total number of receiver points	690
Receiver depth	0.5m
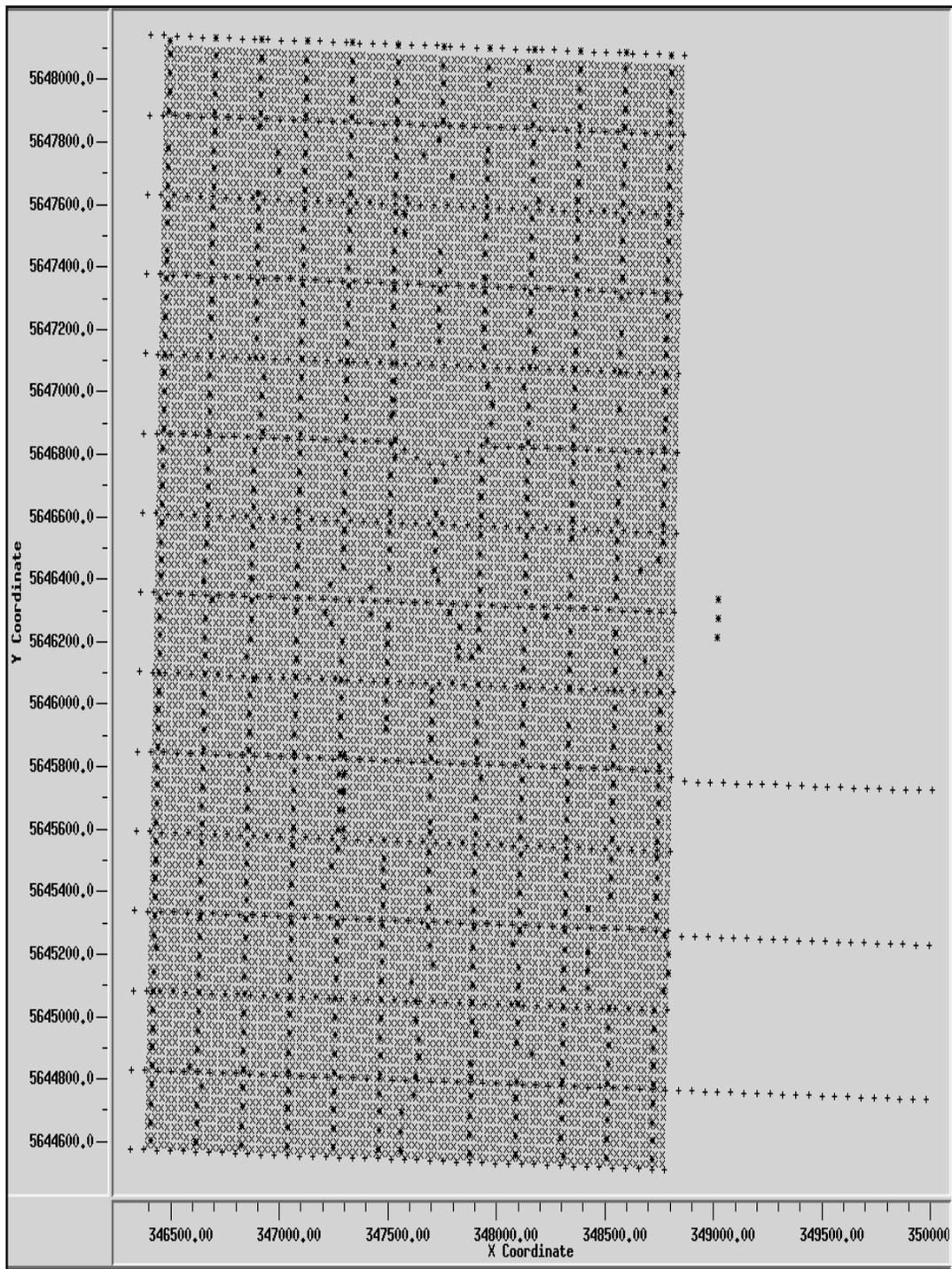
Figure 1.3.3. Base map of shots (*), receivers (+) and CMPs (×) used in the Blackfoot area.
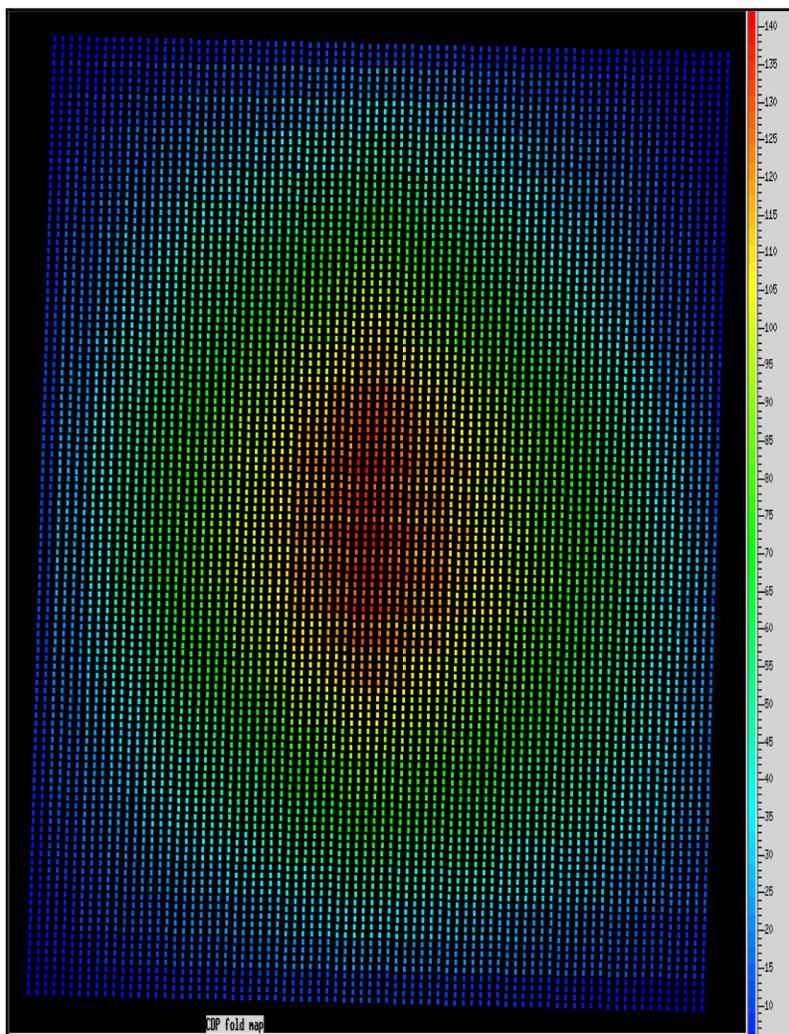
Figure 1.3.4. CDP fold map. The fold number is the largest (142) at the centre and decreases to the edges of the survey.

1.4 Geological background

The following is a brief review of the geology in Blackfoot area. Our target is the Glauconite Formation of the Lower Cretaceous which represents: sediment filled incised valley. Glauconite Formation of the Lower Cretaceous represent the upper Manville Group The thickness of the Glauconite sand varies up to 35meter at encounter depth 1550m where

is the reservoir depth. The grain size of the Glauconite Formation varies from fine to medium.

In this field, eroded Mississippian carbonates are covered with Lower Cretaceous sediments. These sediments are the Detrital member of variable thickness, while above this Detrital member there are sheet and ribbon Sunburst sands. At a later time (Cretaceous), marine transgression deposited brackish shales, limestones and quartz sands and silts to build the Ostracod member. The Glauconitic member consists of shales and sands of lacustrian and channel origin. Within the channel, the sediments are subdivided into three units corresponding to three phases of valley incision with different quality of sand deposited. These three units may are not be encountered everywhere in the area. The reservoir in the Blackfoot field is producing from the Glauconitic sand of the Lower Cretaceous Glauconitic Formation, in which the porosities are up to 18% . Figure 1.4.1 (Margrave et al., 1998) shows the stratigraphic column of the Blackfoot area. This field mainly produces oil and gas in some wells. In more detail, the geology of the Blackfoot Field was well discussed by Miller et al. (1995).
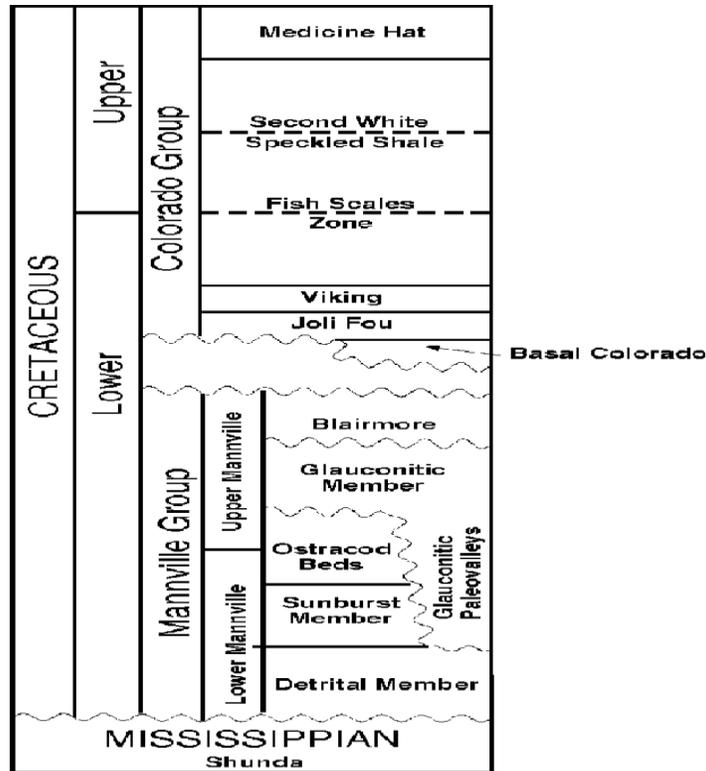
Figure 1.4.1. Stratigraphic column of Cretaceous rocks in the Blackfoot area (Margrave et al., 1997).

1.5 Seismic data processing

ProMAX software was used for processing the Blackfoot 3D seismic data. The initial data loading and geometry set up was performed by Dr. Ma prior to the beginning of this study. After this, trace editing was applied to remove bad traces and to correct traces with reverse polarities. In addition, true amplitude recovery was performed to compensate for the loss of amplitudes caused by wave divergence away from the sources. The remaining seismic processing steps were: inversion for statics correction, noise filtering, velocity analysis and stacking, as shown in Table 1.5.1.

14

Table 1.5.1. Seismic data processing steps

#	Operation	Purpose
1	3D GEOMETRY ASSIGNMENT (performed by Dr. Jinfeng Ma)	Providing the geographic reference.
2	TRACE EDITS	Removing bad traces, reversing polarity as necessary, and muting.
3	TRUE AMPLITUDE RECOVERY	To recover the loss of amplitude as the wave divergence
4	ELEVATION AND REFRACTION STATICS	Time correction for shallow subsurface
5	BAND-PASS FILTER	Attenuating the ground roll in shot gathers
6	VELOCITY ANALYSIS	Extract RMS velocity for NMO correction
7	3D NMO CORRECTION	Removal of reflection time moveout.
8	3D CMP stack	Increasing signal to noise ratio.
9	AGC (Automatic gain control) and DISPLAY	Increase the amplitude for display
10	F-X deconvolution	Reducing random noise and improving image coherency

First, elevation and refraction static corrections were applied by using the GLI3D program by Hampson-Russell. First-arrival picking was performed for each of the 15 lines in 708 shots, and the first-arrival travel times were transferred to GLI3D. The program built a model of the weathering layer (Figure 1.5.1) and predicted the static corrections for all sources and receivers. These statics were applied to the seismic data in ProMAX software.

In the second step, band-pass filtering was used to remove the ground roll. I found frequency filtering was sufficiently effective for ground-roll removal in this dataset and no velocity-selective (e.g., *f-k*) filtering was required. Examples of the filtered sections are shown in Figures 1.5.2.

Next, stacking velocity analysis was performed on the CMP gathers by using a 180 m by 300 m grid (Figure 1.5.3). These stacking velocities were used to determine the normal moveout (NMO) corrections. Figure 1.5.4 illustrates selected CMPs gathers before and after application of the NMO corrections.

Finally, 3D stacked sections were obtained by stacking the traces within each CMP gather. These stacked sections were sorted into in-line and cross-line sections (Figure 1.5.5). F-X deconvolution was applied to the stacked seismic data to reduce random noise and improve image coherency. Figures 1.5.6 show selected in-line and cross-line stacked sections in the study area. In addition, an amplitude map was taken at a 1065-ms time slice, where the reservoir channel was expected (Figure 1.5.7).

As a guide to interpretation, several stratigraphic horizons were picked in the resulting 3D stacked volume. These horizons were later used to tie the reflectivity volume to the well logs, and also to control the inversion. Two of the most important time-structure maps of Manville above the reservoir and Mississippian carbonate beneath the reservoir are shown in Figures 1.5.8. Note that there is an increase in reflection times (cool colours) within the area of the channel.

16
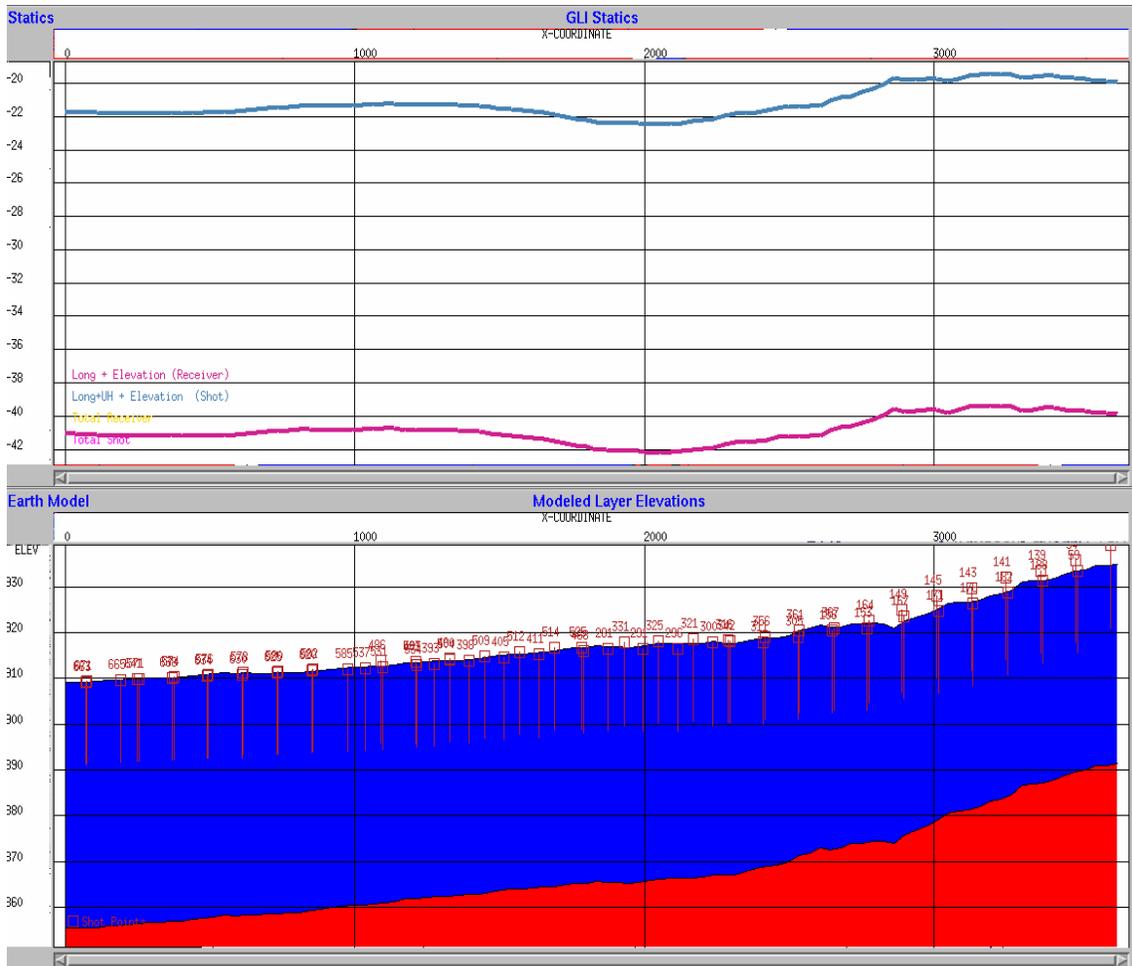
Figure 1.5.1. GLI3D static inversion results for cross-line 145. Blue colour shows the weathering layer. In upper plot, pink line shows the receiver statics, and light blue – shot statics derived from this model.
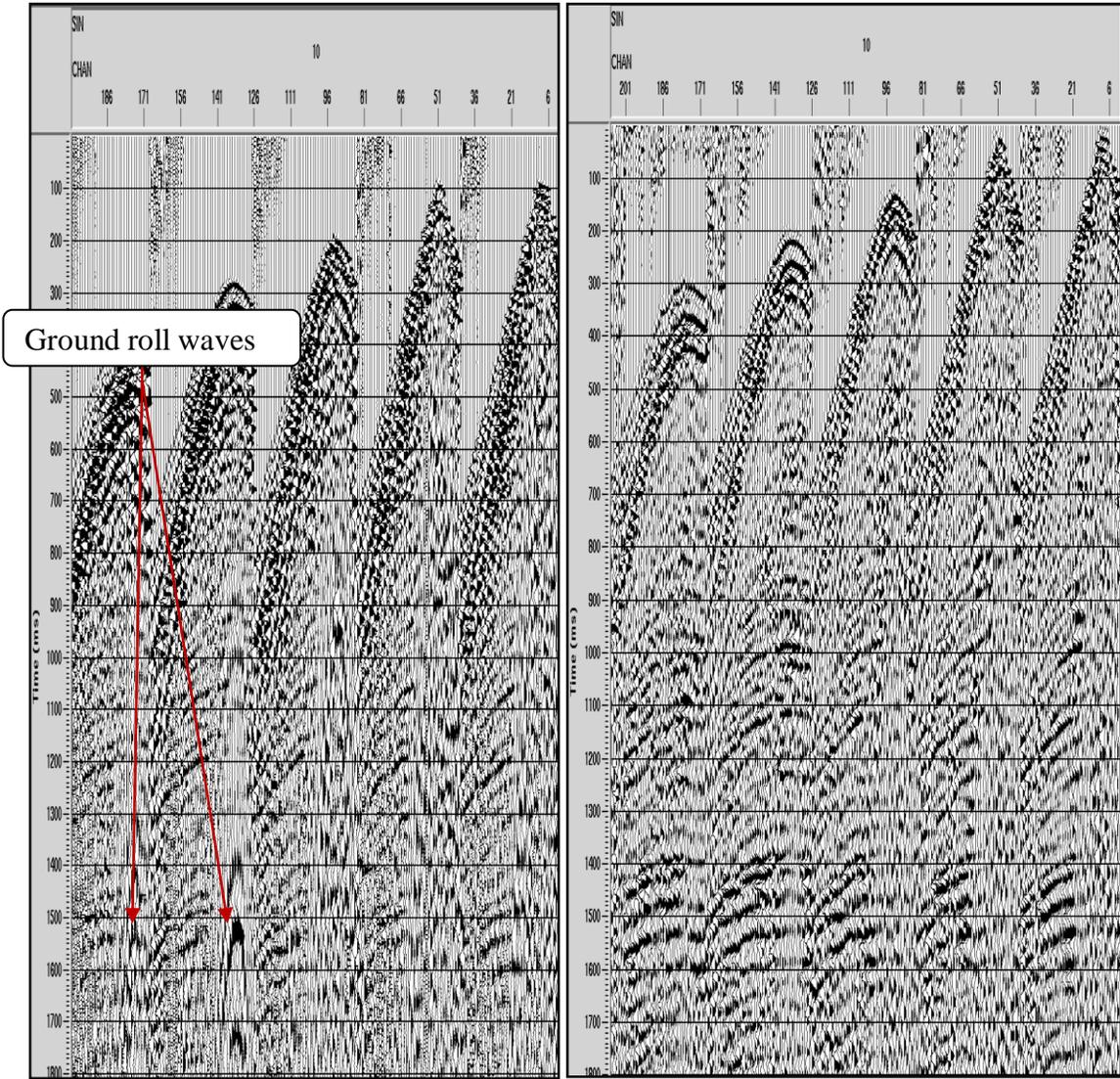
Figure 1.5.2. Selected shot records before and after applying the band-bass filter. Note the low-frequency ground-roll waves are attenuated by this filtering.
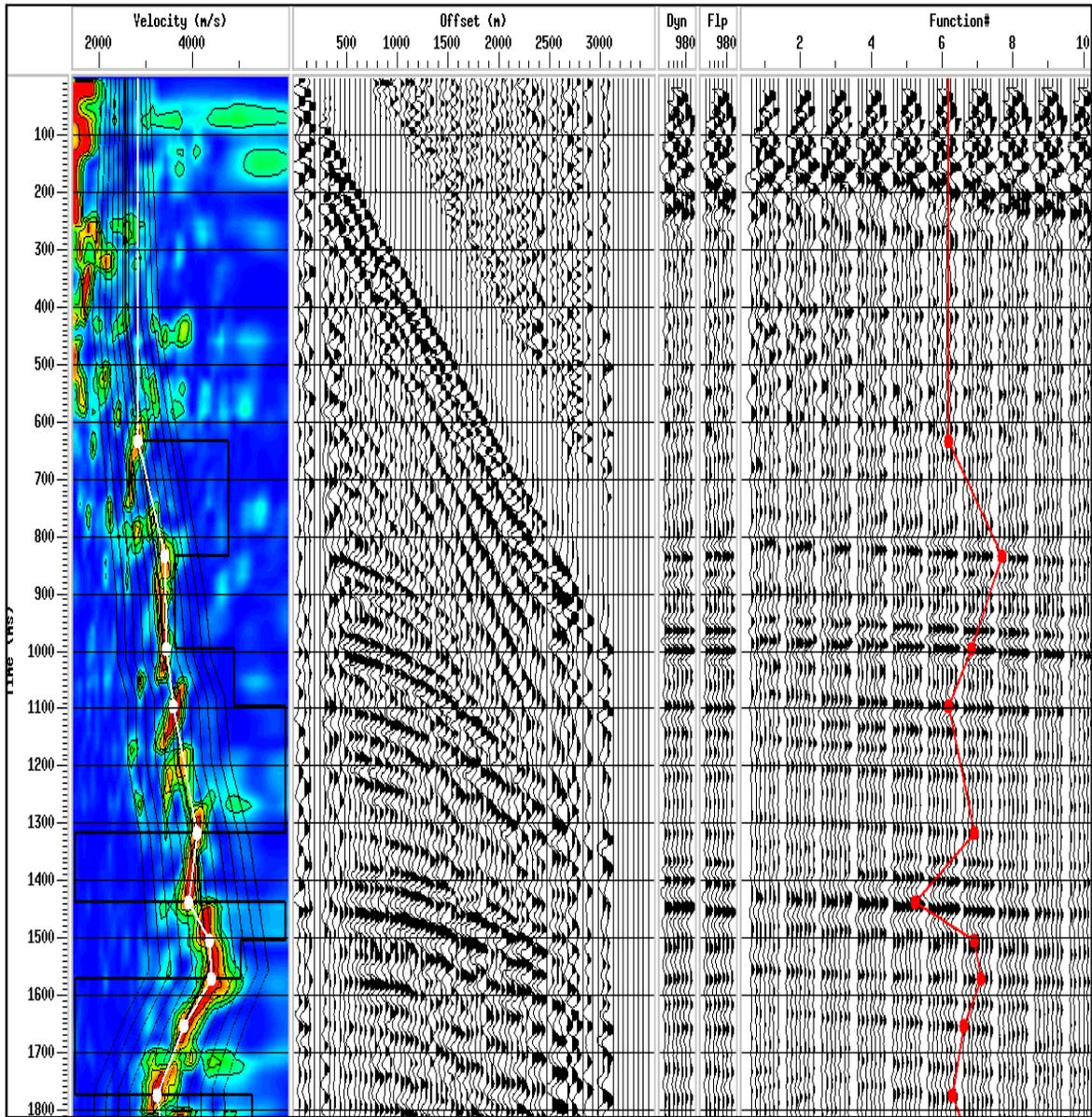
Figure 1.5.3. Velocity analyses in a CMP gather. Left: velocity spectrum; middle: CMP gather with offset; right: velocity analysis functions.
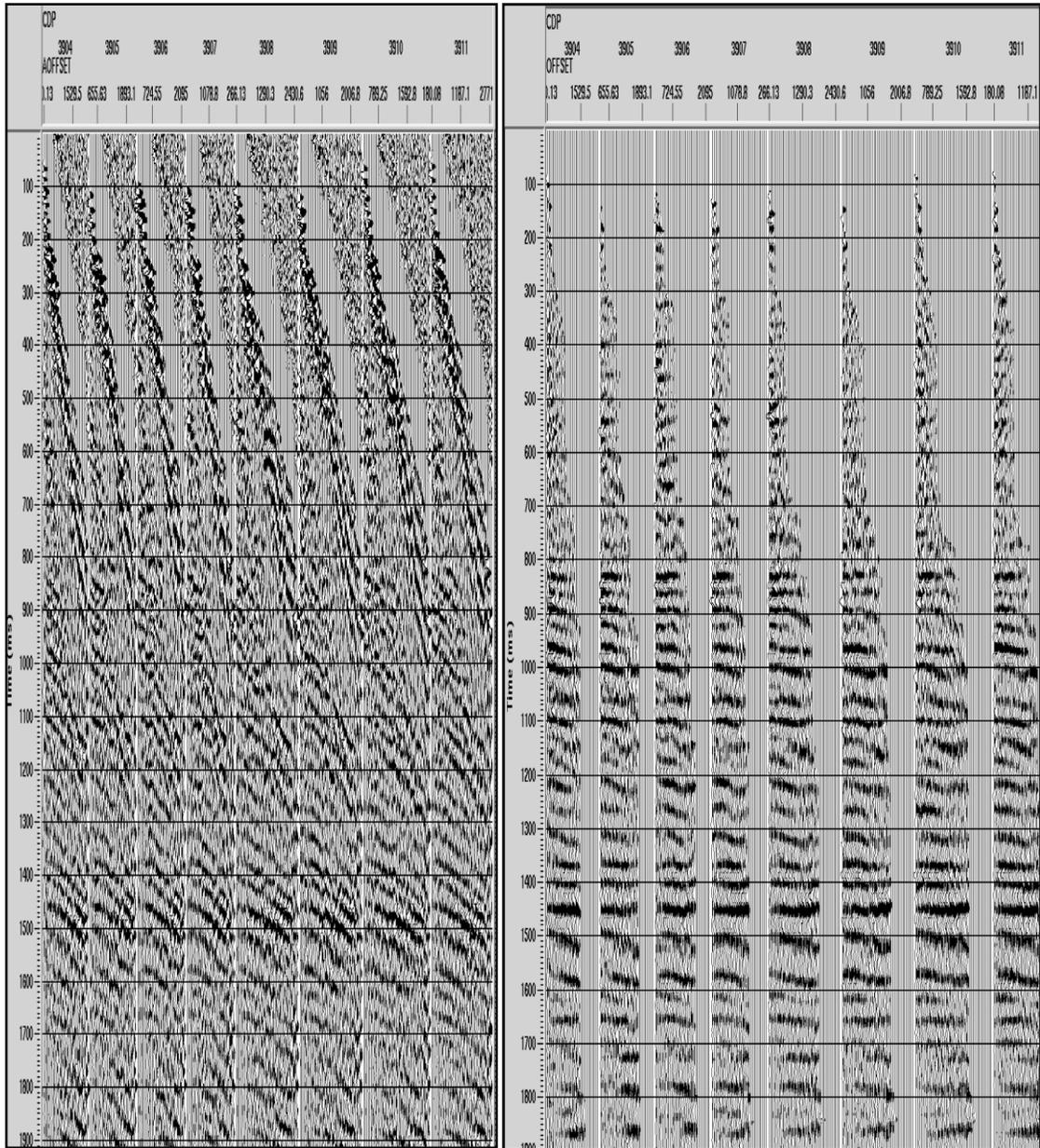
Figure 1.5.4. CMP gathers before (left) and after the NMO correction (right).
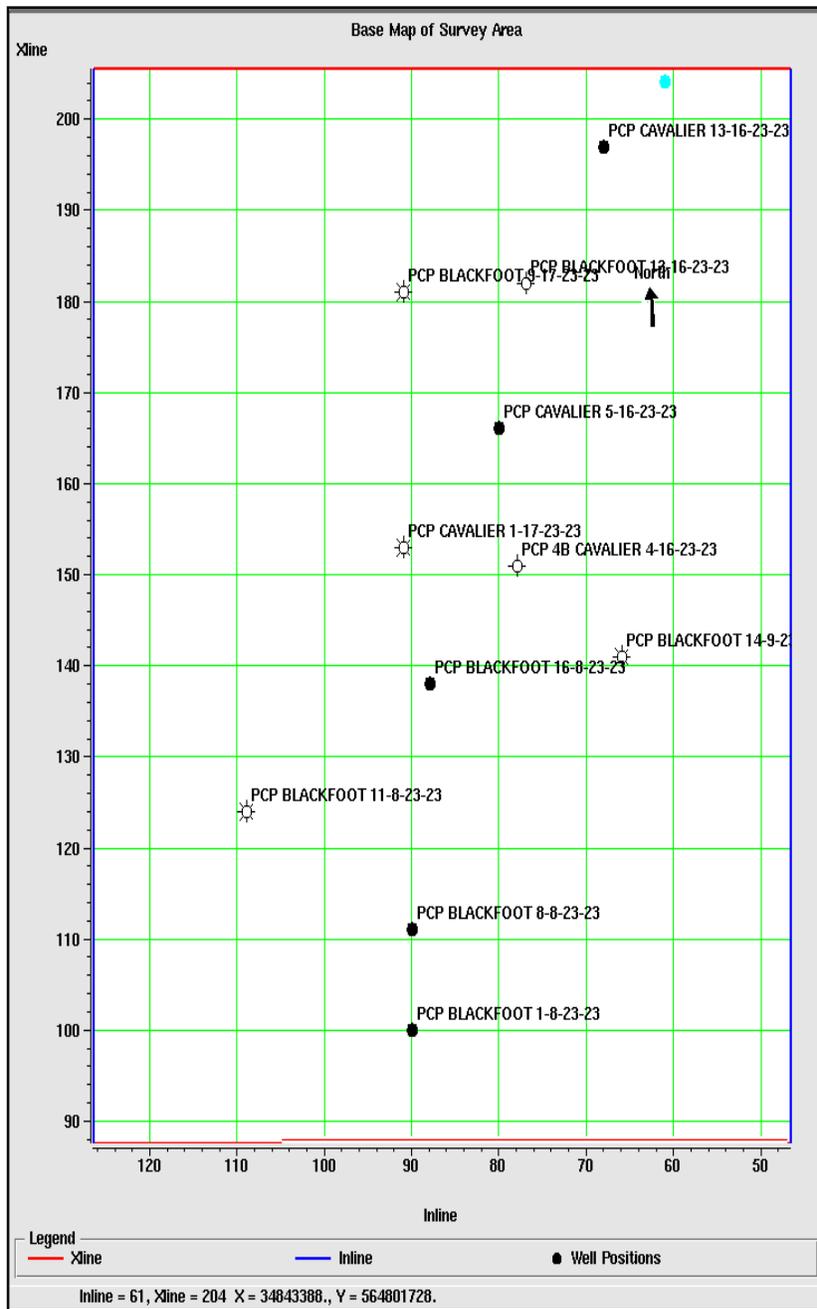
Figure 1.5.5. Base map of the area sorted into in-line and cross-line sections. The in-line numbers range from 47 to 126, and cross-line numbers range from 88 to 205.
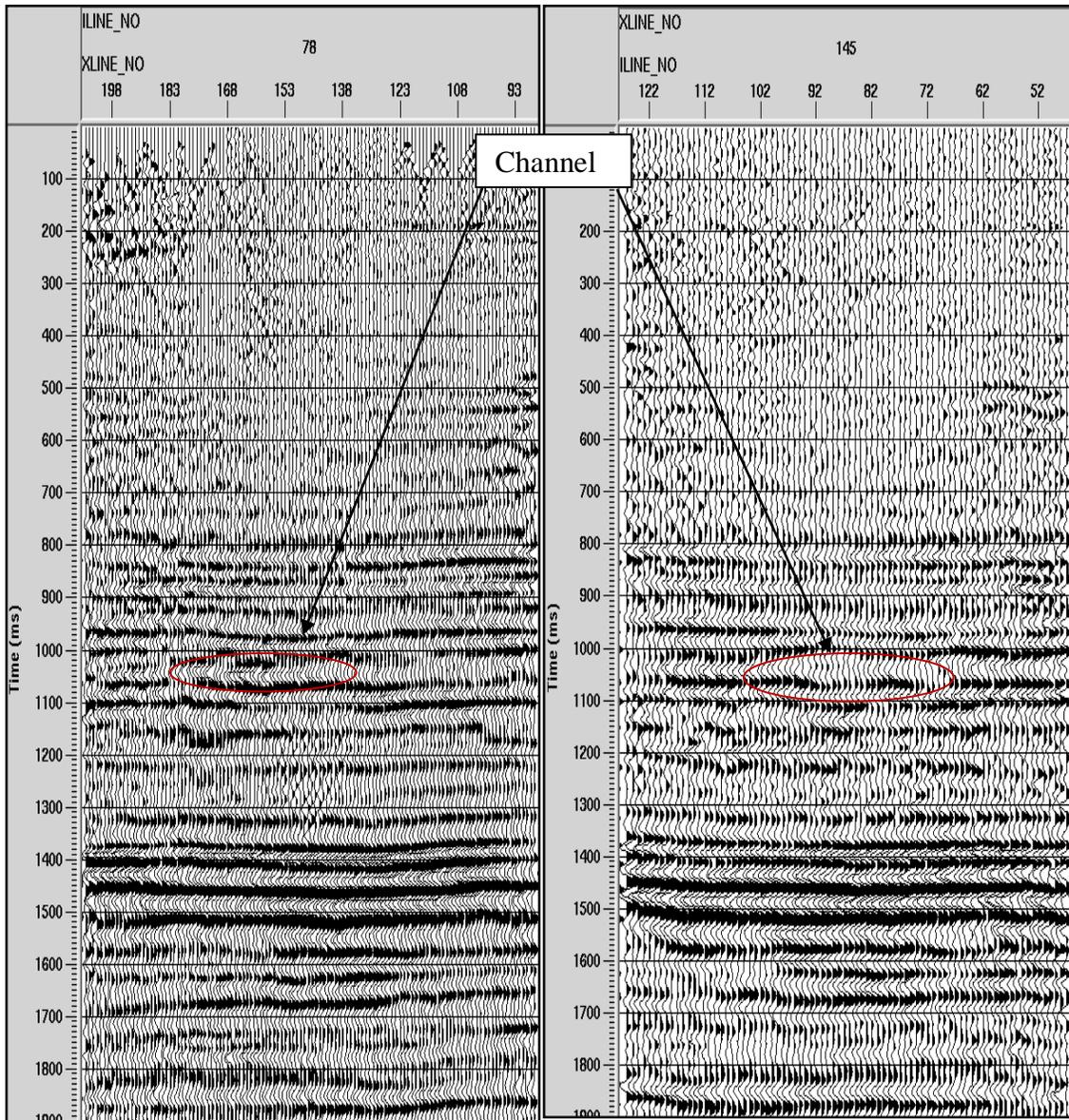
Figure 1.5.6. In-line and cross-line sections crossing the channel where the reservoir is expected. The position of the Glauconitic channel is indicated.

22
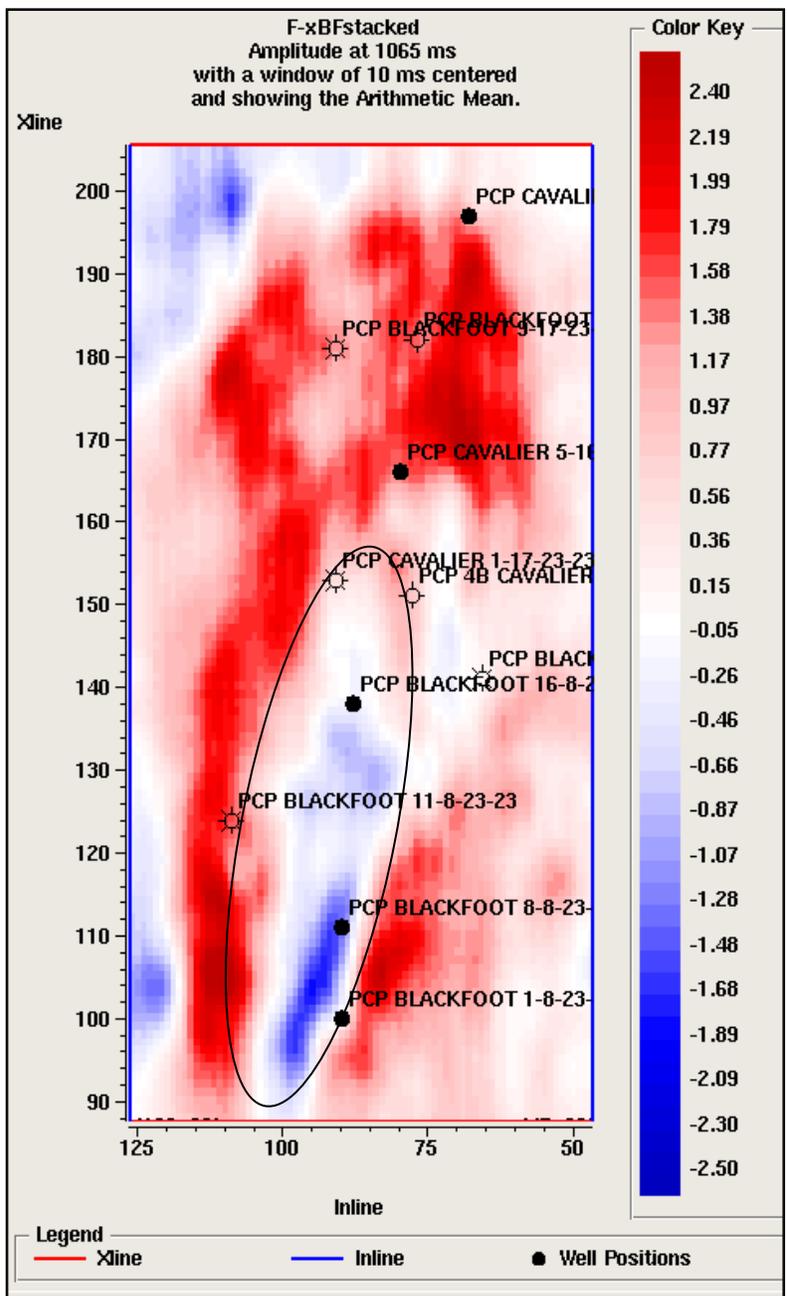
Figure 1.5.7. RMS Amplitude map at time slice of 1065 ms. Note the change from high positive amplitude to high negative amplitude in the Glauconitic channel.
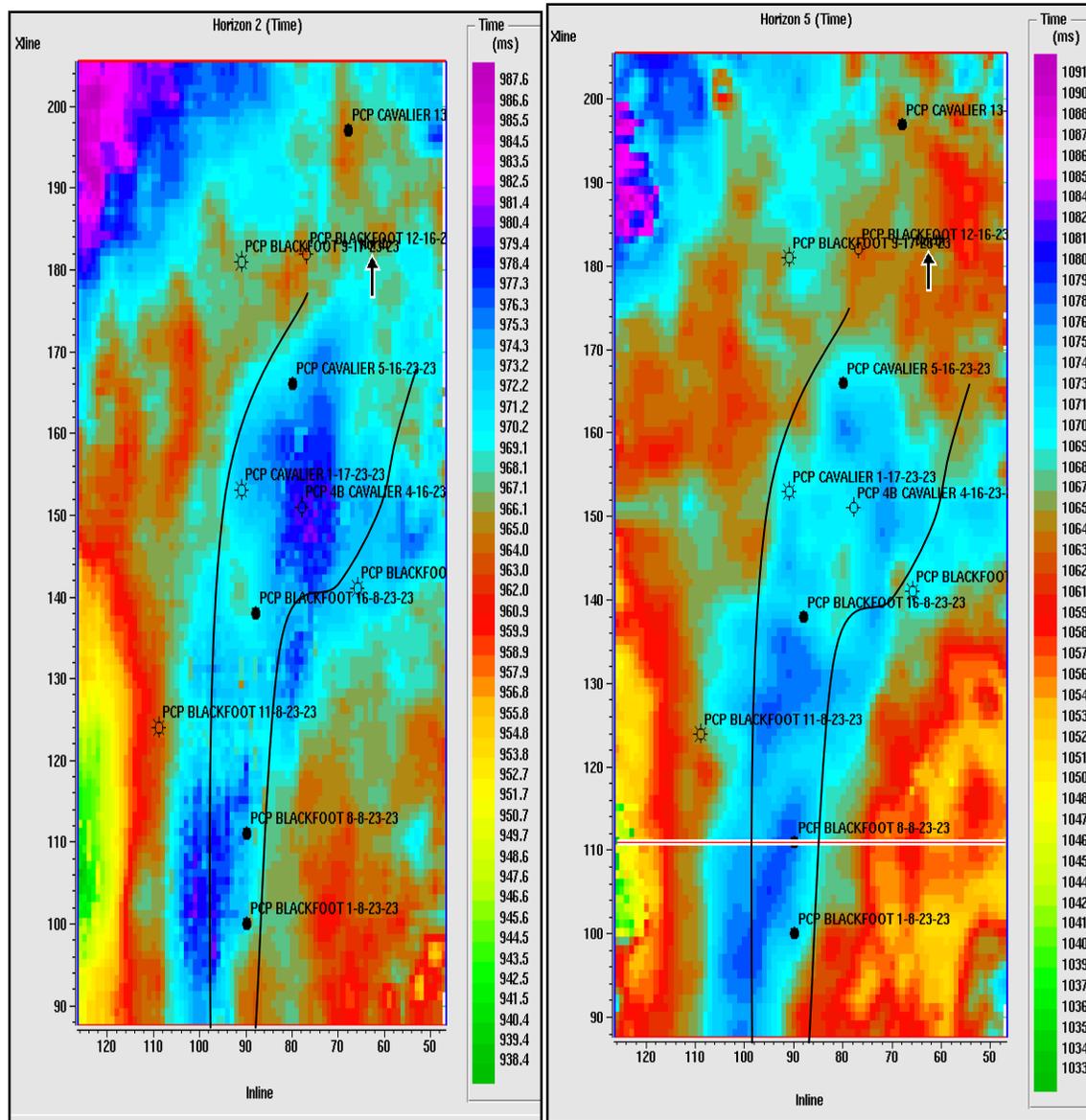
Figure 1.5.8. Time structure map of two horizons. Left: the top Manville above the reservoir; right: the Mississippian carbonate beneath the reservoir. Scheme is the location of the channel based on the wells according to Crews report. Locations of the wells is also shown.

24

2   Methods

2.1   Pre-stack AVO attributes

The relationship between the incident and reflection/transmission amplitudes for plane waves at an elastic interface is described by the Zoeppritz equations. These equations (eq2.1.1) give us the exact amplitudes as functions of the incidence angle. Figure 2.1.1 explains the notation used in equation (2.1.1).

$$
\begin{bmatrix} R_P(\theta_1) \\ R_S(\theta_1) \\ T_P(\theta_1) \\ T_S(\theta_1) \end{bmatrix} =
$$

$$
\begin{bmatrix}
-sin\theta_1 & -cos\phi_2 & sin\theta_2 & cos\phi_2 \\
cos\theta_1 & -sin\phi_1 & cos\theta_2 & -sin\phi_2 \\
sin2\theta_1 & \frac{V_{P1}}{V_{S1}}cos2\phi_1 & \frac{\rho_2 V^2{}_{S2}V_{P2}}{\rho_1 V^2{}_S V_{P2}}cos2\phi_1 & \frac{\rho_2 V_{S2}V_{P1}}{\rho_2 V^2{}_{S1}}cos2\phi_2 \\
-cos2\phi_1 & \frac{V_{S1}}{V_{P1}}sin2\phi_1 & \frac{\rho_2 V_{P2}}{\rho_1 V_{P1}}cos2\phi_2 & -\frac{\rho_2 V_{S2}}{\rho_1 V_{P1}}sin2\phi_2
\end{bmatrix}
\begin{bmatrix} sin\theta_1 \\ cos\theta_1 \\ sin2\theta_1 \\ cos2\phi_1 \end{bmatrix}. \quad (2.1.1)
$$
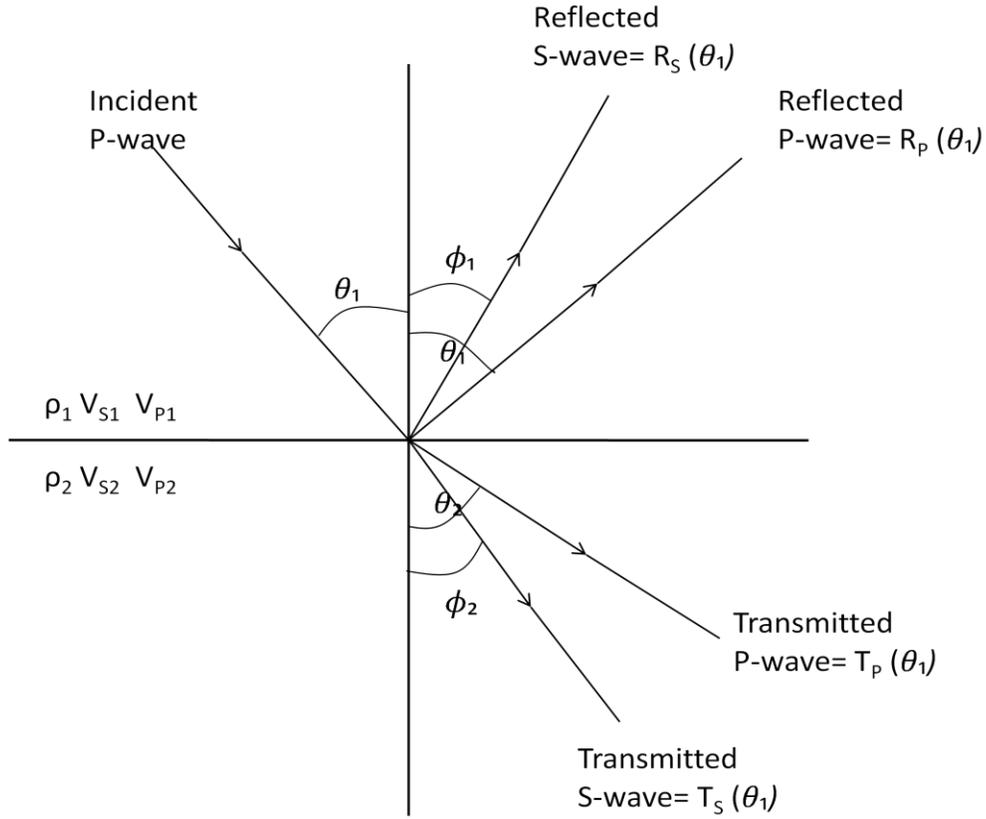
Figure 2.1.1. Notation used in eq (2. 1.1).

The AVA/AVO analysis typically uses the small-contrast approximations to Zoeppritz equations, given by Aki and Richards (2002). The first equation above was further linearized in respect to small variations of elastic parameters across the boundary, yielding an approximation of the full Zoeppritz equations (Aki and Richards, 2002):

$$R(\theta) = a\frac{\Delta V_P}{V_P} + b\frac{\Delta V_S}{V_S} + c\frac{\Delta \rho}{\rho}, \tag{2.1.2}$$

where: $\qquad a = \frac{1}{2cos^2\theta},$ $\qquad\qquad\qquad\qquad\qquad$ (2.1.3)

$$b = 0.5 - \left(\frac{V_S}{V_P}\right)^2 sin^2\theta, \tag{2.1.4}$$

and $\qquad c = 4\left(\frac{V_S}{V_P}\right)^2 sin^2\theta.$ $\qquad\qquad\qquad\qquad\qquad$ (2.1.5)

Wiggins et al. (1983) separated the three terms related to perturbations in the elastic parameters of interest (Russell, 1988):

$$R(\theta) = A + Bsin^2\theta + Ctan^2\theta sin^2\theta, \tag{2.1.6}$$

26

where:

$$A = \frac{1}{2}\left[\frac{\Delta V_P}{V_P} + \frac{\Delta \rho}{\rho}\right], \hspace{4cm} (2.1.7)$$

$$B = \frac{1}{2}\frac{\Delta V_P}{V_P} - 4\left[\frac{V_S}{V_P}\right]^2\frac{\Delta V_S}{V_S} - 2\left[\frac{V_S}{V_P}\right]^2\frac{\Delta \rho}{\rho}, \hspace{1.5cm} (2.1.8)$$

$$C = \frac{1}{2}\frac{\Delta V_P}{V_S}. \hspace{4cm} (2.1.9)$$

These equations predict an approximately linear relationship between the amplitude and $\sin^2\theta$ (Aki and Richards, 2002). In equations 2.1.(6-9), the intercept (A) is the zero-offset reflection coefficient, which is a function of the P-wave velocity and density. The AVO gradient (B) depends on the P- and S-wave velocities and density. The gradient has the largest effect on the amplitude variation with offset. The curvature factor (C) has only a very small effect on the amplitudes at incidence angles below 30°. By using the two terms of the Aki and Richards equation, one can extract them at different reflection times from the seismic amplitudes in CMP gathers. As a result, the intercept and gradient seismic attributes, $A(t)$ and $B(t)$ are produced (Figure 2.1. 2).
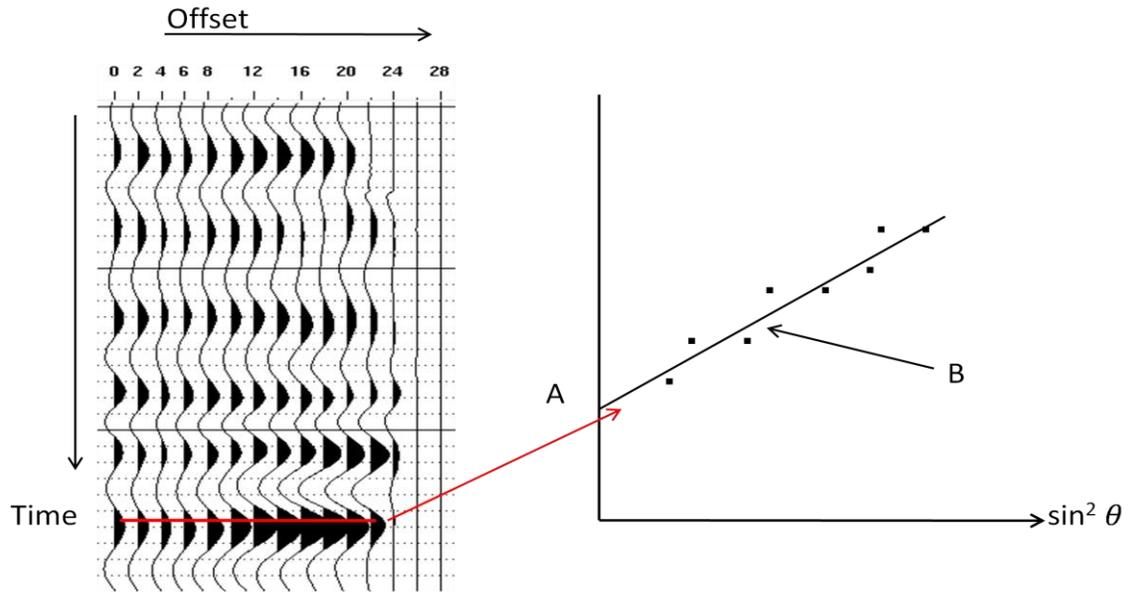
Figure 2.1.2. Amplitudes extracted from CMP gather are positive and is increasing with offset for Class III gas sandstone. A and B are the intercept and slope of the amplitude dependence on $\sin^2\theta$, respectively.

Another useful simplification of Zoeppritz equation was proposed by Shuey (1985), who decomposed the reflectivity into the normal-incidence term and corrections principally depending on the Poisson's ratio and density variations across the boundary:

$$R(\theta) \approx R_0 + \left[A_0 R_0 + \frac{\Delta\sigma}{(1-\sigma)^2} \right] sin^2\theta + \frac{1}{2}\frac{\Delta V_P}{V_P}(tan^2\theta - sin^2\theta), \quad (2.1.10)$$

where $R_0 = \frac{1}{2}\left[\frac{\Delta V_P}{V_P} + \frac{\Delta\rho}{\rho} \right],$ (2.1.11)

$$A_0 = B - 2(1 + B)\frac{1-2\sigma}{1-\sigma}, \quad (2.1.12)$$

$$B = \frac{\Delta V_P/V_P}{\Delta V_P/V_P + \Delta\rho/\rho}. \quad (2.1.13)$$

The first term in eq 2.1.10 describes the amplitude at $\theta=0$, the second term represents an amplitude correction at intermediate angles, and the third term describes the amplitude at wide angles. For a rock sample under unidirectional pressure, the Poisson's ratio σ is the ratio of the transverse expansion to the longitudinal compression, or the ratio of shear strain to principal strain (Yilmaz, 2006). For isotropic rock, σ can be expressed through the ratio of the P- and S-wave velocities:.

$$\sigma = \frac{\left(\frac{V_P}{V_S}\right)^2 - 2}{2\left(\frac{V_P}{V_S}\right)^2 - 2} \quad (2.1.14)$$

Thus, the Poisson's ratio increases when V_P/V_S increases, and vice versa, and therefore this ratio is typically low for gas reservoirs (Ostandard, 1982). It typically equals to 0.1, for gas sands, for which while p- $V_P/V_S \approx 1.5$. Changes in gas or fluid saturation change the Poisson's ratio significantly because of the changes in rock bulk modulus and consequently in the P-wave velocity. At the same time, the shear modulus changes only slightly, and therefore fluid saturation has little effect on the S-wave velocity (Gassmann, 1951). Therefore, an increase in fluid saturation decreases the P-wave reflectivity and the Poisson's ratio.

In 3D seismic datasets, attributes *A* and *B* above can be used to produce attribute volumes. However, such volumes are rarely used singly because they still do not provide unambiguous indicators of reservoir properties. Different combinations of these parameters are used to produce secondary attributes, such as given below:

1. AVO product: $A \cdot B$. This is a good indicator of the classical bright spots, in which high amplitudes (A) and increased gradients (B) occur simultaneously (Castagna and Smith, 1994). For example, class III gas sandstones have low impedance, and therefore both A and B are negative at its top and positive at the bottom (Figure 2.1.2). Consequently, the product ($A \cdot B$) shows large positive values for both the top and bottom of such reservoir.

2. Scaled Poisson's Ratio Change: $A + B$. This attribute relies on the assumption that the background Poisson's Ratio is approximately 1/3, and therefore $A + B = (9/4) \Delta\sigma$ by using the Shuey's approximation (Shuey, 1985). Therefore, this attribute is proportional to the change in the Poisson's Ratio, and consequently reflects the changes in the V_P/V_S ratio. In case of gas sand, σ decreases at the top and increases at the bottom of the reservoir, as a result of strong variations in the P-wave velocities combined with only slightly changes in S-wave velocities.

3. Shear Reflectivity: $A - B$. If we approximate, as it is commonly done, that $V_P/V_S = 2$, (corresponding to the Poisson's ratio of 1/3), and use equations 2.1.7 and 2.1.8, then this attribute ($A - B$) is proportional to the shear-wave reflectivity: $A - B = 2R_S$.

Cross-plotting of the intercept (A) against gradient (B) is an efficient interpretation technique helping to identify the AVO anomalies. This method was developed by Castagna et al. (1998). It is based on two ideas: 1) the Rutherford and Williams (1989) AVO classification scheme described below and 2) the so-called Mudrock Line. The Rutherford-Williams classification subdivides the various amplitude-offset patterns into four classes (Figure 2.1 3):

Class 1: High-impedance contrast with decreasing AVO;
Class 2: Near-zero impedance;
Class 2p: Same as class 2, but with polarity change;
Class 3: Low impedance with increasing AVO;
Class 4: Low impedance with decreasing AVO.

If we assume that $V_p = cV_S$, which means that the Poisson's ratio is constant, and use the Gardner's equation relating the P-wave velocity to density: $\frac{\Delta\rho}{\rho} = \frac{1}{4}\frac{\Delta V_p}{V_p}$,

then Aki and Richards (2002) equations 2.1.(7, 8 and 9) lead to the following relationship between the intercept (A) and gradient (B):

$$B = \frac{4}{5} A \left[1 - \frac{9}{c^2}\right].$$

(2.1.15)

where c is a constant.

Using different values of c results in straight lines shown on the intercept/gradient cross-plots (Figure 2.1.4). By taking $c = 2$ for the approximate background, we obtain the commonly used $B = -A$ trend (also referred to as the "wet trend"; Castagna et al., 1998). This mudrock line on a cross-plot connects such P- and S-wave velocities that water-sands, shale and siltstones lie on this line, but gas-sands, igneous rocks, and carbonates lie off it (Fatti et al., 1994). Mudrock lines can be used to identify gas-sands in clastic sediments where there is no carbonate or igneous layers. Anomalous classes (deviations from this trend) can be plotted in different parts of the intercept/gradient cross-plot area (Figure 2.1.5). In the cases of limited time windows, shales and brine sand are likely to fall along the background trend. Gas sandstone tends to fall below the background trend (Castagna et al., 1998).
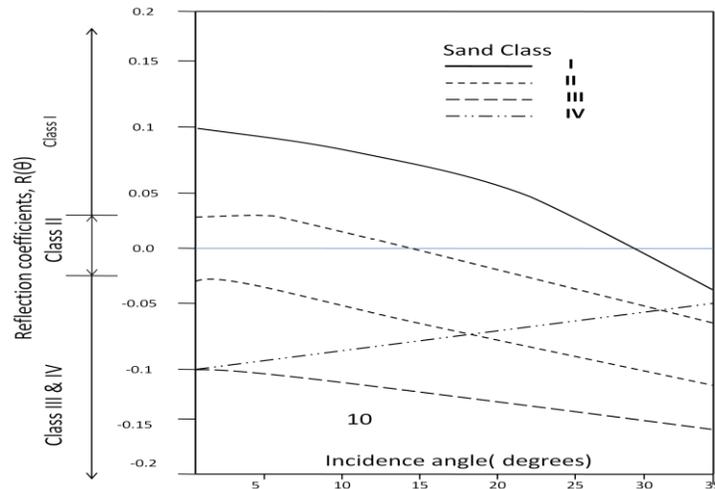
Figure 2.1.3. Rutherford/Williams AVO classifications for the top of gas sands modified from (Rutherford/Williams (1989))

30
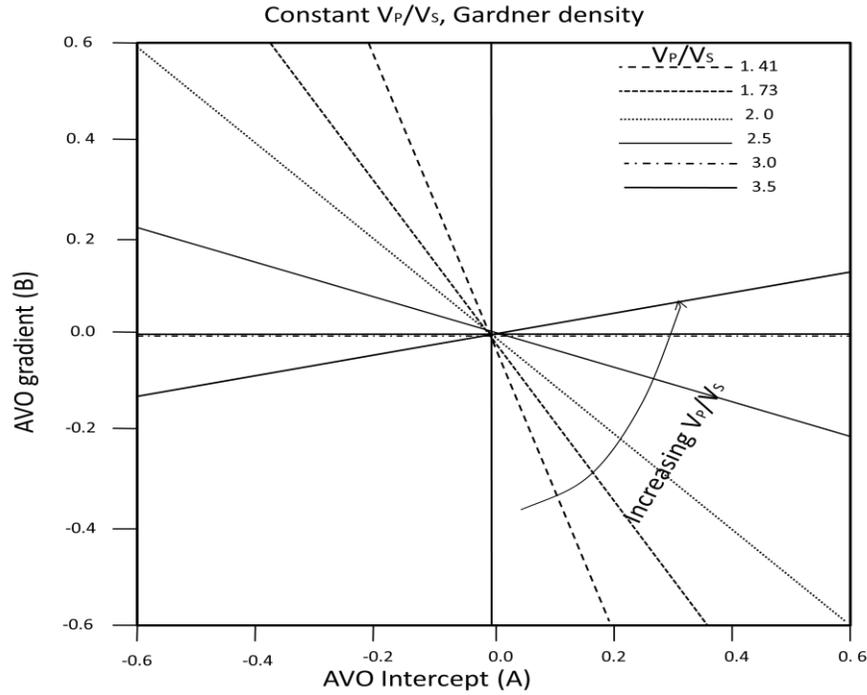
Figure 2.1.4 . Mudrock lines for a range of values of the *Vp/Vs* ratio and Gardner's equation on AVO intercept (*A*) and gradient (*B*) cross plot modified from (Castagna et al., 1998).
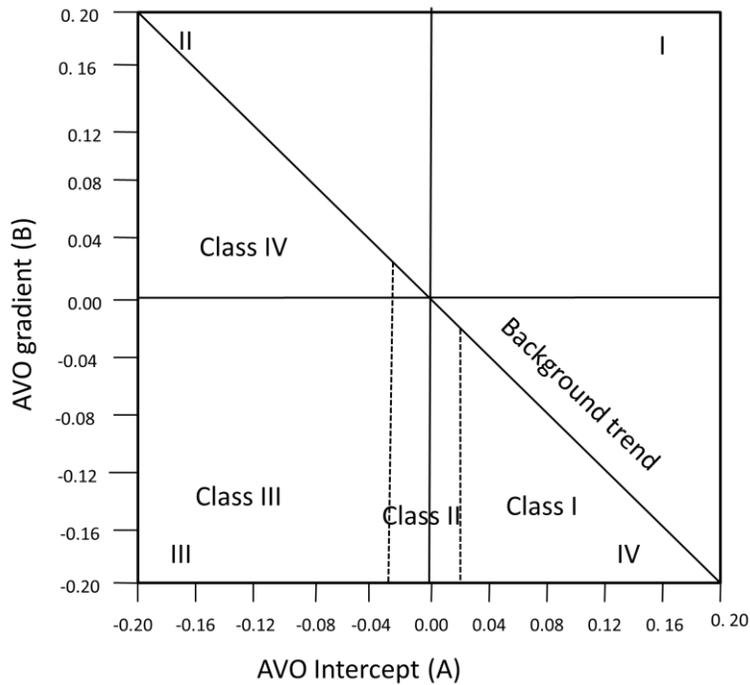
Figure 2.1.5. Four possible anomalous classes in an AVO intercept (*A*) and gradient (*B*) cross-plot. Reflections from the top of a gas-sand reservoir tend to fall below the background trend, while bottom of the gas-sand reflections tend to fall above the background trend redraw from (Castagna et al., 1998).

An alternate form of the Aki and Richards's equation was given by Fatti et al. (1994):

$$R(\theta) = c_1 R_P + c_2 R_S + c_3 R_D , \qquad (2.1.16)$$

where:

$$c_1 = 1 + tan^2\theta , \ c_2 = -8\gamma sin^2\theta, \ \gamma = \left(\frac{V_P}{V_S}\right)^2, \text{and } c_3 = -\frac{1}{2} tan^2\theta + 2\gamma^2 sin^2\theta,$$

and R_P and R_S are the P- and S-wave reflectivities:

$$R_P = \frac{1}{2}\left[\frac{\Delta V_P}{V_P} + \frac{\Delta\rho}{\rho}\right], \qquad (2.1.17)$$

$$R_S = \frac{1}{2}\left[\frac{\Delta V_S}{V_S} + \frac{\Delta\rho}{\rho}\right], \qquad (2.1.18)$$

$$R_D = \frac{\Delta\rho}{\rho}. \qquad (2.1.19)$$

Equation (2.1.16) allows us to calculate R_P and R_S from seismic data. The difference between the P-wave and S-wave reflectivities, (R_P - R_S), can be used as an indicator differentiating the shale over brine-sand and shale over gas-sand cases. R_P - R_S values are negative for shale over gas-sand and always more negative in the case of shale over brine-sand (Castagna and Smith, 1994). The R_P - R_S tend to be constant and near zero for non-pay reservoirs. The reflectivities R_P and R_S can also be transformed into two new attributes: the Fluid Factor (FF) and Lambda-Mu-Rho (LMR).

In a clastic sedimentary sequence, the Fluid Factor is defined so that it is high-amplitude for reflectors that lie far from the mudrock line and low-amplitude for all reflectors on the mudrock line. The equation defining the FF, according to Fatti et al. (1994) is:

$$\Delta F = \frac{\Delta V_P}{V_P} - 1.16\frac{V_S}{V_P}\frac{\Delta V_S}{V_S}, \qquad (2.1.20)$$

or:

$$\Delta F = R_P - 1.16\frac{V_S}{V_P}R_S. \qquad (2.1.21)$$

The FF equals zero when layers both above and below the reflecting boundary lie on the mudrock line, such as shale over brine sand. By contrast, the FF is nonzero when one of the layers lies on the mudrock line and the other one lies away from it (Fatti et al., 1994). In cases of gas sands, the FF will be non zero at both the top and bottom of gas.

32

The Lambda-Mu-Rho attributes (LMR) are defined so that the Lame's elastic parameters λ and μ are combined with density ρ in the form of $\lambda\rho$ and $\mu\rho$, as was first proposed by Goodway et al. (1997). Pre-stack seismic CMP gathers are inverted to extract the P-impedance and S-impedance, and from these impedances, the $\lambda\rho$ and $\mu\rho$ products are extracted. Starting from the equations for wave velocities:

$$V_P = \sqrt{\frac{\lambda+2\mu}{\rho}}, \tag{2.1.22}$$

$$V_S = \sqrt{\frac{2\mu}{\rho}}, \tag{2.1.23}$$

we have:

$$\mu\rho = (V_S\rho)^2 = Z_S{}^2, \tag{2.1.24}$$

$$(V_P\rho)^2 = Z_P{}^2 = (\lambda + 2\mu)\rho \quad , \tag{2.1.25}$$

and therefore:

$$\lambda\rho = Z_P{}^2 - 2Z_S \quad . \tag{2.1.26}$$

The λ parameter, or incompressibility, is sensitive to pore fluid, whereas the μ factor, or rigidity, is sensitive to the rock matrix. Goodway et al. (1997) shows a cross plot between $\lambda\rho$ and $\mu\rho$ which indicates that the clean gas sand usually has low $\lambda\rho$ (below 20 GPa) and quite high $\mu\rho$ (Figure 2.1.6). The interpretation of gas sand is improved by using LMR technique, which essentially correlates the P- and S-wave impedances. In order to create LMR volumes, one needs to start from P and S-impedances and use equations (2.1.24-26).
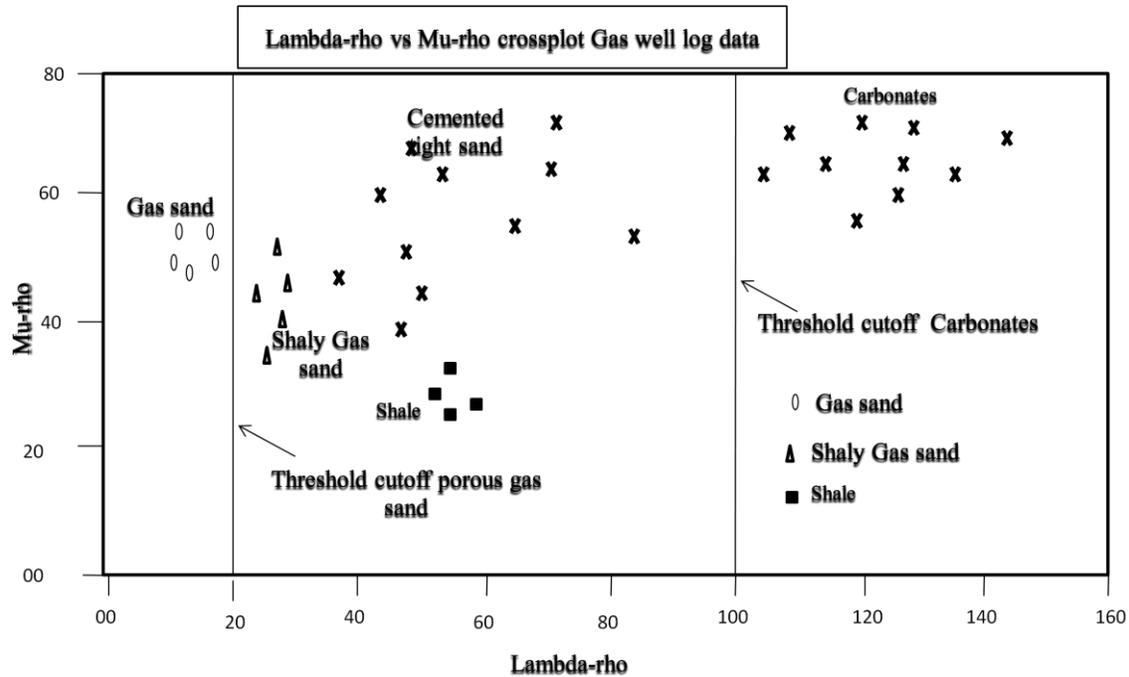
Figure 2.1.6. Interpretation of $\lambda\rho$ and $\mu\rho$ cross plot is improved in gas well (modified from Goodway et al., 1997)

2.2 Post-stack seismic inversion

Seismic inversion is the procedure for extracting underlying models of the physical characteristics of rocks and fluids. Generally, it is used to estimate the physical properties of the rocks by combining seismic and well-log data. In many cases, the physical parameters of interest are the impedance, velocity and density. Attributes based on inversion are also utilized to improve the interpretation of seismic sections.

Usually, the inversion procedure depends on some form of forward modeling generating the earth's response to a set of model parameters by using mathematical relationships. For example, we can produce a synthetic seismogram by using an elastic wave equation and a model with known parameters (velocity and density). For a known data set, the inversion consists in finding the model which reproduces the observed data set.

The post-stack AI inversion method started in the early 80's when algorithms of wavelet amplitude and phase spectra extraction became available (Lindseth, 1979). Inversion results showed high resolution, enhanced the interpretation, and reduced drilling risk

34

(Pendrel, 2006). Figure 2.2.1 illustrates the general principle of the post-stack AI inversion. In practice, many methods are used to perform post-stack AI inversion. Post-stack inversion can be subdivided into two main approaches: band-limited (iterative) inversion and broad-band inversion, which in its turn includes the model-based and sparse-spike approaches (Russell and Hampson, 1991).

Unfortunately, seismic AI inversion has several limitations. First, the seismic frequency band is limited to about 20 – 120 Hz, and therefore, the low- and high-frequency input data for inversion are missing. Well-log data provide the information at these missing frequencies. Non-uniqueness of the solution is another problem, and seismic data can lead to multiple possible geologic models which are consistent with the observations. In addition, in the inversion method itself, multiple reflections, transmission loss, geometric spreading and frequency-dependent absorption are ignored. The common way to reducing these uncertainties is to use additional information (mostly coming from well logs) which contains low and high frequencies and constrains the deviations of the solution from the initial-guess model. The final result therefore relies on the seismic data as well as on this additional information, and also on the details of the inversion methods themselves.

Geology　　　**Impedance**　　　**Reflectivity**　　　**Seismic**
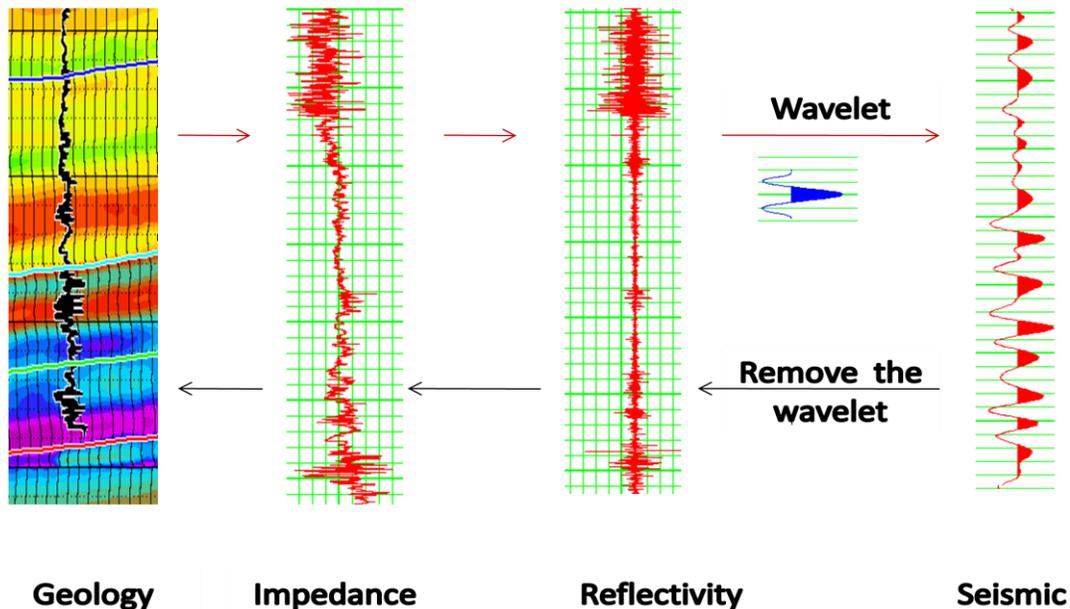
Figure 2.2.1. Concept of the Acoustic Impedance inversion. Red arrows show the forward modelling while black arrows indicate the inversion.

Knowledge of the wavelet and initial model are required in most of AI inversion algorithms. This information is extracted from the seismic and well-log data. The wavelet is the key element of the convolutional model describing the response of the subsurface to seismic sounding (Figure 2.2.1). In the frequency domain, the wavelet is defined by its amplitude and phase spectra, and therefore two tasks need to be performed in order to estimate the wavelet from seismic data:

- Determine the wavelet's amplitude spectrum;
- Determine its phase spectrum.

The amplitude spectrum is determined from the autocorrelation function of the data, under the usual assumption of "random" (or "white") reflectivity (Sheriff and Geldart, 1995). The phase spectrum is more difficult to determine. Two methods described below are usually used to extract the wavelet. In addition, VSP data and direct picks of strong reflections can also be useful for extracting wavelets.

The "statistical wavelet" extraction method allows obtaining the wavelet from seismic data alone. The phase spectrum is not reliably determined by this method, and it should be added as a separate parameter. Phase-correction methods need to be applied in conjunction with this approach, so that the phase of the seismic data is changed to zero-phase, constant-phase, minimum-phase or any other desired phase.

Once the phase is transformed, the amplitude spectrum is established as follows:

- ➢ Chose a time window;
- ➢ Compute the autocorrelation over the window;
- ➢ Compute the amplitude spectrum of the autocorrelation;
- ➢ Calculate the square root of the autocorrelation spectrum which approximates the amplitude spectrum of the wavelet;
- ➢ Apply the phase (zero, constant, minimum);
- ➢ Calculate the inverse FFT to produce the wavelet;
- ➢ Average the wavelet with wavelets calculated from other traces.

In contrast to the statistical wavelet, the well-log wavelet is extracted by correlating the log and seismic data and using a Wiener-Levinstson algorithm. This method provides accurate phase information at the well locations. It depends on the tie between the log and seismic data. The depth-to-time conversion also can cause misties which can affect the results. The wavelet extracted by using the well can be a "full" (meaning with the phase spec-

trum estimated from the data) or a constant-phase wavelet. Full-wavelet inversion requires density and sonic logs for each trace analyzed. This is provided by extrapolation and interpolation of the wells for each trace analyzed within the area.

In the H-R STRATA software, the procedure for well-log wavelet extraction is integrated with the inversion, and performed as follows:

> Extract sonic, density and seismic data analysis window;
> Calculate the impedance, from which calculate the reflectivities;
> Calculate the least-squares shaping wavelet which solves the following convolutional equation:

$$S = W * R + n, \tag{2.2.1}$$

where S denotes the seismic trace, W is the wavelet, R is the reflectivity, n is the random noise, and '*' denotes convolution in time. After estimating the wavelet, the inversion continues:

> Calculate the amplitude envelope of the wavelet by using the Hilbert transform;
> Sum the wavelet with the wavelets derived from other traces;
> Stabilize the calculated wavelet by removing the high-frequency spectral amplitudes whose amplitudes are less than ¼ of the maximum amplitude.

The constant-phase wavelet is a mixture of the statistical and full wavelets. Logs are used only to calculate a single constant phase. Such wavelet is calculated as follows:

> Calculate the amplitude spectrum using seismic data alone;
> Apply a series of constant-phase rotations to the wavelet;
> Calculate the synthetic trace for each phase rotation and correlate it with the seismic trace;
> Select the phase which produces the maximum correlation of the synthetics with the data.

Iterative AI inversion usually requires an initial model. This initial model provides the low- and high-frequency components missing from the seismic data, and it is also used to reduce the non-uniqueness of the solution. This model usually incorporates the interpreted seismic horizons and well-log data from all wells within the study area. In the H-R software, this model is created by using the following steps:

> Calculate the AI at well locations using the well-log data;
> Pick horizons to control the interpolation and to provide structural information for the model between the wells in the area;

37

➢ Use interpolation along the seismic horizons and between the well locations to obtain the initial AI model.

The spatial interpolation method used in the H-R software uses inverse-distance weighting and works as follows. Denoting any attribute (for example, the impedance) at well number i as L_i, the corresponding attribute L_{out} calculated at any location near the wells is given by the following equation:

$$L_{out} = \sum L_i * W_i , \qquad (2.2.2)$$

where the weights W_i are:

$$W_i = \frac{d_i^{-2}}{\sum d_i^{-2}} . \qquad (2.2.3)$$

and d_i is the distance between well #i and the location of interest. Power '-2' used in this weighting ensures that weights stay constant and equal 1 in the vicinity of each well. Another possible approach to well interpolation, which is more complex but is likely better justified geologically, uses Delaunay triangulations (Morozov and Ma, in press).

Once the wavelet and initial impedance model are estimated, the inversion can be performed. However, before the inversion, seismic amplitudes need to be scaled in order to represent the true reflectivities. In H-R STRATA software, scalars to scale the seismic amplitudes are calculated by using synthetics in the initial model, and measuring the average RMS (root-mean square) amplitudes for both synthetic and seismic amplitudes over the analysis window. The desired scalar is measured as the ratio of the RMS synthetic to seismic amplitudes, which is then used to multiply the traces.

In the following, three seismic inversion methods are applied to Blackfoot data set using the H-R STRATA software: band-limited (iterative), model-based and coloured inversion and Seismic inversion by well-Log Calibration (SILC). These methods are summarized below.

The first type of post-stack inversion that was developed was the band-limited recursive (iterative) inversion (Lindseth, 1979). This technique relies on the assumption that the seismic trace represents an approximation to the earth reflectivities:

$$R_i = \frac{Z_{i+1} - Z_i}{Z_{i+1} + Z_i} , \qquad (2.2.4)$$

If we have acoustic impedance Z_i of layer #i and seismic reflectivity from its bottom, r_i, it is possible to iteratively obtain the acoustic impedance in the next layer, Z_{i+1}:

$$Z_{i+1} = Z_i * \frac{1+r_i}{1-r_i}. \tag{2.2.5}$$

The AI for the first layer needs to be estimated from a continuous layer above the target area. In this method, the impedance for the nth layer can thus be calculated as follows:

$$Z_n = Z_1 * \prod \left(\frac{1+r_i}{1-r_i} \right). \tag{2.2.6}$$

Band-limited inversion is limited to the same frequency range as the seismic data. Therefore, the initial model needs to be added to seismic inversion. In STRATA H-R software, the band limited inversion is produced as follows:

1. The initial model is derived by filtering the impedance log from the wells (Figure 2.2.2). Interpolation is used to obtain a 3-D initial model using wells and seismic horizons. Seismic horizons are used to guide the interpolation.
2. Apply iterative equation (eq. 2.2.6) to seismic traces to obtain band- limited seismic inversion.
3. Final iterative inversion product is a combination of the initial model with the band-limited seismic AI (Figure 2.2.3).

An important limitation of the band-limited inversion is that seismic data must be zero-phase. The data could be transformed to zero-phase if an extracted wavelet is supplied. If the wavelet is ignored, the effects of its side lobes could be misinterpreted as lithology variations.
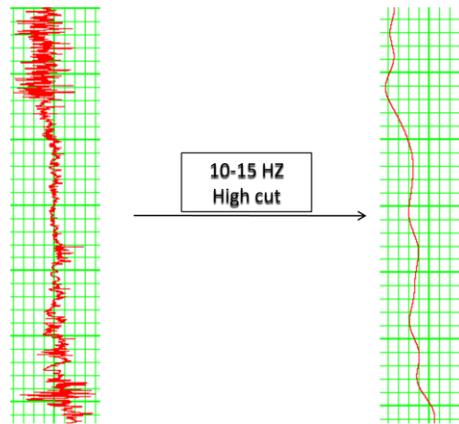
Figure 2.2.2. Initial model derived from an AI log by using high-cut filtering.
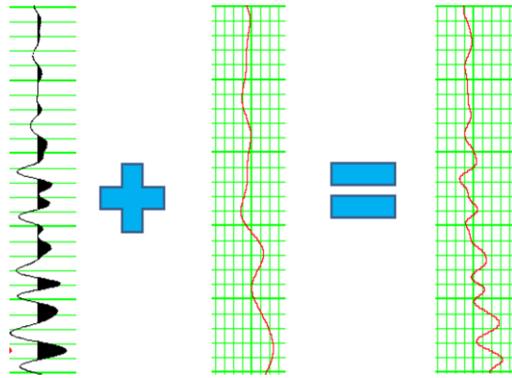
Figure 2.2.3. The inverted band-limited trace is added to the filtered model to obtain the final inversion.

The model-based inversion is also called blocky inversion. This method is based on the convolutional model (eq. 2.2.1).

If the noise is uncorrelated with the seismic signal, we can solve for the reflectivity satisfying this equation. This is a non-linear and band-limited equation which can be solved iteratively. An initial low-frequency model for AI is required to perform the inversion. This model is built from well data and seismic horizons as described above.

In H-R software, convolution between the initial model and the wavelet (*W*) is computed as follows:

1. Block the initial impedance using some selected block size, which represents the thickness of the layers. This layer thickness usually equals or exceeds the sample rate of the seismic data (Figure 2.2.4).

2. Convolve the wavelet with the blocky model to obtain synthetic seismic traces (Figure 2.2 5). These synthetic traces are deferent from the real trace because of two reasons. First, model reflectivities may be different from real-trace reflectivities. Second, the real trace contains measurement noise which is not included in the model.

3. Next, least-squares optimization is used to find the update in the impedances which minimizes the difference between the real and modeled reflectivity traces. This is achieved by analyzing the misfit between the synthetic traces and real traces and modifying the block size (thickness of the layers) and amplitude to reduce the error.

4. Repeating these steps until the lowest misfit between real seismic and synthetic is achieved.

Since the wavelet is known, and as long as the wavelet has the same phase as the seismic data, the convolution step above produces an accurate model for reflectivity. Therefore, the seismic data do not need to be zero-phase as in the band-limited method. Also, this method improves the effective resolution of the seismic (by effectively decon-volving the wavelet). On the other hand, the inversion result is affected by any errors in the extracted wavelet. Furthermore, the final inversion can be dependent on the initial model. This can be avoided by low-pass filtering the model passing only the data frequencies below 10 Hz. Like other inversion methods, the solution may be non-unique.
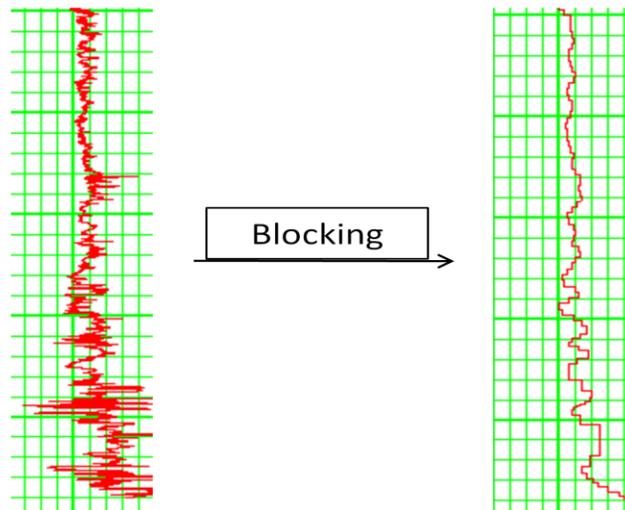
Figure 2.2.4. Blocky model derived from an impedance log.
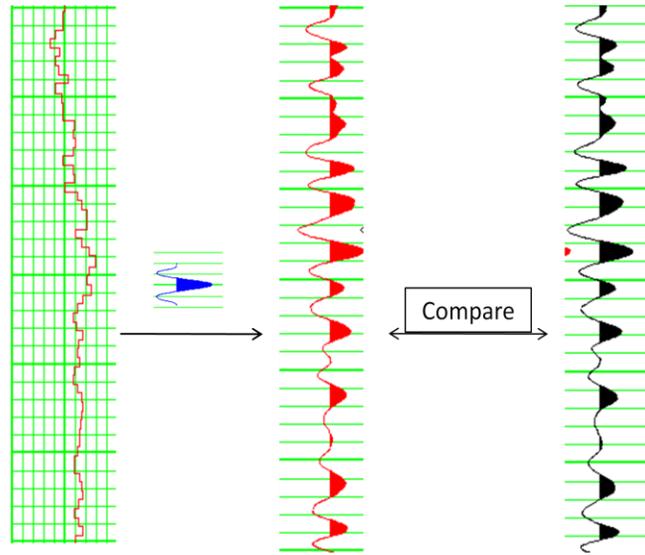
Figure 2.2.5. Convolution between a wavelet and blocky model to produce synthetic trace and compare it with seismic trace.

Coloured inversion was introduced by Lancaster and Whitcombe (2000). In this method, the inversion can be approximately represented as a convolutional (filtering) process. It simply uses an operator (O) in the frequency domain to transform the seismic traces (S) directly into impedance (Z):

$$Z = O * S.$$ (2.2.7)

This operator maps the seismic amplitude spectrum into the earth impedance spectrum. Spectra of AI logs from wells in the same area are typically close, which can be used to derive the spectrum of the operator. The phase of this operator is -90° (Lancaster and Whitcombe, 2000), so that it integrates the reflectivity series into impedance. Using the H-R software, the operator is derived as follows:

1. Plot the acoustic impedance and frequency on log-log scale by using the data from all wells in the area (Figure 2.2 6);

2. Predict a line to fit amplitude spectrum of acoustic impedance to represent the impedance spectrum in the subsurface in the $Z_{log} \propto f^{\theta}$ form;

3. Seismic spectrum is calculated from the seismic traces near the wells. These two spectra are used to calculate the operator spectrum which transforms the seismic spectrum into the average impedance spectrum (Figure 2.2 7);

42

4. The final spectrum is combined with a -90° phase shift to create the desired operator (Figure 2.2 8).

Once the operator is derived, convolution is applied to the seismic data in order to produce the band-limited inversion result. Adding the low-frequency model gives the final inversion.

Coloured inversion is fast and suitable for application to 3-D datasets. The operator uses well-log impedances, which can be analysed, edited, and made consistent with the known impedances in the area. Since the procedure includes only a single convolution applied to the seismic data, this impedance result may also be useful as an initial model for other types of inversion.
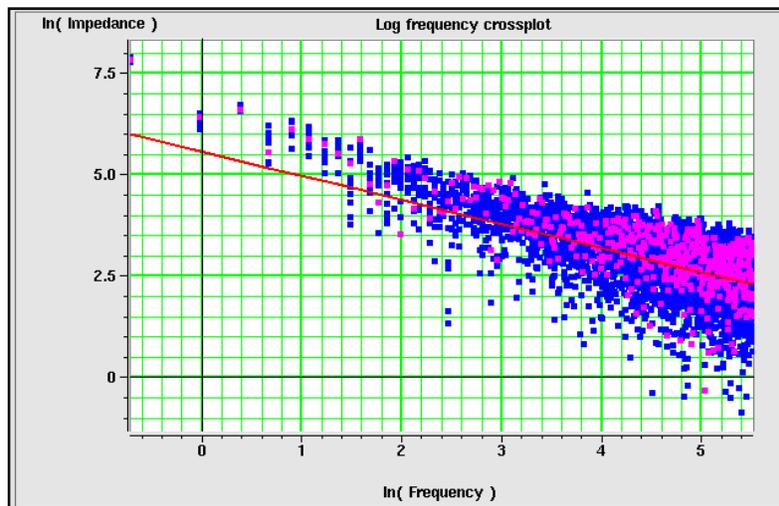
Figure 2.2.6. AI from all wells (blue), one selected well (pink) and frequency on log-log scale.
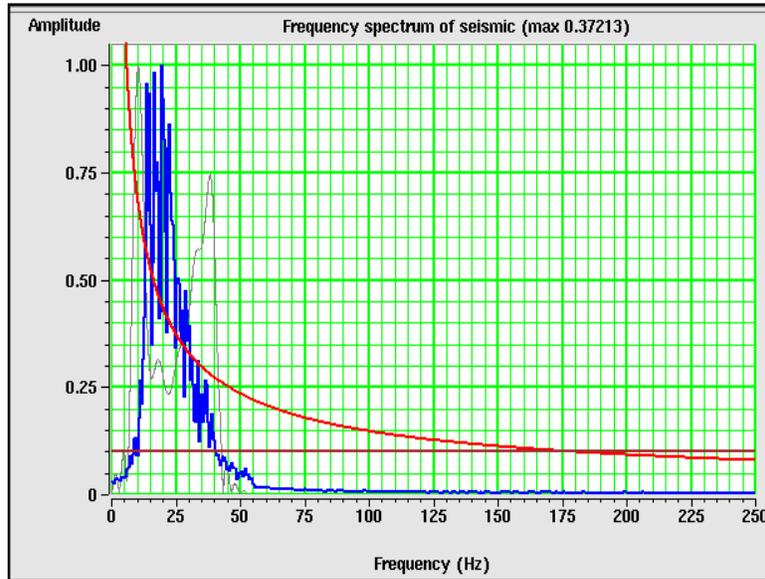
Figure 2.2.7. Seismic spectra near the wells (blue). Red line corresponds to the f^θ AI spectrum derived in Figure 2.6. The operator spectrum (black) is the ratio of these two spectra.
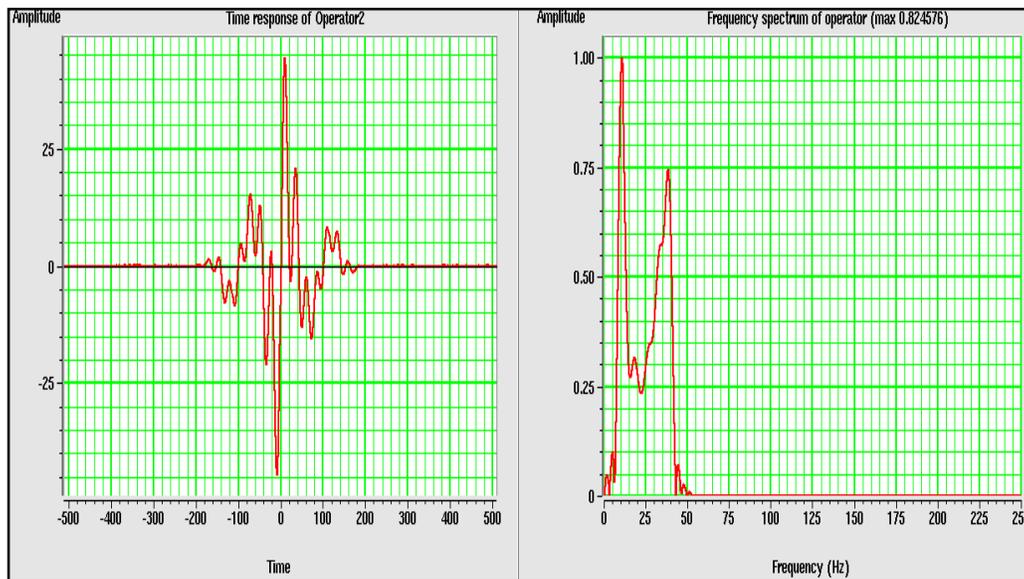
Figure 2.2.8. Frequency spectrum of the operator (right) and its time response (left).

In addition to the three AI inversion methods available in the H-R software, a new method developed by Morozov and Ma (in press) and called Seismic Inversion by well-Log Calibration (SILC) was also applied to the Blackfoot dataset. The method is close to coloured inversion in the sense that it only uses a single-pass forward computation in order to produce an AI image. Therefore, this method is efficient, stable, and fast. Unlike coloured inversion, it matches the AI spectra from each individual well, and uses the Delaunay triangulation to interpolate between the wells in a 2D study area.

The SILC method utilizes well-log data as a calibration applied to the seismic data (Figure2.2.10). First, it is noted that by using the iterative inversion (eq 2.2.4), the convolutional equation is satisfied, but the resulting impedances may still be scaled with a generally slowly varying factor. Also, the seismic reflectivities may also be arbitrarily scaled, and the low-frequency information is still missing from the iterative inverse. Both of these slowly-varying parameters (the background model impedance and amplitude scalar) can be recovered from well-log data, as shown in Figure 2.2.9. As a result, the SILC time-domain pattern comes from the seismic data, and the amplitude spectrum of AI corresponds to that of the log throughout the entire frequency interval from zero to the upper limit of the seismic spectrum.

Figure 2.2.10 shows the principle of the calibration between the seismic data and well log data. The values of AI at frequencies bellow the seismic band are extracted directly from the well log, and seismic AI amplitudes at frequencies within the seismic band are also scaled by utilizing the amplitude for the same frequencies from well log data. This procedure is done using a relatively narrow, AGC-like time window through the impedance traces of seismic and well log (Figure 2.2.11).

Seismic and well-log data have to be tied together by using interpreted seismic horizons before applying inversion. In SILC procedure, they are transformed into a common "stratigraphic time" t_s, which is the two-way travel time or depth at a selected well, so that t_s becomes constant along any single horizon. With all times thus equalized, the SILC inversion is applied as follows:

Continuous amplitude spectrum from log AI

Phase from log AI

Phase from seismic AI

Randomized phase from log AI

Seismic band

Frequency
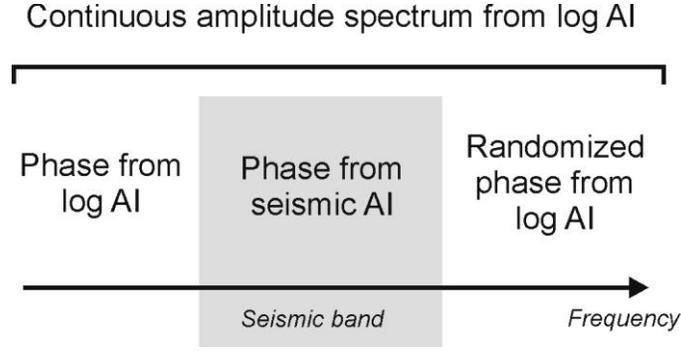
Figure 2.2.9. Schematic diagram of the SILC inversion method in application to AI.

1. Build the AI for the seismic traces (eq 2.2.4) and from the well log (Figure 2.2.11).

2. Define a series of overlapping narrow zero-phase band-pass filters $F_i(f)$ beyond the frequency band of seismic data. As a result the sum of all filter amplitudes equals 1 at any frequency in the seismic band and these frequencies start from zero f: $\sum_i F_i(f) = 1$ (Figure 2.2.11).

3. Filter the log (denoted $u^{\log}(t_s)$ below) and seismic impedance $(u^{\text{seismic}}(t_s))$ series within each of these frequency bands to produce their band-limited versions $u^{i\log}(t_s)$ and $u^{\text{seismic}}(t_s)$, respectively (Figure 2.2.11);

4. For each of the filtered log and seismic records, determine their time- (or depth-) variant amplitudes, $A^{\log}(t_s)$, $A^{\text{seismic}}(t_s)$) respectively using time window as shown in Figure 2.2.11;

5. Optionally, randomize the retaining log frequencies above the seismic band (how-ever, this option is risky and was not used in this study);

6. Construct the final synthetic log at the position of seismic trace:

$$u(t_s) = \sum_i [(1 - w_i)u_i{}^{log}(t_s) + \frac{A_i{}^{log}(t_s)}{A_i{}^{seismic}(t_s)} w_i u_i{}^{seismic}(t_s)].(2.2.8)$$

where weight w_i is equal 1 within the seismic band and 0 outside of it.
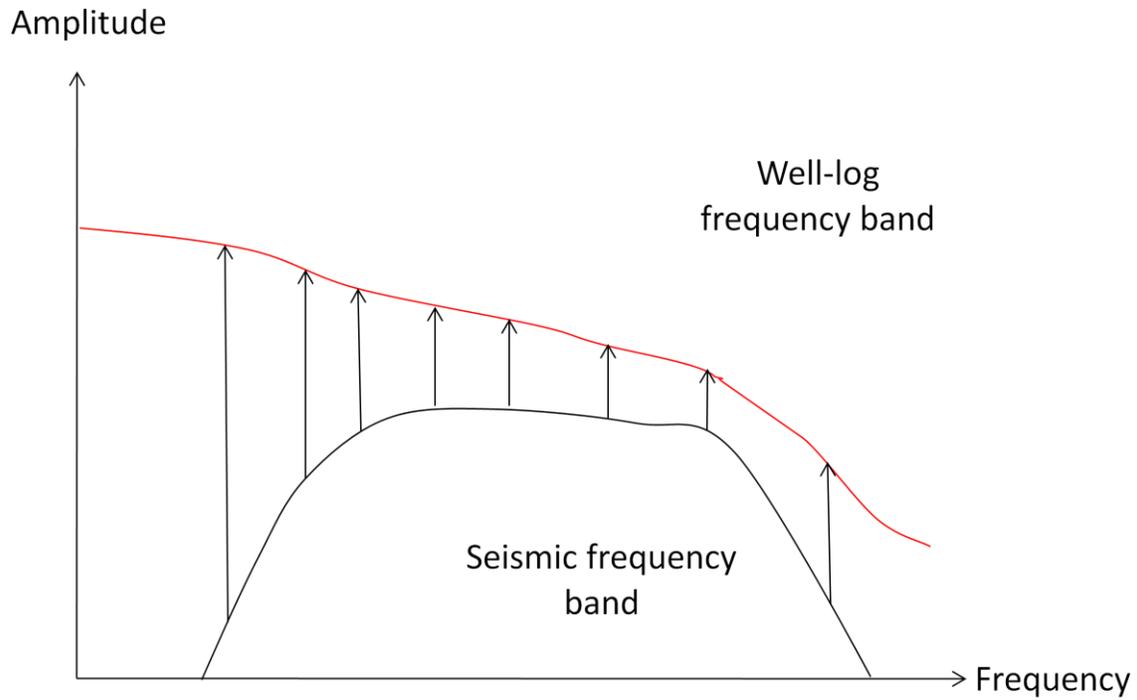
Figure 2.2. 10. Principles of scaling amplitudes between the seismic and well-log bands in SILC inversion.
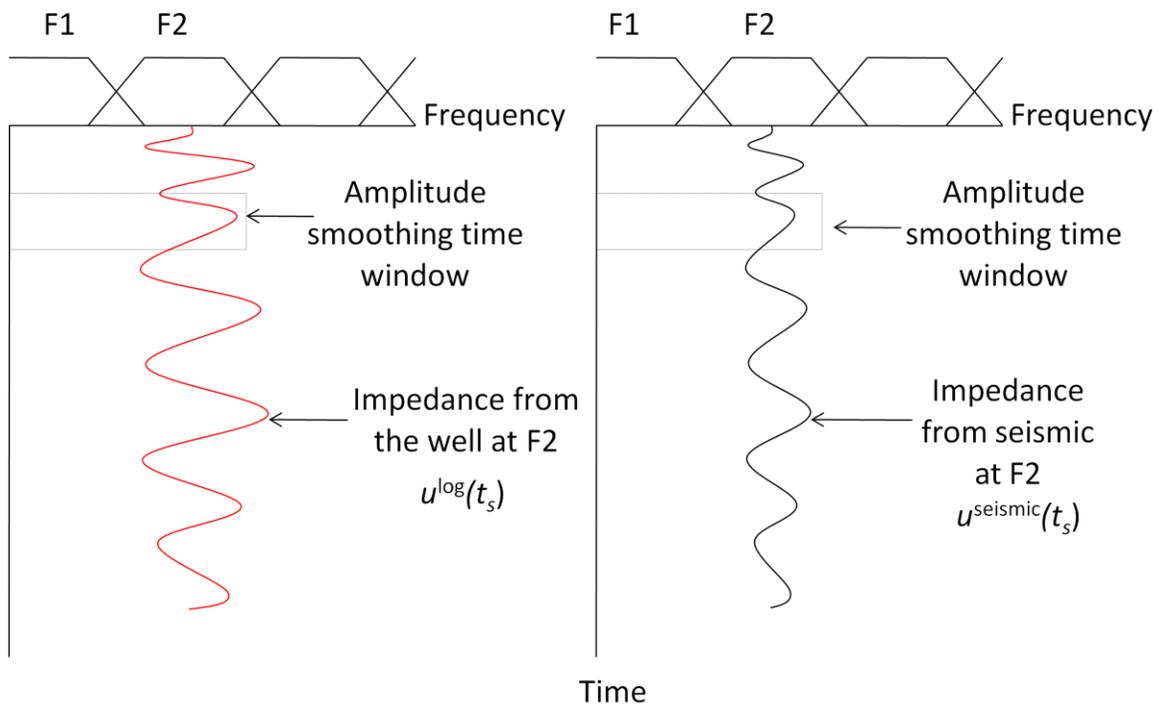
Figure 2.2. 11. SILC inversion steps from building AI, filtering AI and calculate time-variant amplitude scale.

The advantages of the SILC approach are in its including no iterations, matrix inversion, deconvolution, or spectral divisions. Therefore the resulting solution is unique (in the sense of being entirely controlled by the data), stable, fast, and does not use starting models. The procedure also contains no user parameters except the limits of the seismic frequency band. In addition, intermediate steps (such as horizon-flattened data and inversion using only seismic or log data) can be readily inspected for quality control and edited if needed.

2.3 Elastic Impedance

The Elastic impedance (EI) represents a generalization of the AI to nonzero incidence angles. Because P/S mode conversions are significant at oblique incidence, EI is a function of the P- and S-wave velocities, density and incident angle. EI can be used to calibrate and invert nonzero-offset data in the same way as AI does for zero-offset data (Connolly, 1999). Similarly to most other pre-stack attributes, EI is derived from the small-contrast Aki and Richards equations (2.1.3).

Connolly (1999) was the first to use range-limited stack interpretation to invert for an EI, and his form of EI is the most broadly used to date. By considering the incidence angle θ at any layer as fixed throughout the reflection sequence, an angle-dependent EI can be defined from equations. 2.1.(3, 4, 5, and 6) by an analogy to AI (Connolly, 1999):

$$A = \frac{1}{2}\frac{\Delta AI}{AI},$$ (2.3.1)

$$R(\theta) \approx \frac{1}{2}\frac{\Delta EI}{EI} \approx \frac{1}{2}\Delta ln(EI),$$ (2.3.2)

$$K = [\frac{V_S}{V_P}]^2,$$ (2.3.3)

By assuming this K to be constant, Connolly (1999) obtained the following equation for EI:

$$EI(\theta) = V_P^{(1+\tan^2\theta)}V_S^{-8k\sin^2\theta}\rho^{(1-4k\sin^2\theta)}.$$ (2.3 4)

Figure 2.3.1 shows that the EI decreases with oil saturation faster than AI (Connolly, 1999).

Connolly's EI (equation 2.3.4) has several fundamental problems, such as the dependence of its dimensionality on the angle (Whitcombe, 2002) or the unrealistic assump-

tions of *K*= const and θ = const. Several other types of EI were proposed (VerWest et al. 2000; Ma, 2003; Santos and Tygel 2004; VerWest, 2004; Whitcombe et al., 2004; Morozov, in press). However, all of them except one (Morozov, in press) define the EI by phenomenological integration of the reflectivity series and contain normalizations (Whitcombe, 2002) that reduce the above inconsistencies. The EI (equation 2.3.4) is implemented in Hampson-Russell software and appears to be most commonly used. Therefore I consider it representative of the various EI approaches and use in this study.
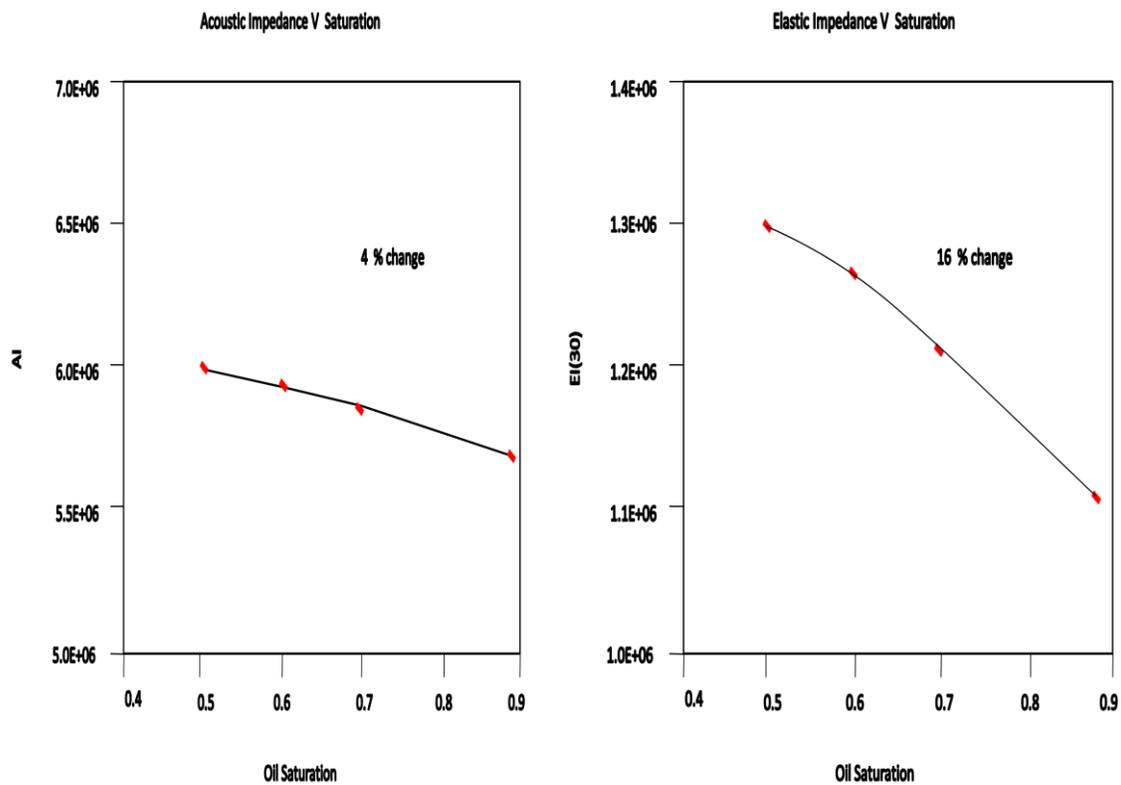
Figure 2.3.1. Compared to AI, EI at 30° angle shows a steeper decrease with increasing oil saturation. Modified from (Connolly, 1999).

Range-limited stacking is often used to extract the EI from pre-stack seismic data. In this process, CMP gathers are stacked within constant-offset or angle bins. By creating near- and far-offset or angle stacks, we can compare them to recognise the effects of AVO

49

properties, as well as to determine the best attributes for estimate lithological and fluid parameters.

Transformation of the CMP gathers from the offset to angle domain is the first step in the EI and AVO analysis. The seismic data are recorded as a function of offset (x), and therefore to transform from constant offset to constant angle (θ), a relationship is needed between these quantities. Two methods are usually used for this transformation: the straight-ray method and the ray-parameter method. The straight-ray method uses the following equation:

$$tan\theta = \frac{X}{V_{RMS}\, t_0}\,, \qquad\qquad (2.3.5)$$

where V_{RMS} is the RMS velocity for the layer, and t_0 is the two-way reflection time. This formula corresponds to reflection rays considered as traveling at straight paths from the surface to the reflection point. If we know the RMS velocity to the layer of interest, offset and the two-way travel time, we can solve for the angle.

In the ray-parameter method, the ray to the reflection point is assumed to be bending (refracting), with the $V_{int}/\sin\theta$ (where V_{int} is the interval velocity) constant along the ray according to the Snell's law. Therefore:

$$sin\theta = \frac{XV_{int}}{tV_{RMS}{}^2}\,, \qquad\qquad (2.3.6)$$

Range-limited stacking using constant offsets or constant angles is very robust and avoids misaligned event problems, which means such data can be inverted at constant offsets.

To perform EI inversion in H-R software, we start with unstacked CMP gathers. The processed seismic gathers are analysed in the AVO program to produce common-angle stacks, which are further passed to the post-stack inversion program (STRATA). Integration of the reflectivity series is the same as in the AI case, but calibration with well-log data is done differently, by using the EI-type equations 2.3 (3 or 4). The elastic impedance steps are similar to the AI; and the following list shows them in H-R software:

1. Generate EI(θ) at the well locations for near and far stack.
2. Extract the wavelet (as a function of angle θ) for both near and far stacks.
3. Use seismic horizons as structural-geology guide in the area.
4. Build the EI initial models for each angle.

5. Apply the QC (quality control) at well locations to check the quality of EI(θ) inversions and compare the results with EI at the well locations.

6. Apply the inversion to the near- and far-angle stacked data.

Cross-plotting is another valuable tool to use in the interpretation. By cross-plotting the near-angle versus the far-angle stacked amplitudes, or the inverted EI at the near and far offsets, we can use them to estimate the presence of gas sands within the seismic section.

2.4 Pre-stack inversion (simultaneous)

In simultaneous inversion, pre-stack CMP gathers are utilized directly to determine the compressional impedance (Z_P), shear impedance (Z_S) and density (ρ). In wet clastic rocks, the *P*- and *S*-wave impedance are related. According to Castagna's equation (2.4.1) there is a linear relationship between the *P*-wave velocity and *S*-wave velocity in background trend (Castagna et al., 1985). Gardner's equation (2.4 2) also shows the relation between *P*-wave velocity and density in the same case (background trend) (Gardner et al., 1974). Therefore, simultaneous inversion could use these linear relationship forms to couple the variables as shown in equations (2.4.3 and 4) (Figure 2.4 1).

$$V_P = 1.16V_S + 1360 \, , \tag{2.4 1}$$

$$\rho = 0.23V^{0.25}, \tag{2.4 2}$$

$$ln(Z_S) = k \, ln(Z_P) + k_C + \Delta L_S \, , \tag{2.4 3}$$

$$ln(\rho) = m \, ln(Z_P) + m_C + \Delta L_D. \tag{2.4 4}$$

where coefficients ($k, k_c, m \text{ and } m_c$) are calculated using well log data in the area (Figure 2.4. 2). ΔL_S and ΔL_D represent the deviation from background trend as a result of hydrocarbons.
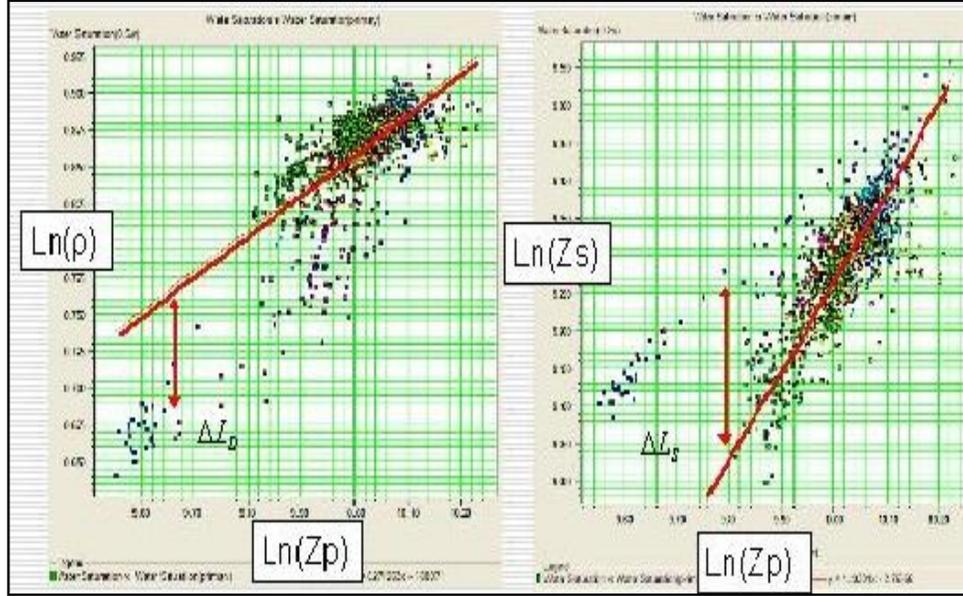
Figure 2.4.1. Cross-plot between ln(Z_P) and ln(Z_S) (right) and ln(Z_P) and ln(ρ), showing that Z_S and ρ are the linearly related to Zp; Values of ΔI_D and ΔI_S indicate the deviations away from background trend (red line) in case of fluid anomalies (CGG VERITAS workshop, 2008).

Now, we can derive simultaneous inversion starting with Fatti's version of the Aki-Richards' equations 2.1 (8, 9, 10 and 11). These equations model the reflection amplitude as a function of incident angle (Figure 2.4 2). Using these equations and the previous relationships between the *P*-impedance, *S*-impedance and density changes Fatti's equation to:

$$T(\theta) = \hat{C}^1 W(\theta) * DL_P + \hat{C}^2 W(\theta) * DL_S + C_3 W(\theta) * DL_D . \qquad (2.4.5)$$

where: $\hat{C}_1 = \frac{1}{2} c_1 + \frac{1}{2} K c_2 + m c_3$, $\hat{C}_2 = \frac{1}{2} c_2$, $W(\theta)$ is the wavelet at angle θ, D is the differentiation derivative operator, and $L_P = ln\ (Z_P)$.

52
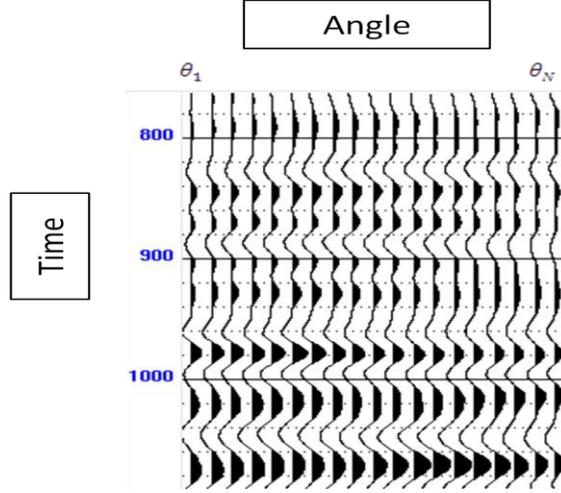
Figure 2.4.2. CMP gather showing the amplitude as a function of angle as described in Fatti's

equation (2.4.5).

Note that if the angle is zero then this equation reduces to zero-offset (model-based) inversion. In equation 2.4.5, we invert for L_P, L_S and L_D. In practice, simultaneous inversion involves the following steps by using the H-R software:

1) From CMP gathers, we have the following information:
    a. A set of N angle traces;
    b. A set of N wavelets for each angle;
    c. Initial model values for Z_P.
2) Calculate the coefficients values for k and m using well-log data.
3) Start with initial model guess.
    $$[\ L_P \quad \Delta L_S \quad \Delta L_D\ ]^T = [log\ (Z_P) \quad 0 \quad 0]^T$$
4) Apply the inversion.
5) Calculate the final values of Z_P, Z_S and density:

$$Z_P = exp(L_P), \hspace{5cm} (2.4.6)$$

$$Z_S = exp(kL_P + k_C + \Delta L_S), \hspace{3.5cm} (2.4.7)$$

$$\rho = exp(mL_P + m_C + \Delta L_D). \hspace{3.5cm} (2.4.8)$$

Note that the initial model guess representing the initial model of P-impedance, while ΔL_S and ΔL_D are initialized with zero values in this iteration.

3   Inversion and AVO attributes in Blackfoot 3D seismic dataset

Seismic observations are critical for the present study because they provide details about the post and pre-stack attributes. This study relies on the 3D seismic dataset processed as described in Chapter 1 and whose data are sorted into CMP gathers. In this Chapter, pre-stack attributes, such as intercept (A), gradient (B), and their combinations are extracted from these gathers,. In addition, the same gathers will be used to perform pre-stack inversion. Range-limited stacks are also computed by partial stacking of the CMP gathers at constant offsets and/or angles, which are called the near- and far-offset or angle stacks, respectively. These stacked data (near and far) are used in the EI inversion. The CMP gathers are also stacked for all offsets to provide the standard post-stack data or zero-offset stacks, which are used for the AI inversion. Eleven wells are also correlated with seismic data (Table 3.1). The Gardner equation (2.4 2) is used to estimate the density logs, which are missing in some wells. S-wave logs are only present in wells 4-16 and 9-17, and therefore Castagna's equation (2.4 1) is used to estimate the missing S-wave logs in other wells

.

Table 3.1. Table of the Blackfoot area wells with, *P*-wave log, *S*-wave log and density logs

Well #	P-wave log	S-wave log	Density
4-16	4-16	4-16	4-16
1-8	1-8	-	1-8
11-8	11-8	-	11-8
12-16	12-16	-	-
14-9	14-9	-	14-9
16-8	16-8	-	16-8
8-8	8-8	-	-
9-17	9-17	9-17	9-17
1-17	1-17	-	1-17
13-16	13-16	-	13-16

Correlating the wells to the seismic data is the first step we need to apply before the post and pre-stack inversion and attribute analysis can be performed. Because the well-log data are usually recorded at higher frequencies than seismic and also because of the measurement errors in stacking velocities, slight differences occur between the well-log horizon times and the corresponding seismic records. The correlation simply consists in matching the corresponding events between the real and synthetic seismic traces, which are generated from the well-log data at the well locations. Such correlation is performed for all wells in the area by using the wavelet extracted from seismic and well-log data, and by shifting and stretching the corresponding well logs. After the matching between wells and seismic in the area is achieved, I pick several horizons to provide the structural and geological guidance for inversion. Once the correlation is completed and horizons picked, the data are ready for application of the inversion and attribute analysis as described below.

3.1 Inversion of post-stack seismic data

Post-stack seismic inversion operates on NMO-corrected and stacked CMP seismic data. Wavelet extraction is the first step of this inversion. As described in Chapter 2, two types of wavelets can be used to perform the inversion: statistical and well-log derived. First, I derived a statistical wavelet, which was based on measuring the autocorrelations of the seismic data and assuming that the earth reflectivity is "white" (has zero autocorrelations at non-zero lags). Because of the lack of any other information, the phase of such wavelet is usually set to zero, assuming zero-phase processing of the input data. I used the following parameters for measuring the data autocorrelations (Figure 3.1.1):

- ➢ Start time: 800 ms;
- ➢ End time: 1200 ms;
- ➢ In-line range to derive the autocorrelations: 55 to 115;
- ➢ Cross-line range: 95 to 195;
- ➢ Wavelet length: 150 ms;
- ➢ Taper: 20 ms;
- ➢ Phase: zero.
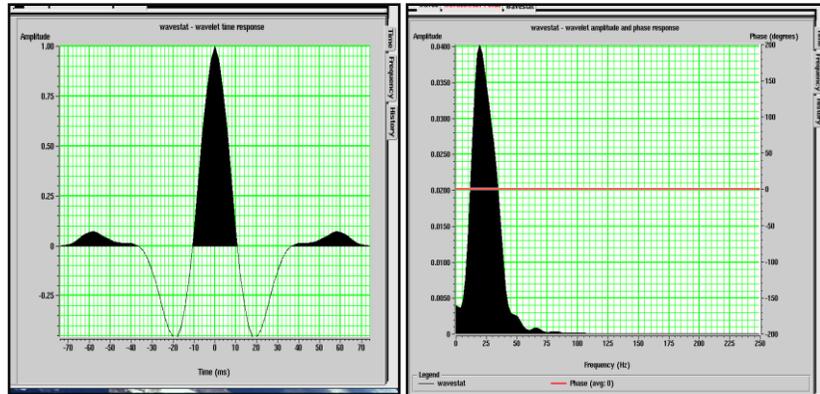
Figure 3.1.2. Statistical wavelet extracted from seismic data in the time domain (left) and frequency domain (right). Note that the wavelet is symmetrical in time and has zero phase.

In these parameters, the time range of 800 - 1200 ms was suitable for our target, which is between 1000 and 1100 ms. Some of the noisy data at the edges of data coverage were excluded. The wavelet length corresponded to the inversion window length.

Once the wavelet was extracted, well-log correlation was performed for each well. The correlation was applied as follows:

- ➢ A synthetic trace was generated and compared to the real seismic trace nearest to the well location;
- ➢ Time stretching and squeezing was applied to align the seismic and well-log events;
- ➢ Correlation coefficient was measured between the seismic and adjusted well-log synthetic traces.

Table 3.1.1 shows the correlation percentage levels for each well with the corresponding seismic data. The correlations were good for all wells (above 84%). As an example, Figure 3.1.2 shows the correlation of the reflection synthetics with band-pass filtered well logs at well 1-8.

Table 3.2. Correlation between the synthetic trace and real trace at well locations

using the statistical and full wavelets.

Well #	Correlation between wells and statistical wavelet %	Correlation between wells and full wavelet %
4-16	87	89
1-8	84	88
11-8	81	87
12-16	84	84
14-9	88	90
16-8	86	88
8-8	87	90
9-17	86	87
1-17	90	91
13-16	87	84
5-16	84	87
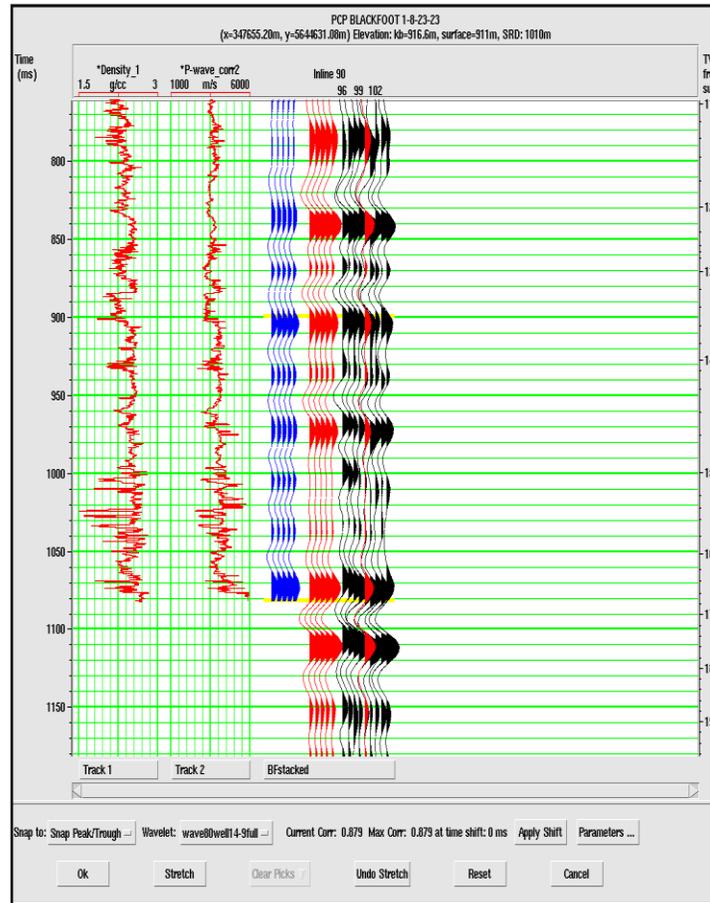
Figure 3.1.3. Correlation at well 1-8 by using the statistical wavelet. The curves, left to right, show: well density log, *P*-wave velocity log, the blue trace represent the synthetic trace from the well and the red represents the seismic trace, for easy comparison each trace presented 5 times. The correlation level is 84%.

For comparison, I also extracted a full wavelet by using the well-log data. By contrast to the statistical wavelet, this wavelet includes an estimate of the phase obtained by matching the real and synthetic phase spectra at the well location. Such wavelet can only be computed by using one well at a time. Therefore, I extracted the full wavelets for each well individually, correlated them with the seismic data, and selected the one showing the best correlation as our final full wavelet. Well 14-9 gave the best wavelet that also correlated well with all other wells. The parameters of this wavelet are as follows (Figure 3.1.3):

- ➢ Start time: 800 ms;
- ➢ End time: 1200 ms;
- ➢ In-line range: 55 to 11;

59

> ➢ Cross-line range: 95 to 195;
> ➢ Filter length: 80 ms;
> ➢ Taper: 15 ms;
> ➢ Average phase.

The correlation levels using the full wavelet for all wells is also shown in Table 3.1.1. Note that the phase of this wavelet is small (~4°), and therefore the wavelet is close to the statistical wavelet. The full wavelet slightly improves the correlation for most wells. Figure 3.1.4 shows its correlation with the seismic data, performed in the same well 1-8.
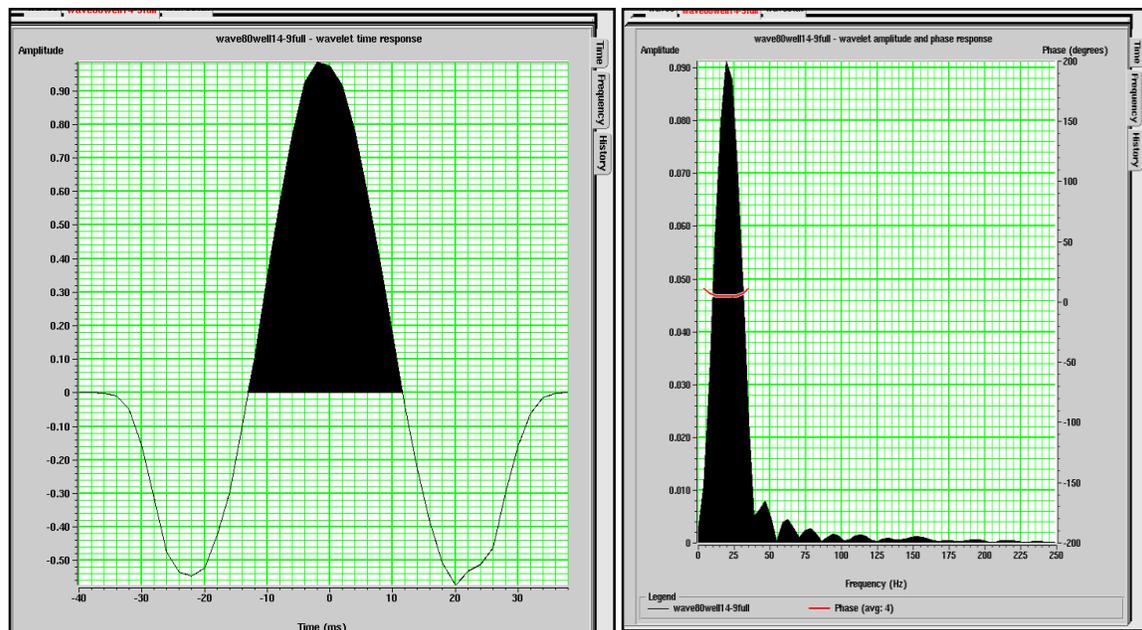
Figure 3.1.4. Full wavelet in the time (left) and frequency (right) domains extracted by using well 14-9 and seismic data. Compare to Figure 3.1.1.
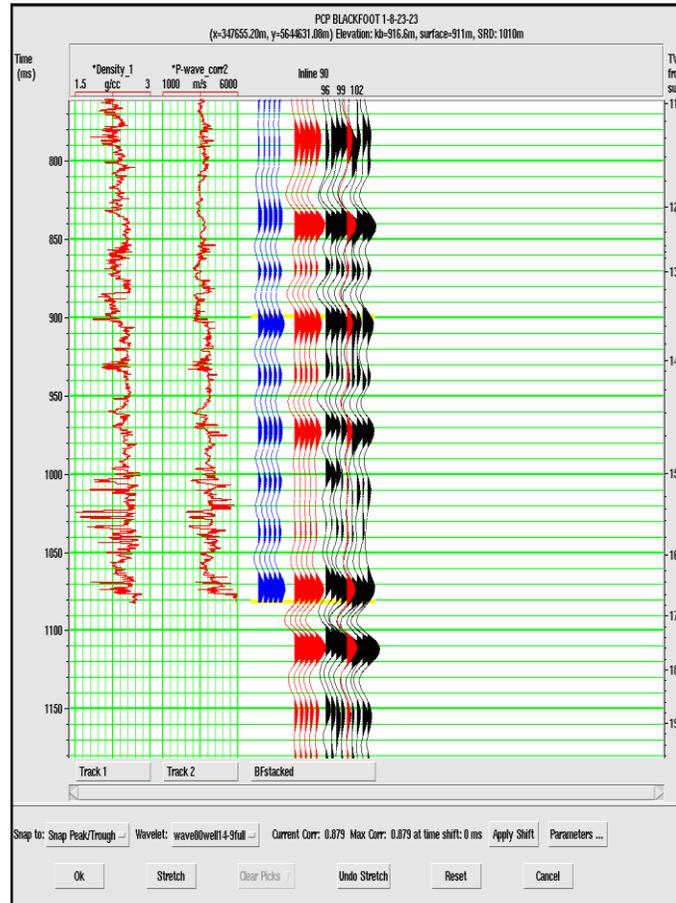
Figure 3.1.5. Correlation at well 1-8 using the full wavelet. The blue trace represents the synthetic trace from the well and the red represents the seismic trace. The correlation coefficient is 88%. Compare to Figure 3.1.2.

After a satisfactory wavelet was extracted, the log-to-seismic correlation procedure was completed and horizons picked. Determination of the starting model was the next step of the inversion. This model was built by interpolating the AI from eleven well locations into the in-lines, cross-lines shown in Figure 1.5.5. The density logs in wells 8-8 and 12-16 were blocked (averaged within depth intervals) in the original dataset, and therefore the Gardner equation (2.4.2) was used to calculate the detailed density logs for these two wells. Four interpreted seismic horizons were introduced to guide the structural information for the interpolation (Figure 3.1.5). As soon as I had all the required information for the model, I ran the program to construct the model.

A 10-Hz low-pass filter was applied to the model for two reasons. First, the low-frequency impedance trend was required in order to recover the low frequencies missing

from the stacked seismic data. In addition, the impedances above ~10-Hz frequencies should be only obtained from seismic data, and therefore this frequency band should be removed from the well-log data while building the starting model. The reason for using the 10-Hz cut-off was that the spectrum of stacked seismic section showed no data below this frequency (Figure 3.1.6). Figures 3.1.7 and 1.1.8 show two AI cross-sections of the unfiltered and filtered models, respectively. Figures 3.1.9 show horizontal slices of the impedance at the 1065-ms time level, averaged within a 10-ms window in the unfiltered and filtered model, respectively.
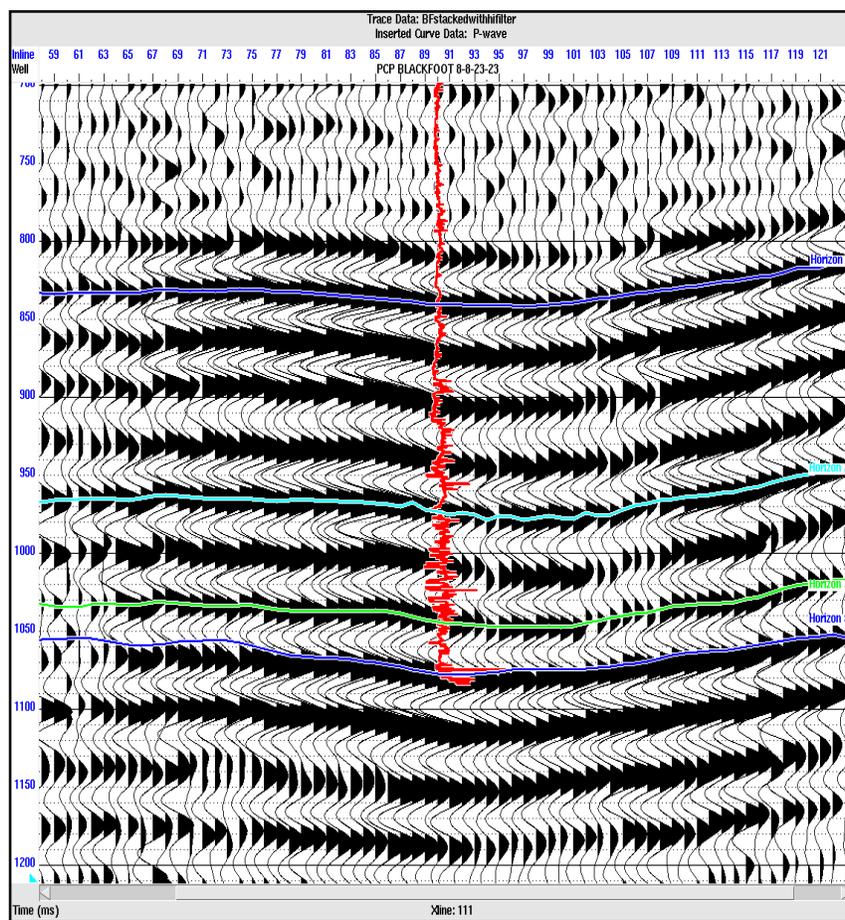
Figure 3.1.6. Seismic section showing the horizons used for interpolations and inversion and AI log from well # 8-8.
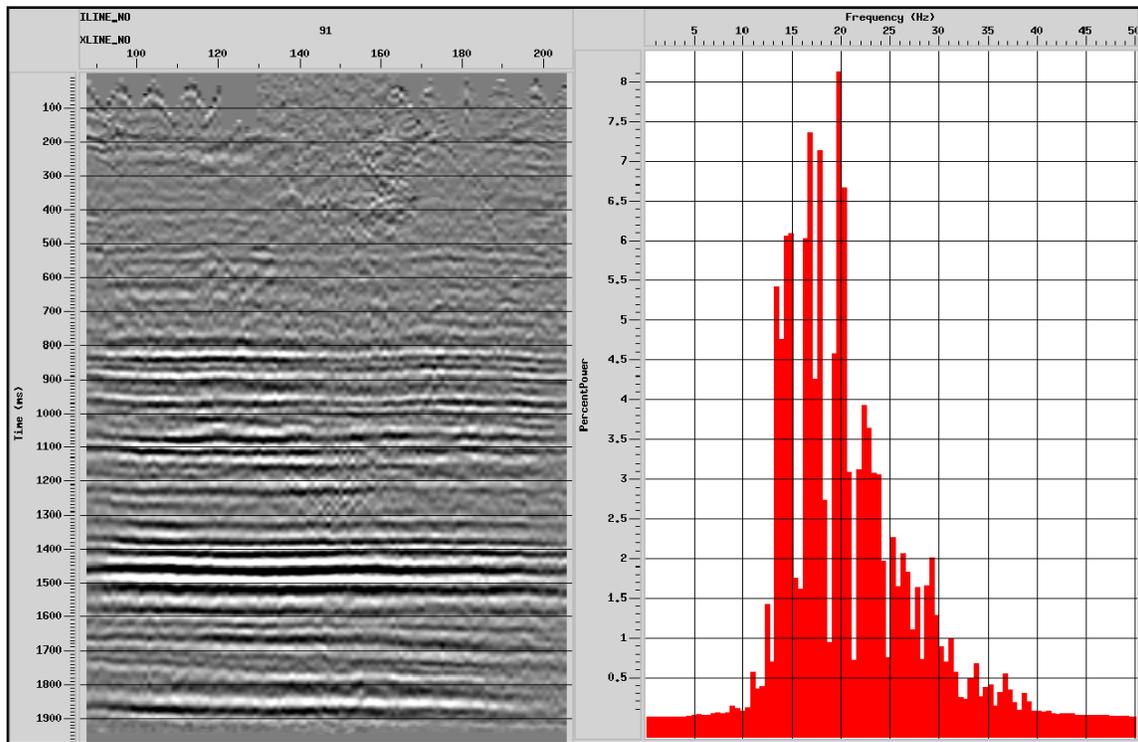
Figure 3.1.6. Stacked seismic section (left) and its frequency spectrum (right). Note that there is no significant seismic energy below 10 Hz.
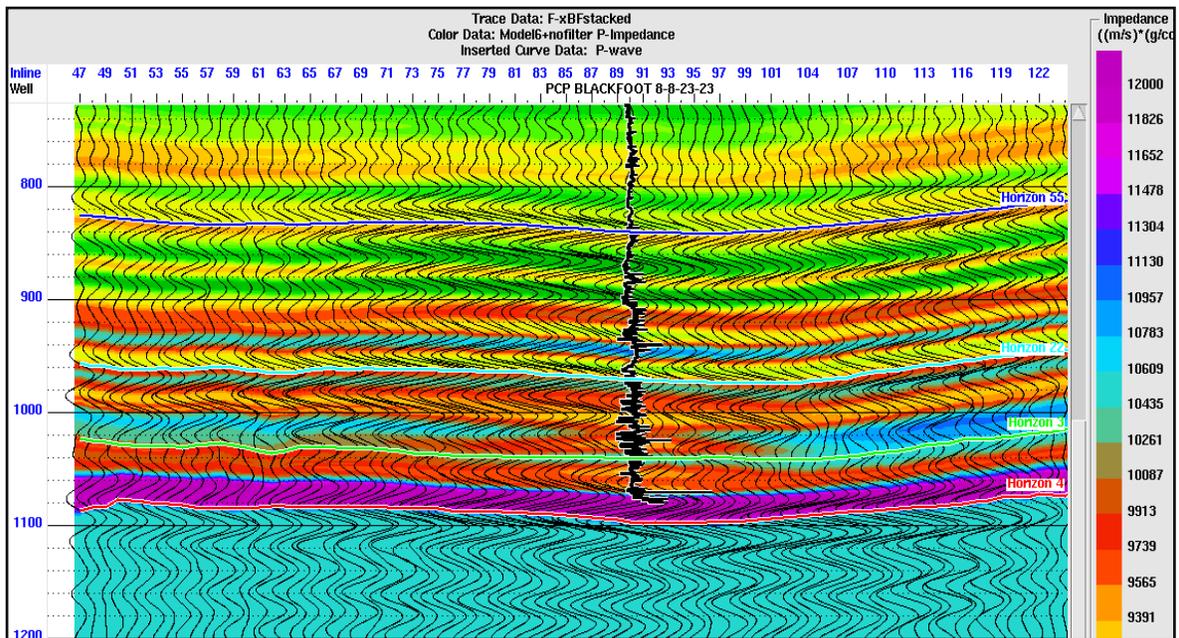
Figure 3.1.7. Cross-section of unfiltered initial model impedance derived from well-log interpolation.
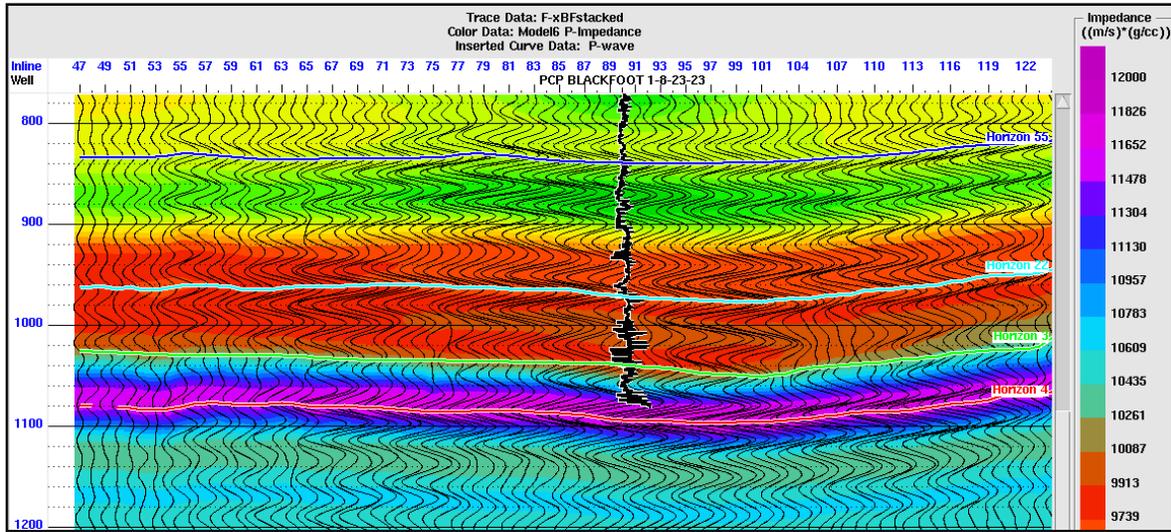
Figure 3.1.8. Cross-section of the initial AI model after low-pass filtering.
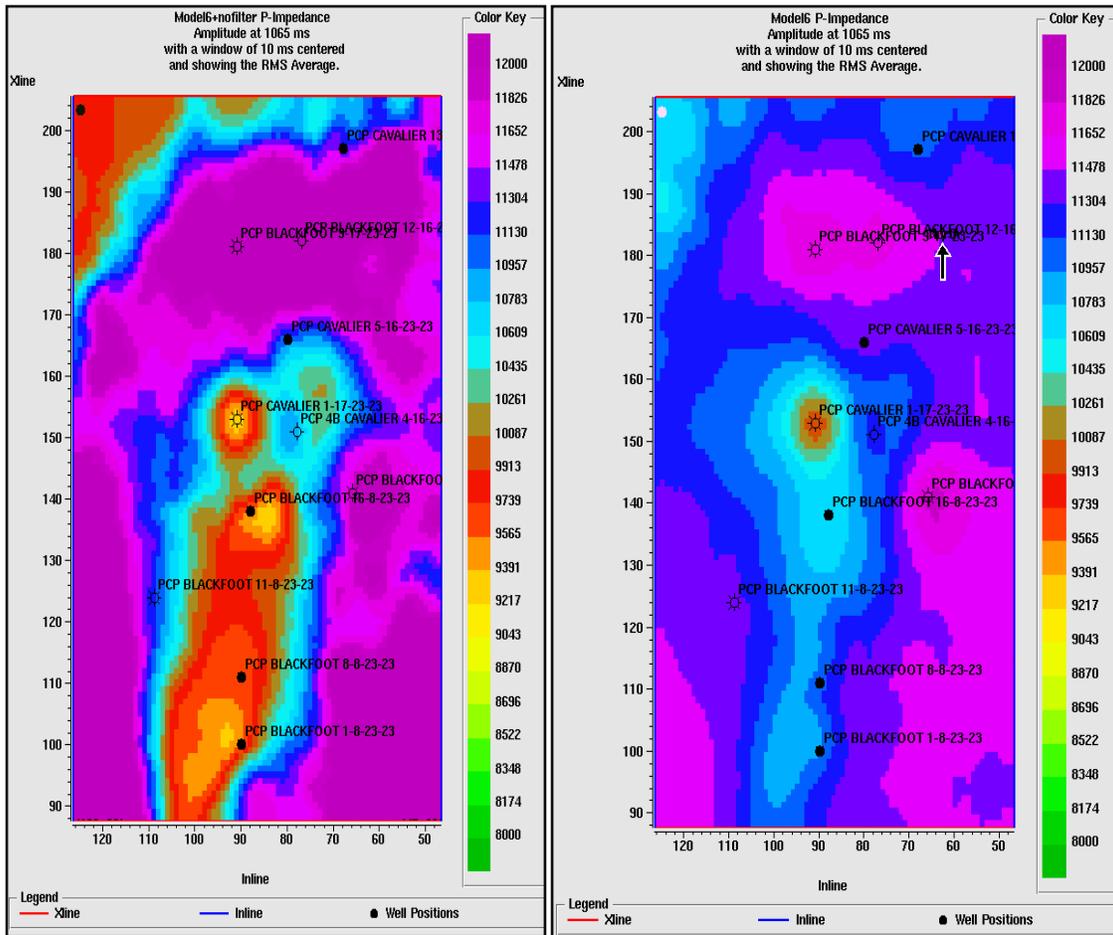
Figure 3.1.9. RMS average impedance of initial model indicated in slice at time 1065 ms, for unfiltered (left) and filtered (right) models.

64

The H-R band-limited AI inverse was the first inversion procedure applied to the dataset. I used the following parameters:

➢ Inversion time: Horizon 55 - 1100 ms;
➢ Number of iterations: 10;
➢ Separate scales;
➢ High cut frequency   10 Hz.

The inversion in the band-limited method should start with known layer impedance (AI), as indicated in equation (2.2.4). This AI was obtained from the model. I used horizon # 55 as such reference impedance level. The "separate scale" selection was used to adjust the amplitude of each seismic trace in order to match the corresponding trace in the model. As a result of such normalization, the output seismic impedance amplitudes corresponded to those above the 10-Hz frequency threshold in the well-log data. Note that this scaling scheme is further refined to space- and frequency-dependent scaling in SILC procedure (eq. 2.2.8).

Figure 3.1.10 shows the band-limited inversion result compared to the original log at well 1-17. For an easy comparison, log impedance was filtered to match the seismic band using a high-cut filter for frequencies above 60-Hz. The inverted impedance is comparable to the impedance from the log in the time between 920 ms to 1100 ms. Above 920 ms, the inverted impedance is quite different from the log impedance. In this example, the well ended at the time level of ~1100 ms, and therefore the inversion beneath this time is close to the averaged initial model. The inverted impedance column at the well location was used to create a synthetic trace, which was called the inverted synthetic trace. This inverted synthetic trace was correlated with the seismic data for all wells in the area as shown in Figure 3.1.11, and the errors between the original logs and inverted results were measured. The error in the AI values varied from 500 (m/s)·(g/cc) to 850 (m/s)·(g/cc). A cross-section of the inversion result is shown in Figure 3.1.12. Note the low-impedance zone between times of 1060 ms and 1070 ms. An impedance slice averaged with a 10-ms window centred at 1065 ms time is shown in Figure 3.1.13. Note the low impedance imaged around the wells.
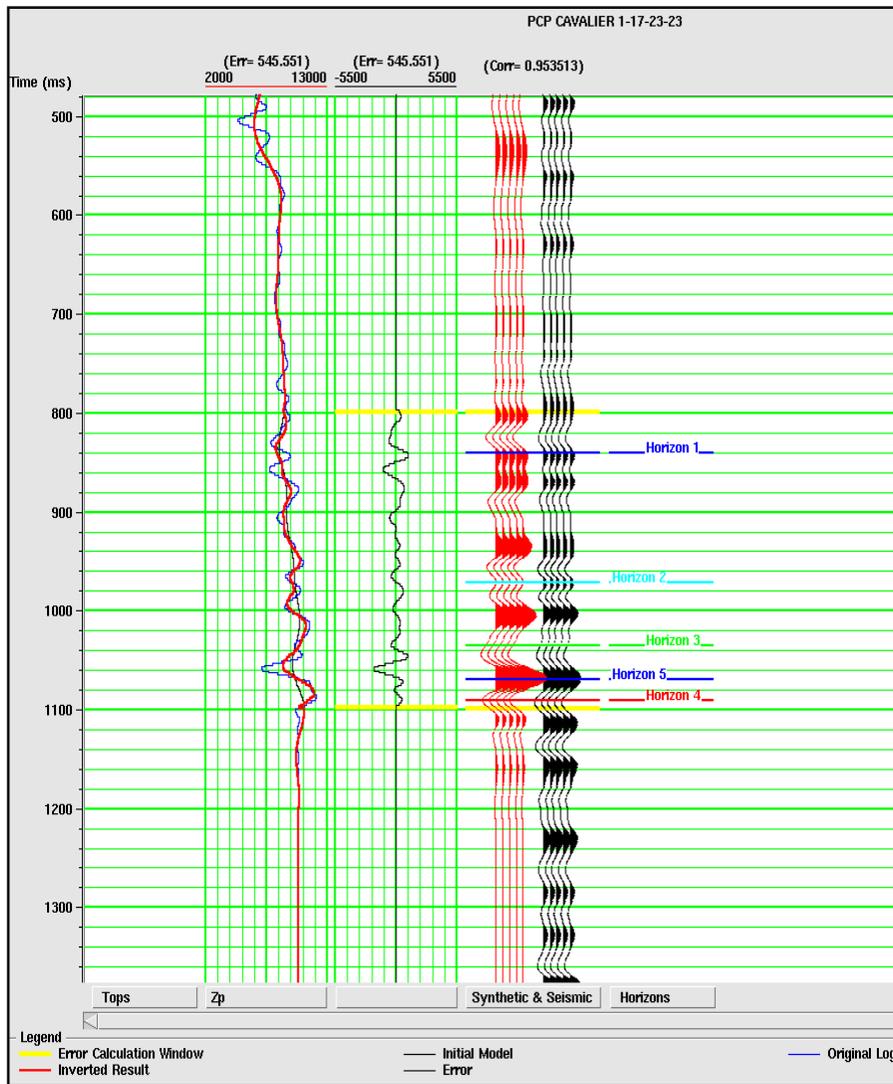
Figure 3.1.10. Inverted result (red) using the band-limited algorithm compared with the well AI log (blue) at the well 1-17. Black curve shows the error between the well-log AI and the synthetic. All data were filtered using a high-cut filter with50-60 Hz ramp. The red wiggle trace was trace generated from the inversion results while the real-data trace is shown in black.

66
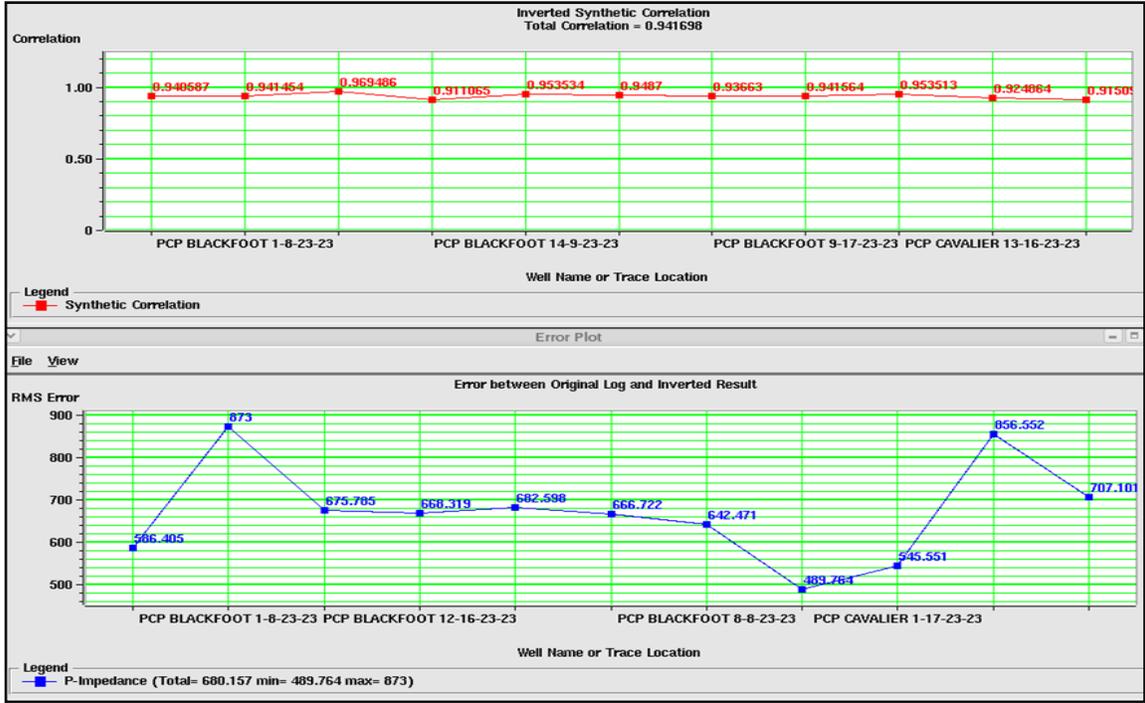
Figure 3.1.11. Inverted synthetic traces correlated with seismic data (top) and the average RMS errors between the original logs and inverted result (bottom).
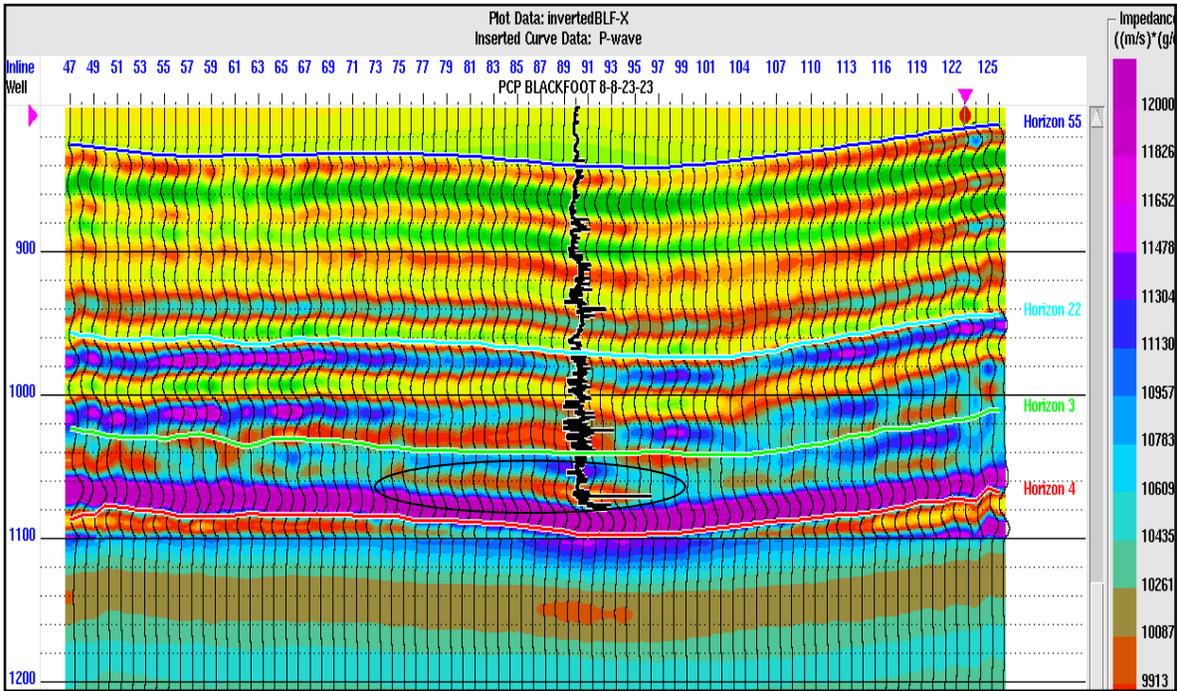
Figure 3.1.12. Cross-section of band-limited inversion results. Note the low impedance around 1065 ms (ellipse).
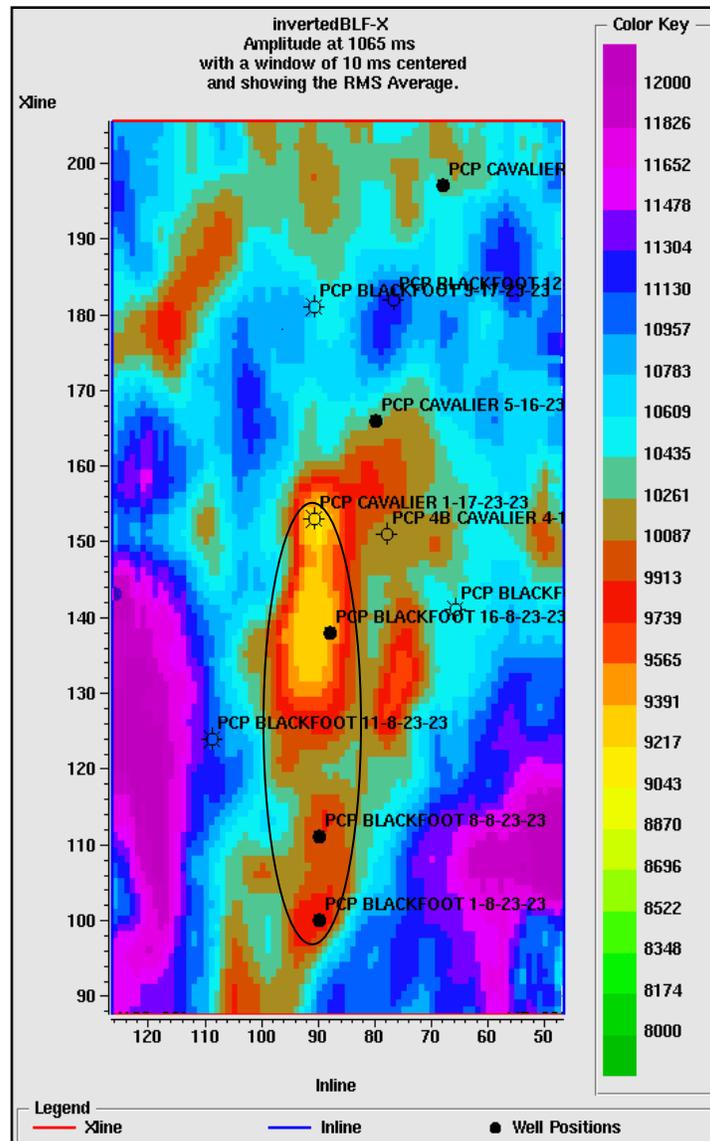
Figure 3.1.113. Time slice of the RMS average impedance result at 1065 ms from the band-limited inversion. Note the channel with low impedance (ellipse).

The next algorithm I applied to the seismic data by using the H-R STRATA program was the model-based inversion. Its parameters were:

➢ Inversion time interval: 800-1100 ms;
➢ Number of iterations: 10;
➢ Separate scales;
➢ Impedance change constraint: ±30%;
➢ High cut frequency: 10Hz.

In this method, the iterations were used to enhance the match between the real and synthetic seismic traces. The impedance change constraints were used to restrict the changes of inversion impedance relative to the average impedance of the model, which was represented by filtered well impedances.

The inversion result at the well location was compared to the original log at well 4-16 as shown in Figure 3.1.14. In general, the inverted AI was comparable to the filtered well-log impedance. Synthetic traces generated from the resulting AI were correlated with the seismic traces for all wells shown in Figure 3.1.15, and the differences between the original filtered log and inverted result were measured. The match between the synthetic traces and the data showed good correlations for most wells. The residual errors in AI varied from 650 (m/s)·(g/cc) to 1100 (m/s)·(g/cc). A cross section of the inversion result is given in Figure 3.1.16. Note that low impedances near 1065-ms level are clearly visible in this Figure. The RMS average impedance at the time 1065 ms, measured within a 10 ms time window, also showed low impedances near most wells within the channel.
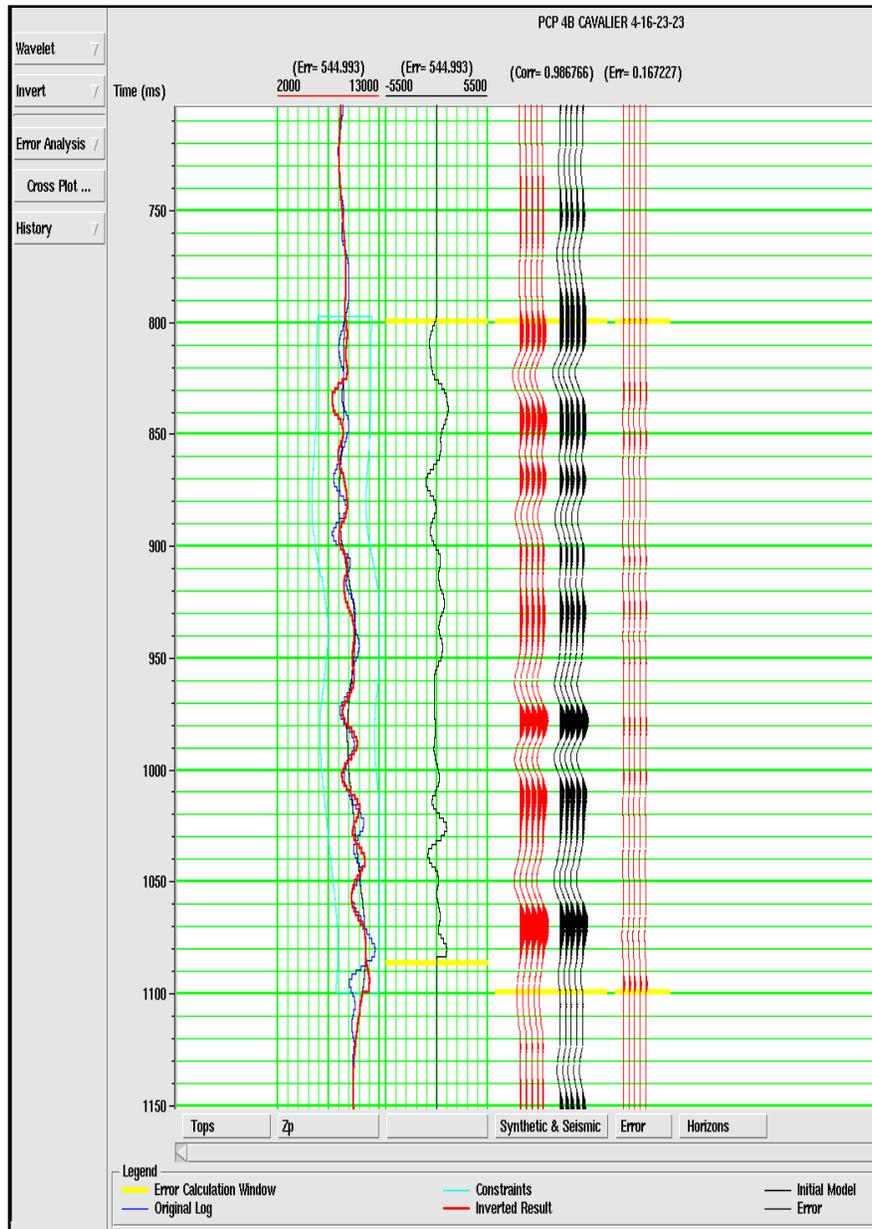
Figure 3.1.14. Inverted result using H-R model-based algorithm compared to the original log at well 4-16. Curve explanations are given in Figure 3.1.10.
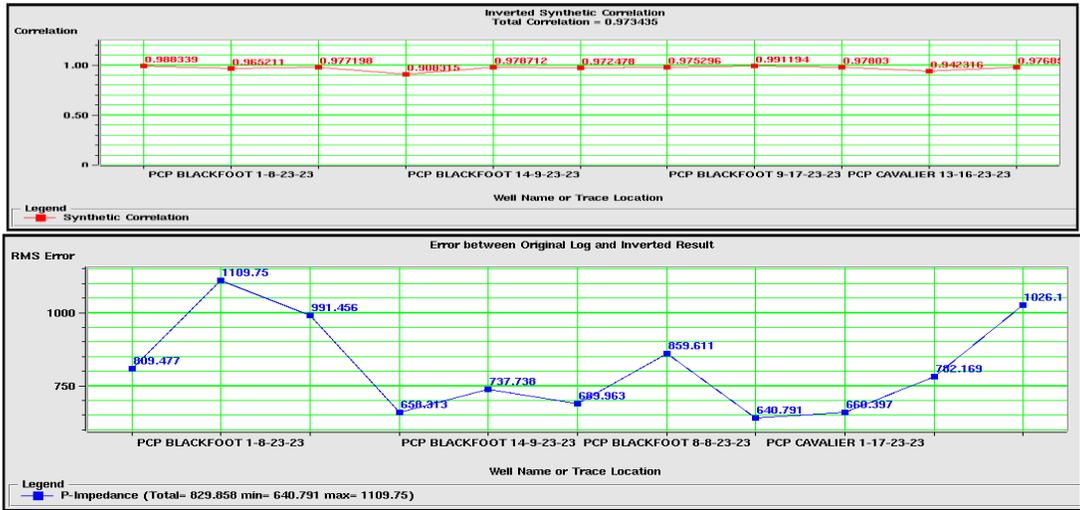
Figure 3.1.15. Top: Correlation of the inverted synthetic and real seismic traces. Bottom: RMS errors between the original logs and inverted results for all wells.
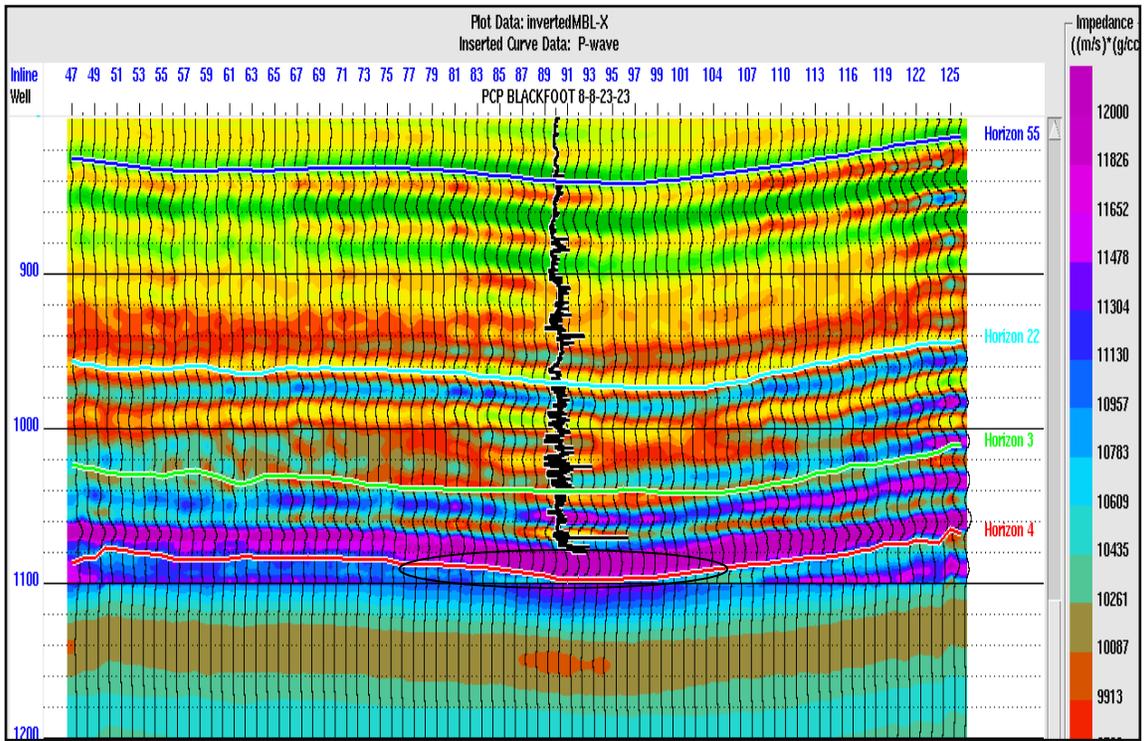
Figure 3.1.16. Cross-section of model based-inversion results. Note the low impedances around 1065 ms (ellipse).
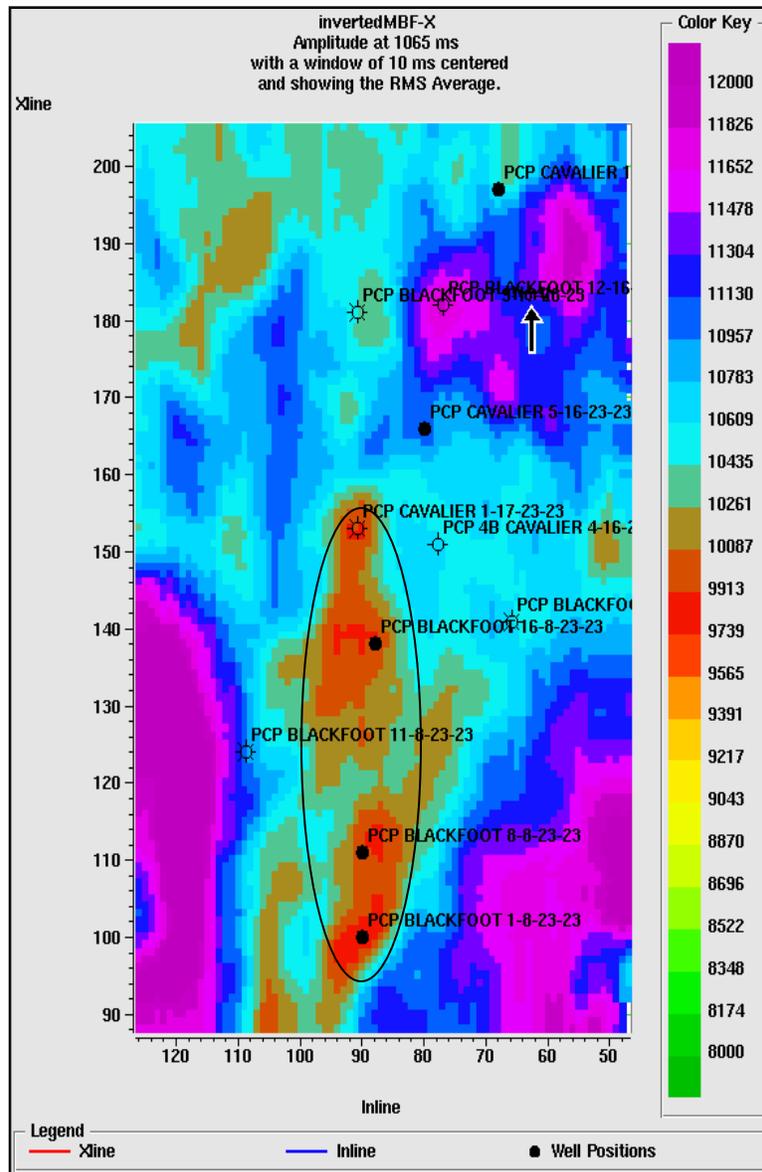
Figure 3.1.17. Slice at time 1065 ms from the model-based inversion in the study area. Ellipse shows low impedance in the channel.

Coloured inversion was the third technique applied to the seismic and well-log data. In this technique, I started with deriving the operator to transform the reflectivity into impedances. In general, the operator spectrum is calculated from seismic and well log data as described in Chapter 2. Figure 3.1.18 illustrates the parameters derived for this operator in H-R STRATA software. The length of the operator, which was later used for convolving with the seismic data, was 200 ms. Other parameters of this inversion method were:

- ➢ High cut frequency: 10Hz
- ➢ Separate scales.

The predicted synthetic at well 1-17 was comparable with the well log (Figure 3.1.19). The synthetic correlation and errors are shown in Figure 3.1 20. The synthetic correlation was poorer compared to the other techniques, and the AI errors (log data misfits) varied from 650(m/s)·(g/cc) to 1000(m/s)·(g/cc). One of the resulting cross-sections is shown in Figure 3.1.21. The low impedance around 1065 ms in the channel is visible, similarly to the results from other AI inversion techniques. As for other inversions, the RMS average impedance of the area at time 1065 ms was taken (Figure 3.1.22), showing the horizontal distribution of the coloured AI.
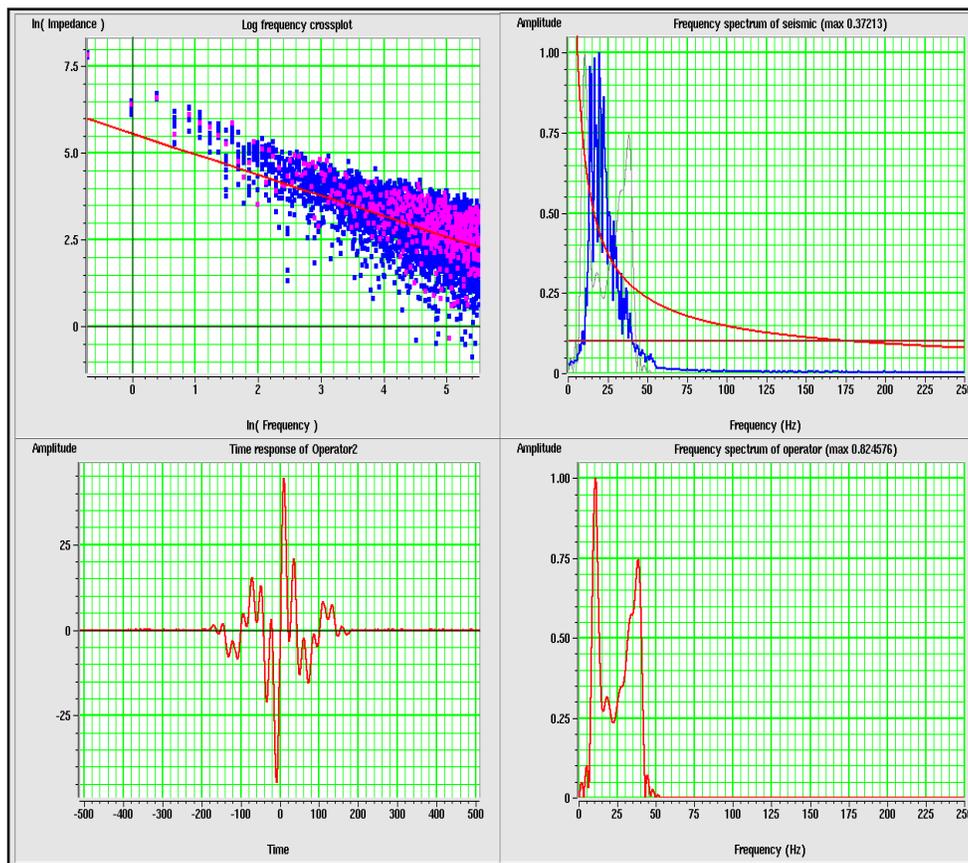
Figure 3.1.18. Operator used in coloured inversion in the time (left) and frequency (right) domains.

73
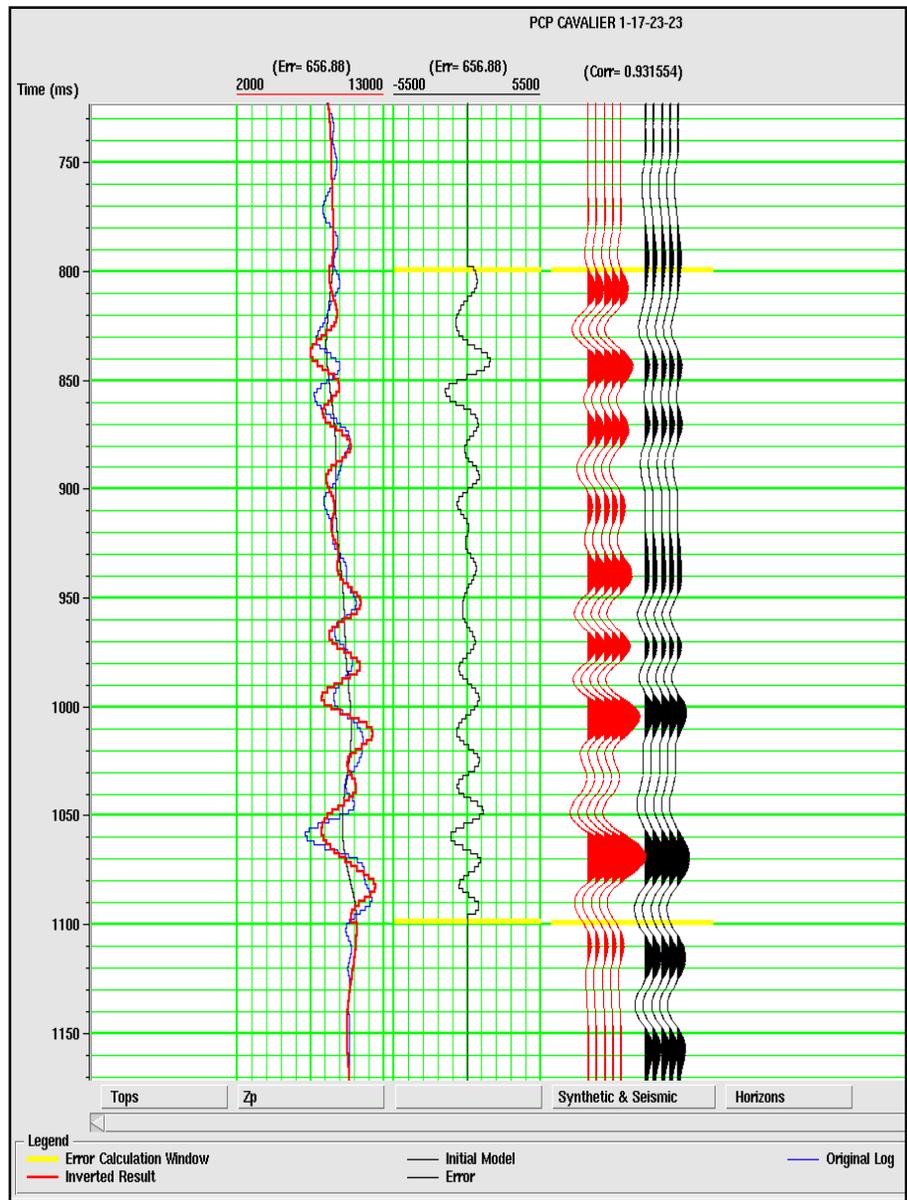
Figure 3.1.19. Inverted result using coloured AI inversion algorithm compared with the original log at well 1-17. Curves explanations are in figure 3.1.10.
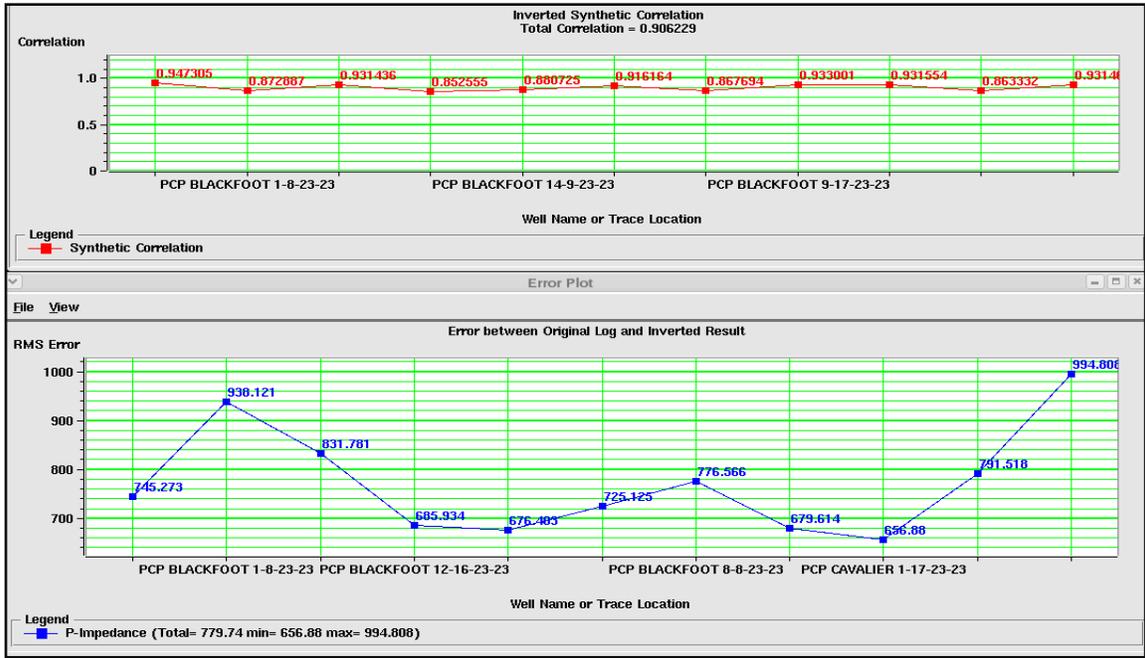
Figure 3.1.20. Inverted synthetic correlation and errors between the original logs and inverted results from all wells.
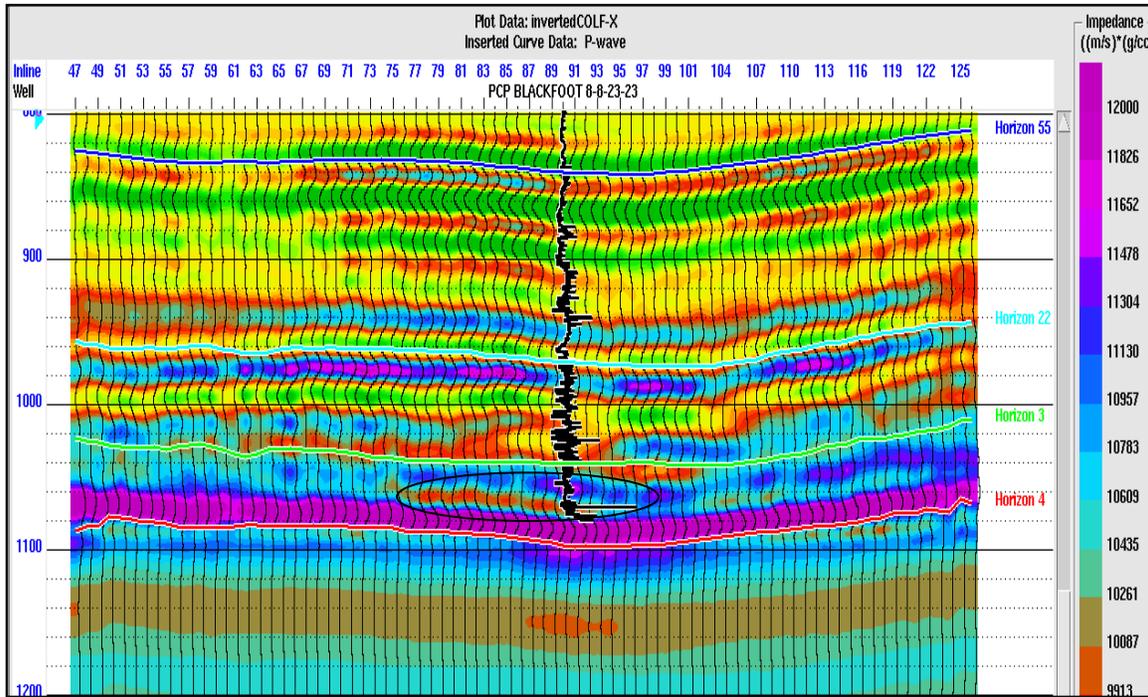
Figure 3.1.21. Cross-section of the coloured inversion result. Note the low impedances around 1065 ms.
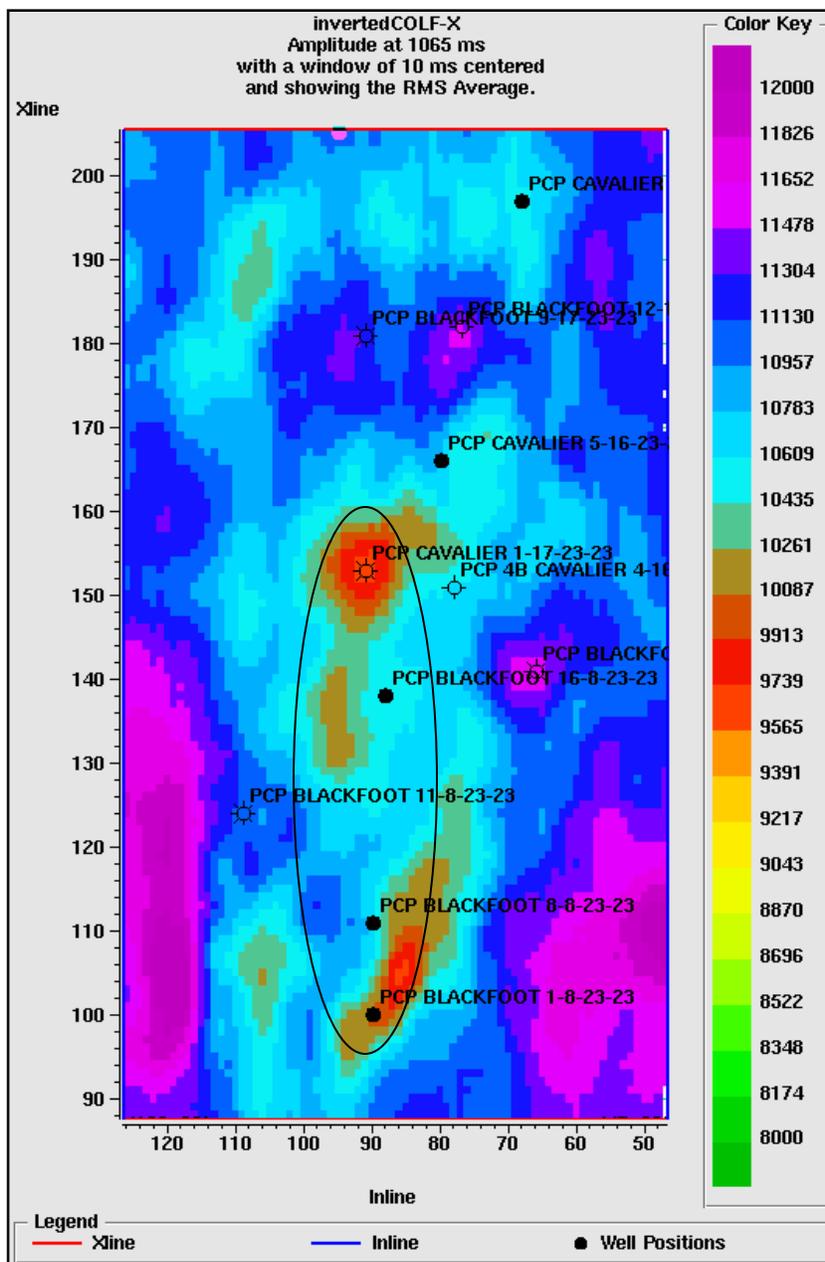
Figure 3.1.22. Slice at time 1065 ms across the coloured-AI result for the study area. Ellipse indicates the low-AI zone of interest.

The fourth method applied to the dataset was Seismic Inversion of well Log Calibration (SILC), implemented in seismic processing system IGeoS (http://seisweb.usask.ca/igeos). The seismic data, horizons and well log data (AI) were exported from the H-R software to IGeoS by using the SEGY format. The seismic data and

well log data were previously correlated, and therefore I only needed to apply the final SILC inversion in IGeoS system. SILC inversion starts with the band-limited impedances, which are constructed from the seismic data by using the iterative equation (2.2.4), and the impedances of wells, which were presented in the form of AI logs. Next, a series of over-lapping zero-phase filters extending slightly beyond the seismic band were defined in the frequency domain. Within each filter frequency band, the seismic impedances were balanced to match those of the wells, by using equation (2.2.8). The resulting parameters of the algorithm were:

- Seismic frequency band: 10 Hz to 60 Hz;
- Well-log band: 0 Hz to 60 Hz;
- Width of each band-pass filter 10 Hz;
- Length of the sliding amplitude-balancing time window 80 ms.
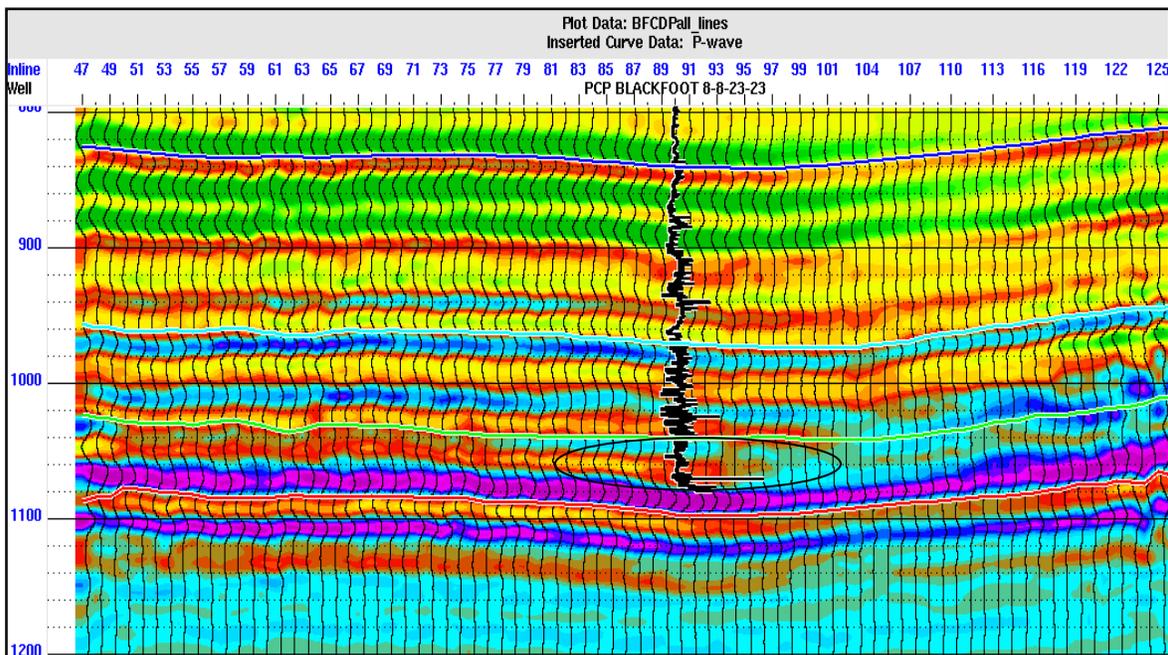
Figure 3.1.23. Cross-section of the SILC inversion result.

77
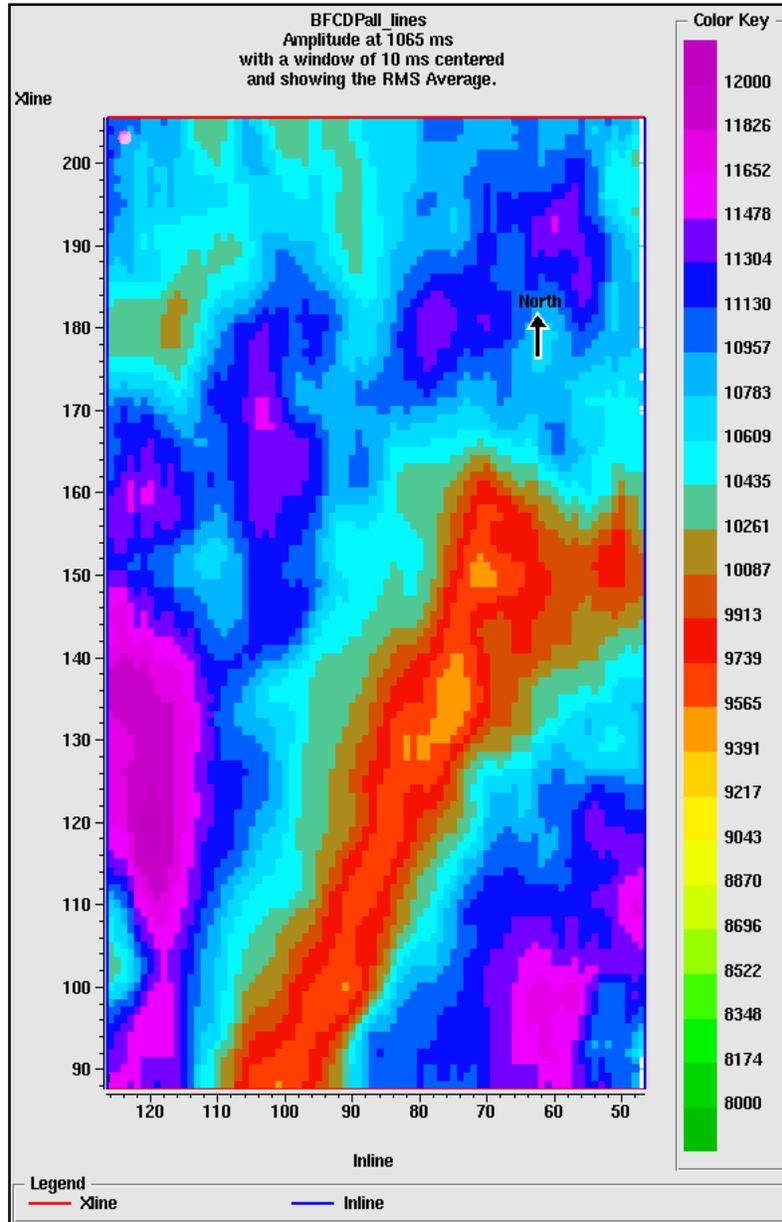
Figure 3.1.24. Slice of the RMS average impedance of the SILC AI at time 1065 ms.

Now let us compare the inversion results by different methods shown in Figures 3.1.12, 3.1.16, 3.1.21 and 3.1.23. These images represent cross-sections of the 3D image volume across the channel. The band-limited and model-based acoustic impedance results show similar low-impedance zones at the reservoir depth, indicated by ellipses in Figures 3.1.12 and 3.1.16). The slices of the AI distributions are also similar in the band-limited and model-based inversions (Figure 3.1.13 and Figure 3.1 17). However, the coloured AI

78

result shows the low-impedance zone less clearly than the first two methods. The same difference can also be noticed in the slice impedance distribution (Figure 3.1.22). It appears that poorer performance of the coloured inverse may be caused by the need to derive a single operator (Figure 3.1.21) that resulted in weaker correlations with the stacked data at the positions of the individual wells.

Notably, SILC impedance result shows the low-impedance zone near the channel quite differently. At the reservoir depth, the low-impedance zone shows lower AI values and higher spatial resolution than in the H-R based inversions. The higher resolution is likely related to using the complete information from the seismic data scaled to the complete well-log spectra at well locations (Figure 3.1.23). In principle, because of the simplicity of the SILC procedure and its orientation on fullest utilization of the data with minimal algorithmic constraints (Morozov and Ma, in press) its images most closely represent the information contained in the data. Additionally, SILC time slices also show significantly different spatial impedance distributions (Figure 3.1.24). This difference could be caused by the strongly different spatial interpolation technique (SILC uses the Delaunay triangulations between wells). At the same time, note that the spatial AI distribution inverted by SILC is similar to the reflectivity pattern (Figure 1.5.8), from which the H-R inversins differ significantly. In respect to the spatial interpolation, with typically relatively wide well spacing, there probably is no "silver bullet" interpolation method, and it is important to try different approaches. By comparing the results from different interpolation schemes, one can assess the differences in predictions caused by the different assumptions.

3.2 Inversion for Elastic Impedance

To perform the EI inversion, we need to produce range-limited stacks of the CMP gathers at different constant angles. At the first step, I converted the CMP gathers from the offset to angle form and to identify the maximum incidence angles in our data. Then, according to these maximum angles of the CMP gathers, I stacked the CMP angle-gathers data. In our Blackfoot dataset, the maximum angle was 29°, as shown in Figure 3.2. 1. Ac-

cordingly, I stacked the data within two angular ranges: near angles from 0° to 15° and far angles from 16° to 30° (Figure 3.2.2).
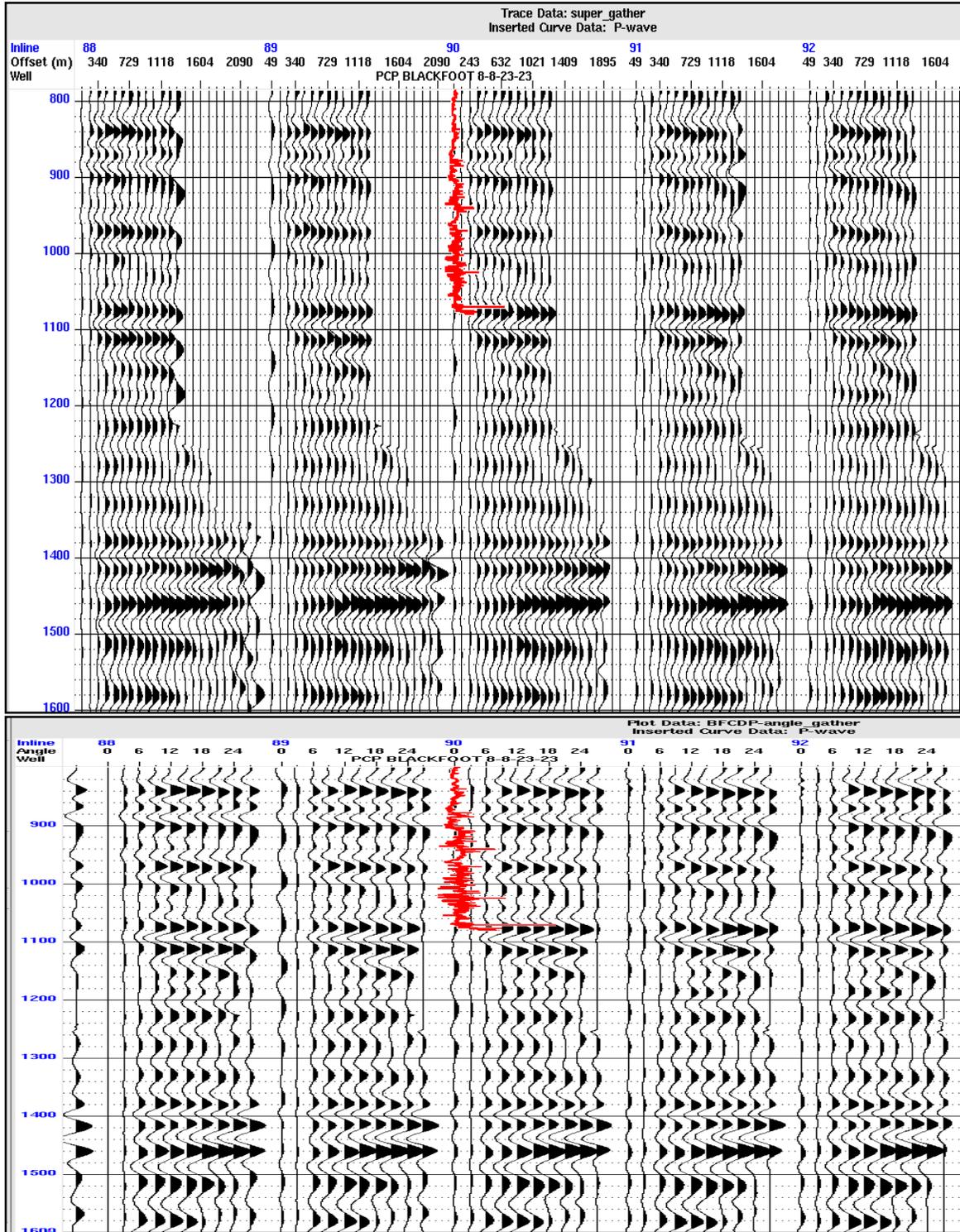
Figure 3.2.1. CMP gathers shown as offset gathers (top) and angle gathers (bottom).

80
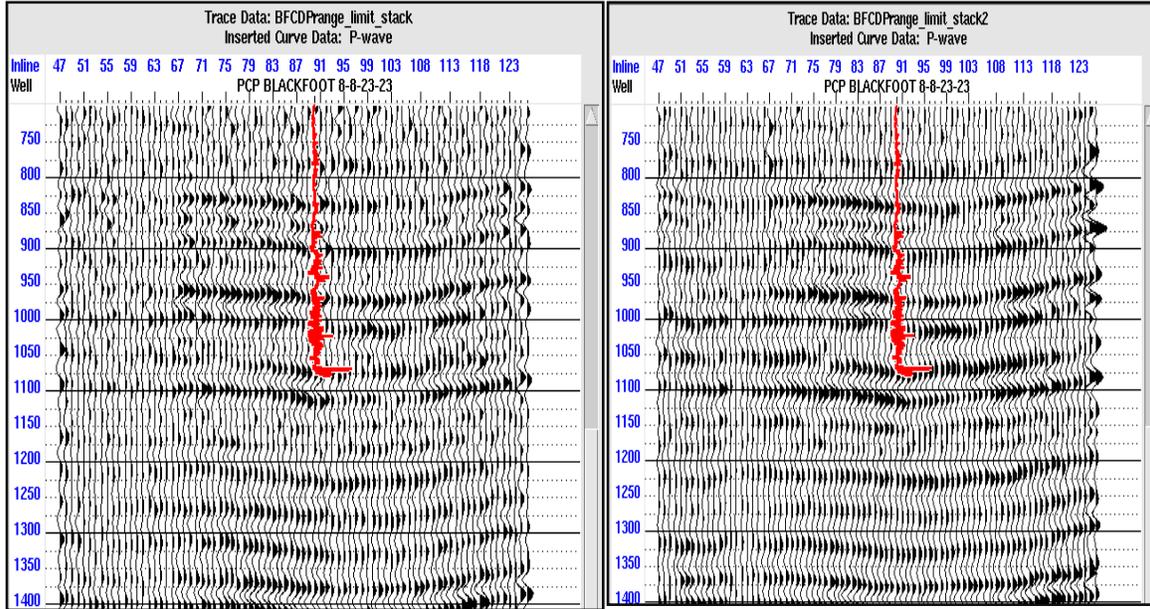
Figure 3.2.2. Two seismic cross-sections stacked at near angles (left) and far angles (right). p-wave log from well # 8-8 is shown in red.

Once we had our data stacked within the two angle ranges, we proceeded to the next step, which consisted in creating the near- and far-angle EI logs at the wells. The EI logs are required to build the two respective initial models for inversion. Equation 2.3 4 was used to construct the EI logs for both the near-angle and far-angle stacked datasets. The parameters used to generate the elastic impedance were:

- ➢ V_P, P-wave log;
- ➢ V_S, S-wave log;
- ➢ ρ, density log;
- ➢ $K = \left(\dfrac{V_S}{V_p}\right)^2 = 0.25$;
- ➢ For near angles, $\theta = 8˚$;
- ➢ For far angles, $\theta = 23˚$.

Extracting the wavelet from the near- and far-angle stacks used the following steps which were also essential for building the initial models. The statistical wavelet was extracted as in AI inversion above for the near- and far-angle data (Figure 3.2.3). The parameters of the wavelet extraction algorithm were:

81

➢ Start time: 800 ms;
➢ End time: 1200 ms;
➢ In-line range for auto-correlation: 55 to 115;
➢ Cross-line range: 95 to 195;
➢ Wavelet length: 150 ms;
➢ Taper: 20 ms;
➢ Phase: zero.
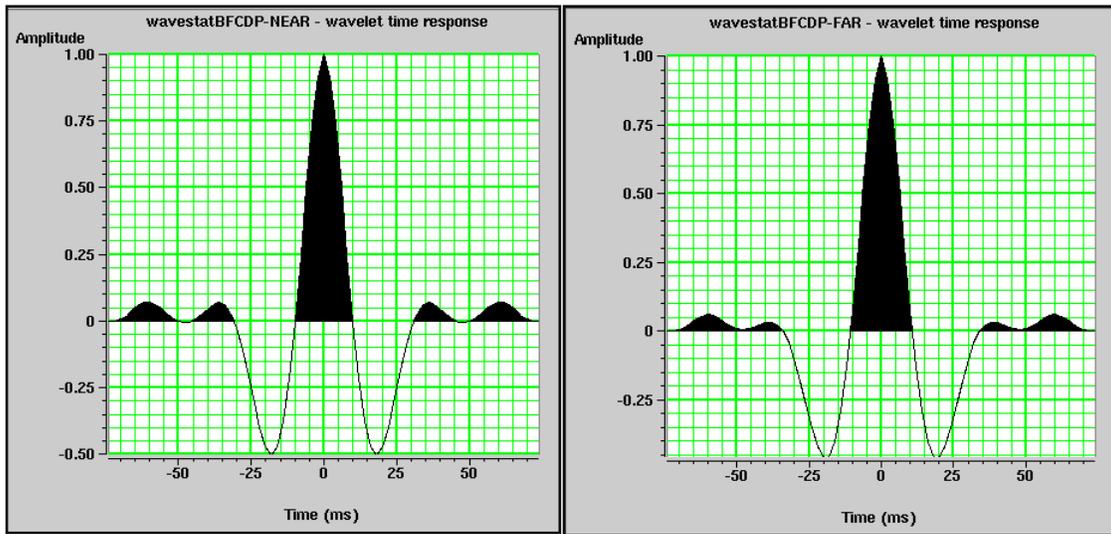
Figure 3.2.2. Statistical wavelets constructed from near angle section stack (left) and far angle section stack (right).

Note that there is only a slight difference between the near-angle and the far-angle wavelets. Such small difference may be caused by the small angular aperture of the dataset.

Constructing the initial models was the next step following the wavelet extraction. In EI inversion, I used the same four horizons picked during the previous post-stack AI inversions. The models (near- and far-angle) were also constructed in the same ways we built the model for post-stack inversion. Instead of using the AI as the property interpolated between the wells, I now used the EI for the near- and far-angle data. A similar low-pass filter (with a 10-Hz cut-off) was applied to the models (Figure 3.2 4).
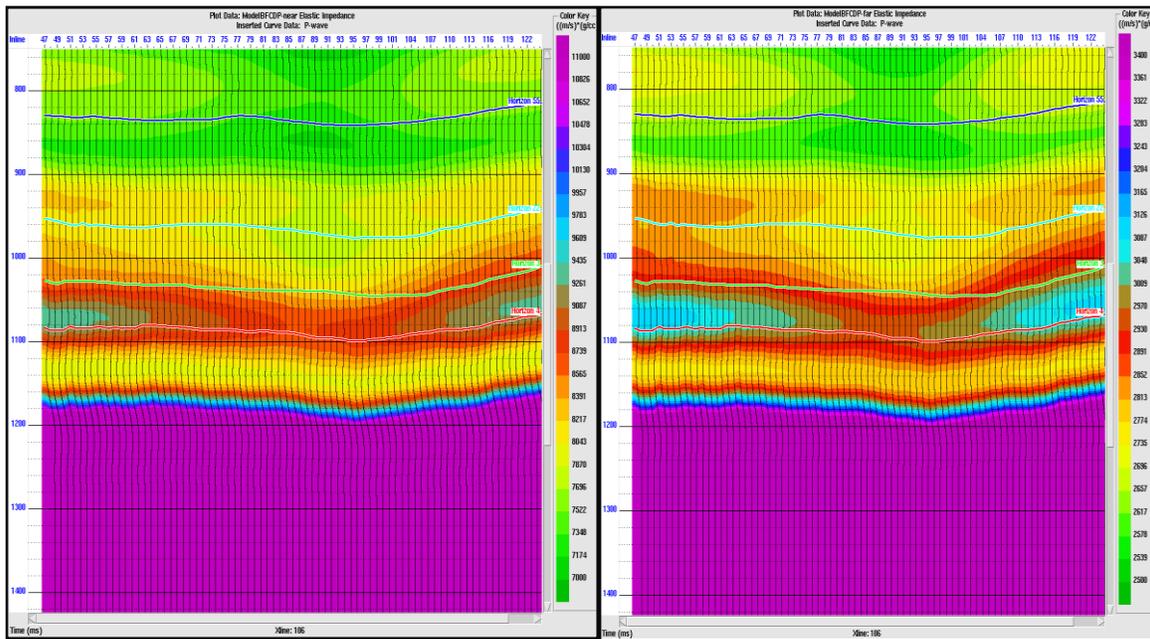
Figure 3.2.3. Initial models constructed from wells and seismic horizons: near-angle (left) and far-angle (right).

Once the wavelets were extracted and initial models built, the EI inversion was applied to the near- and far-angle stacked data separately. Two inversion methods were utilized by using the H-R software: band-limited and model-based. These two techniques were used in the same way as in the post-stack AI inversion above.

I started with the band-limited inversion technique by using parameters similar to those of the post-stack AI inversion:

➢ Inversion time: Horizon 55 - 1100 ms;
➢ Number of iterations: 10;
➢ Separate scales;
➢ High-cut frequency: 10 Hz.

The H-R Quality Control tool helped comparing the EI results to the EI logs computed in the wells. Figure 3.2.5 shows a comparison between the EI inversion result and EI logs from well 1-17 for both near- and far-angle stacks. A 60-Hz high-cut filter was again applied to make the log impedances match the seismic band. This Figure shows that the EI resulting inversion was close to the EI derived from the log. Because most well

83

ended at the time level of ~1100 ms, the model reduces to the average initial model values below this time.

As with AI, correlations were measured between the inverted synthetic traces and the near-CMP seismic data for all wells, and the error (differences) between the original EI logs and inverted results were measured quantitatively (Figures 3.2.6 and 3.2.7). When the inversion result appeared satisfactory in this quality control, I applied the inversion to the whole seismic dataset. A cross-section of the inversion result is shown in Figure 3.2.8. A 10-ms RMS averaged impedance slice at 1065 ms is also shown in Figure 3.2 9.
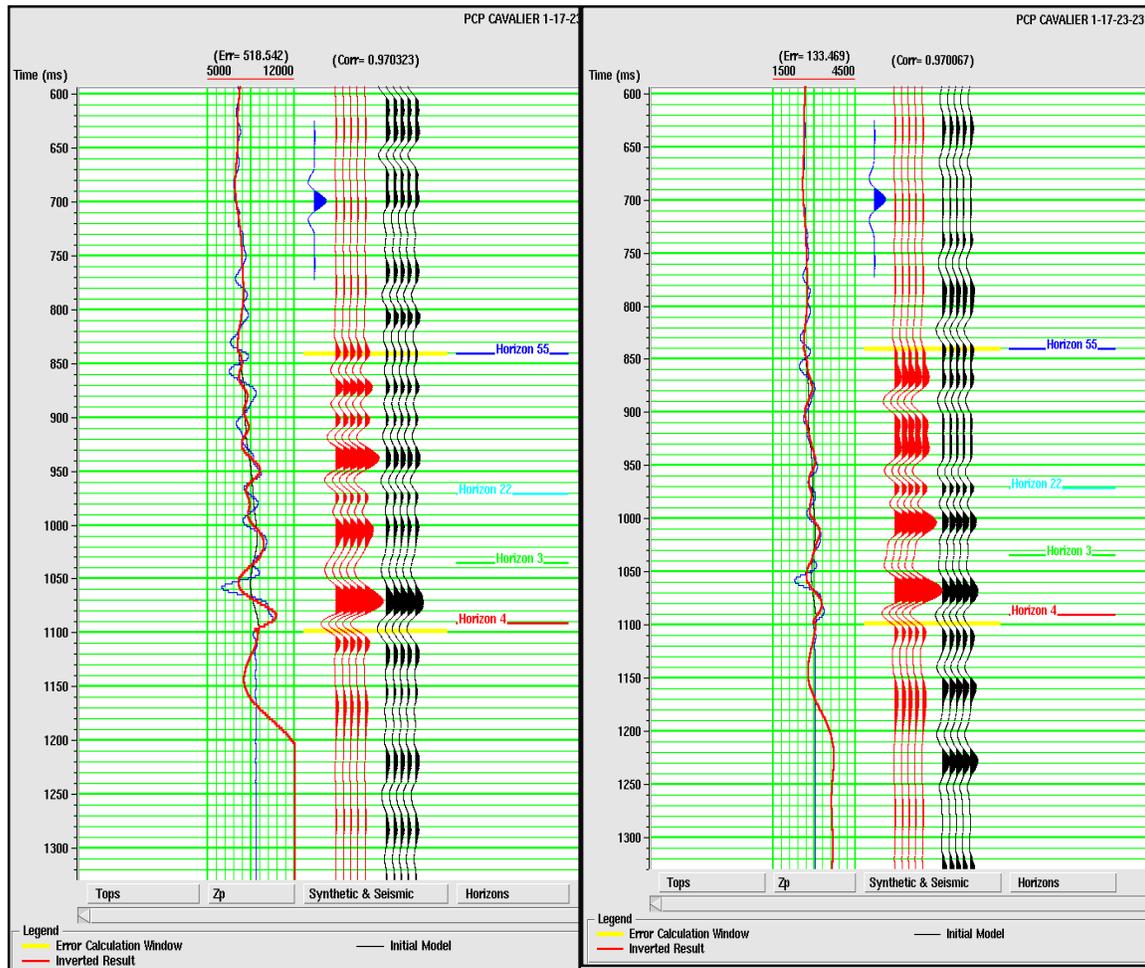
Figure 3.2.4. Quality control at well location to compare the band-limited EI result the well: *left*: near-offset, *right*: far-offset. Curves and notation as in Figure 3.1.10.

84
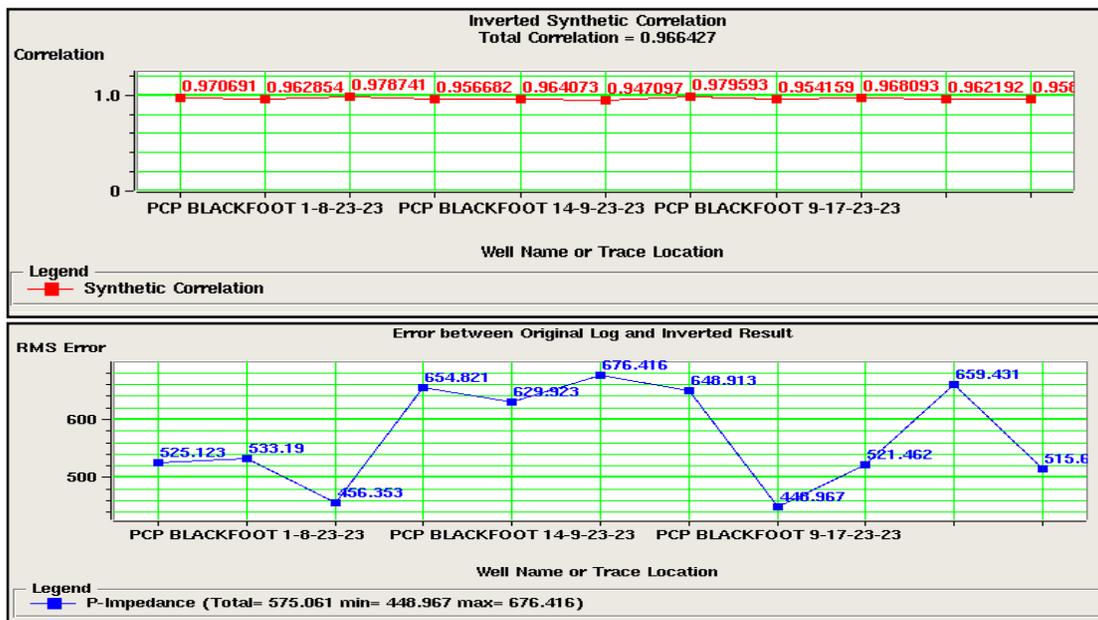
Figure 3.2.5. For the band-limited near-angle inversion: *red*: correlation coefficients of the inversion result to to seismic traces; blue: errors between the original logs and inverted results for all wells (blue).
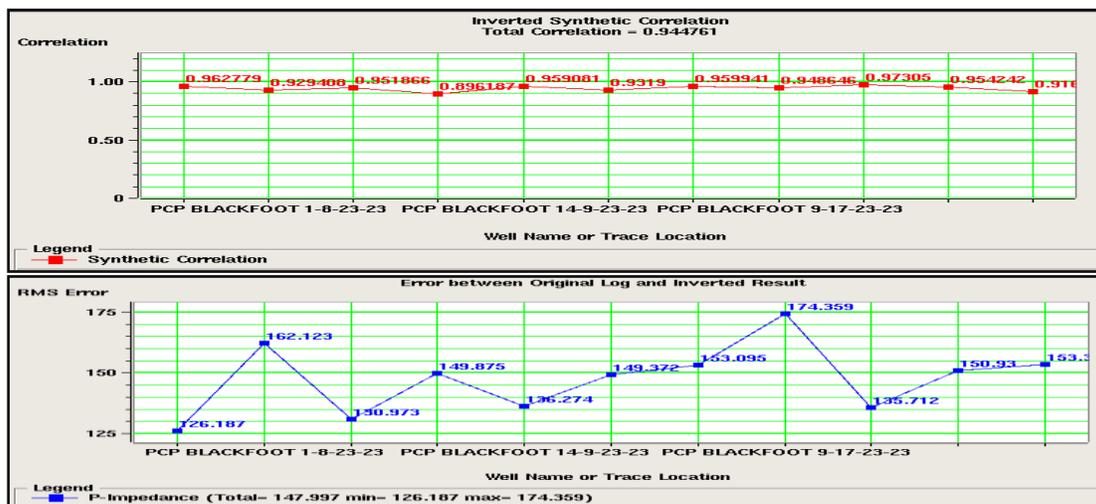
Figure 3.2.6. For the band-limited far-angle inversion: *red*: correlation coefficients of the inversion result to to seismic traces; blue: errors between the original logs and inverted results for all wells (blue).
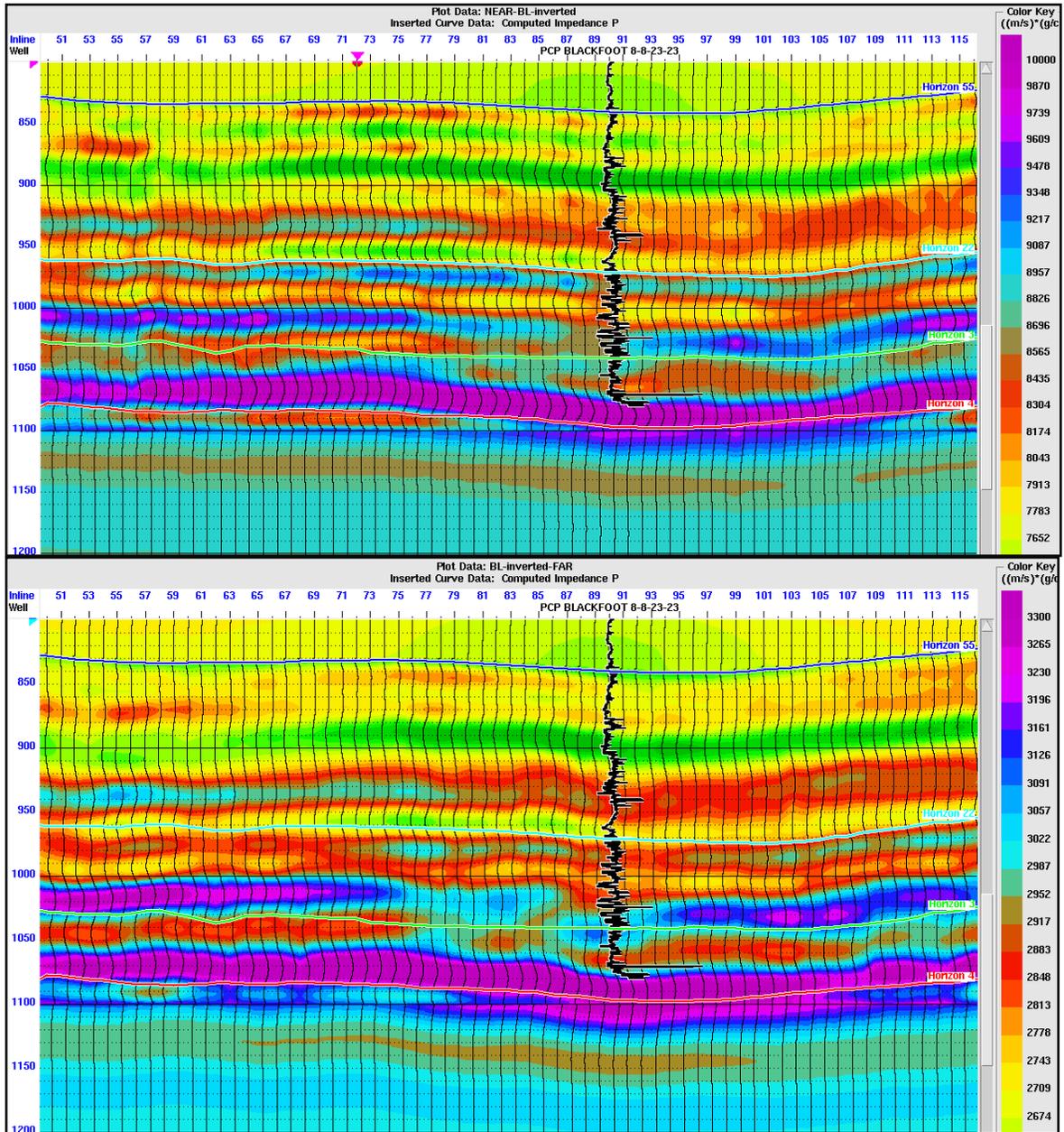
Figure 3.2.7. Two cross-sections of the EI using band limited method: near inversion (top) and far inversion (bottom).
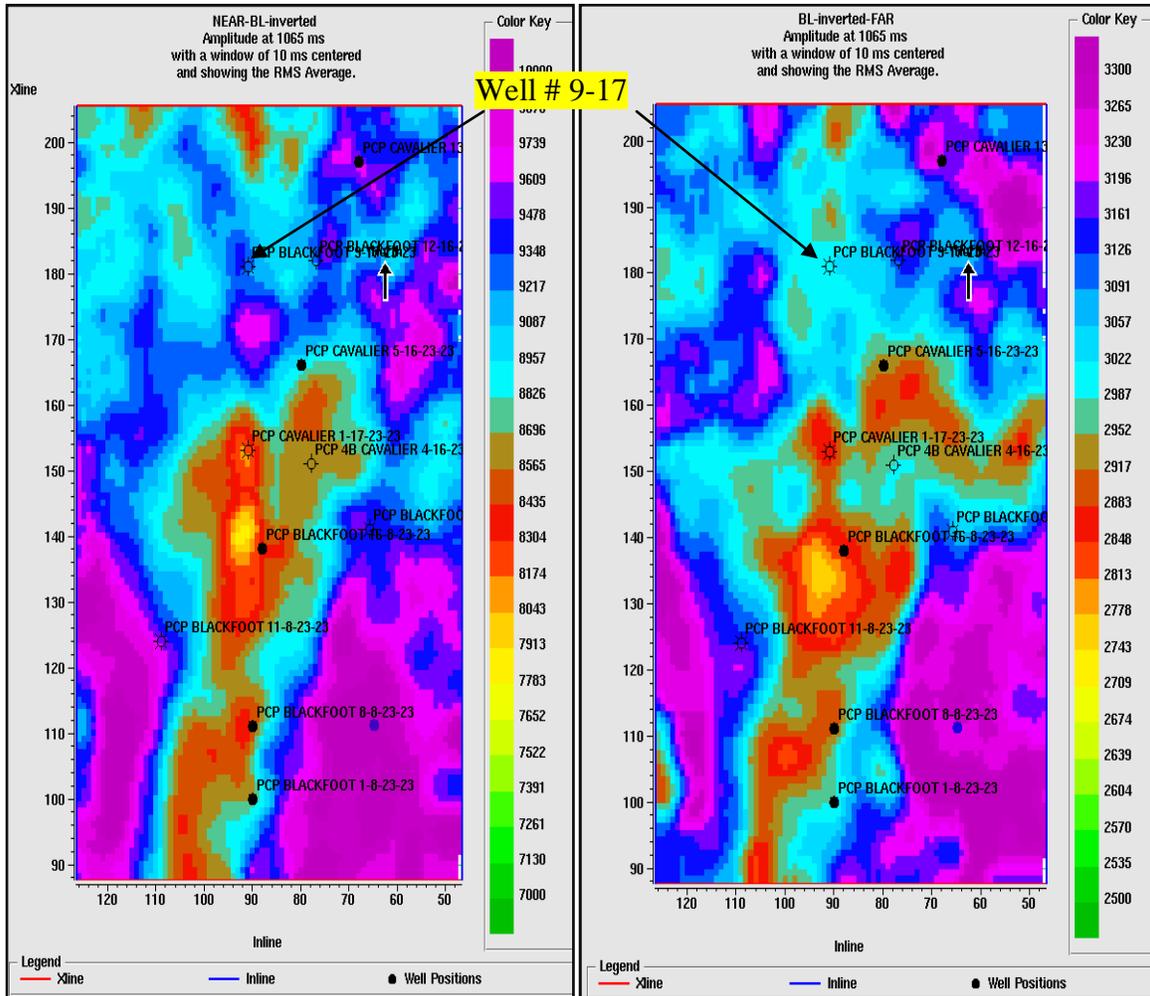
Figure 3.2.8. Slices of EI are taken at time 1065 ms for band-limited method: near-angle (left) and far-angle (right).

In model-based EI inversion; the parameters used were as follows:

➢ Inversion time: 800 - 1100 ms;
➢ Number of iterations: 10;
➢ Separate scales;
➢ Impedance change constraint: ±30%;
➢ High cut frequency: 10Hz.

Similarly to band-limited method, quality control is performed at the wells to check the parameters and compare the inversion results to well-log impedances. The comparison be-

tween inverted and log impedance at well 1-17 for near- and far-angle stacks are shown in Figure 3.2 10. Figures 3.2 11 and 3.2 12 indicate the correlations between the inverted synthetic trace and seismic data at the wells, as well as the errors between the original logs and inverted results. When I obtained a satisfactory match between inversion impedance and well impedance at the wells, I applied the inversion to the entire seismic dataset. A cross-section of the inversion result is shown in Figure 3.2 13. A slice of EI at 1065 ms averaged within a 10-ms window is shown in Figure 3.2 14.
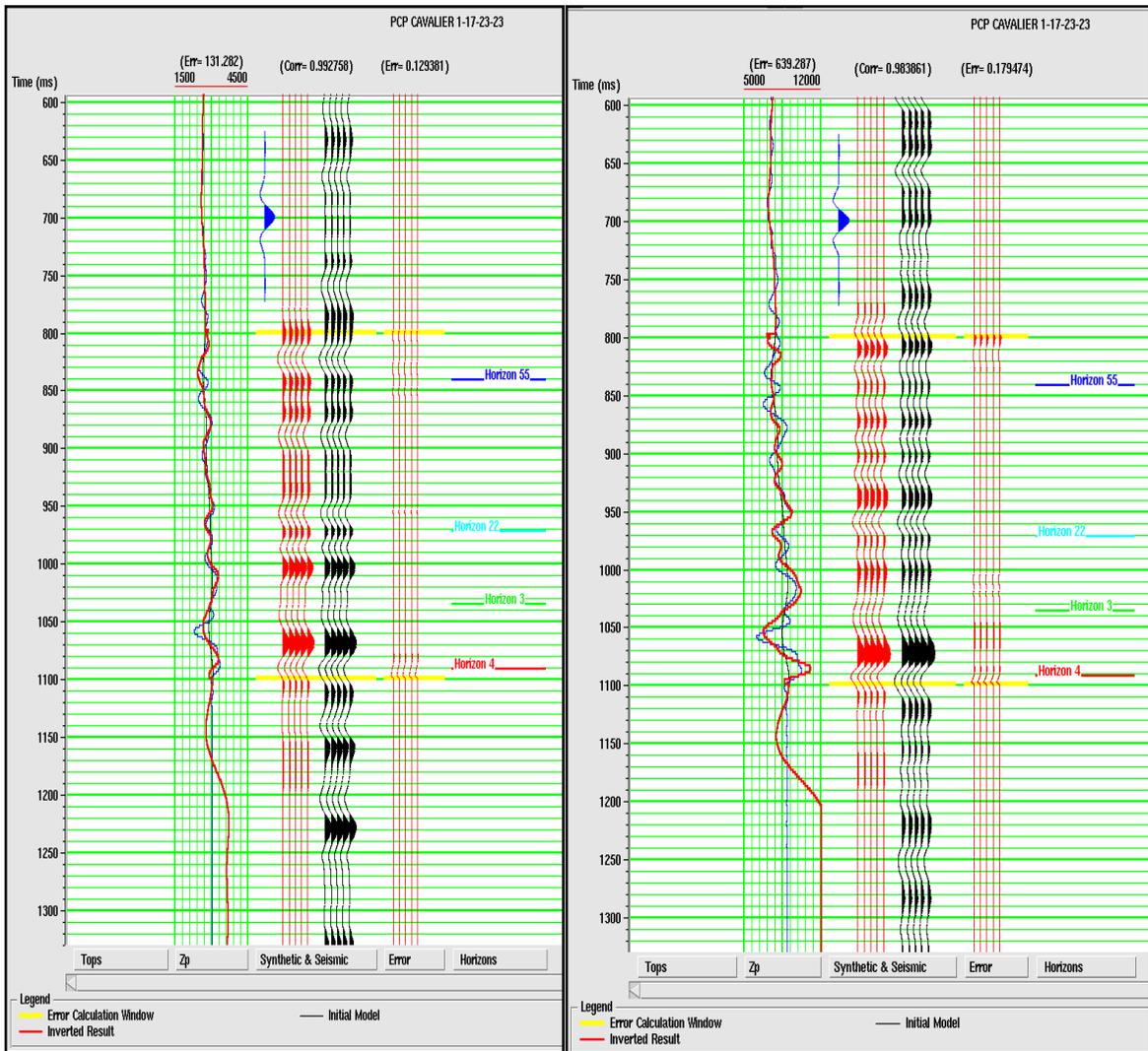
Figure 3.2.9. Quality control applied at well location to compare elastic impedance result to elastic at the well using model-based method, near elastic impedance (left) and far elastic impedance (right).
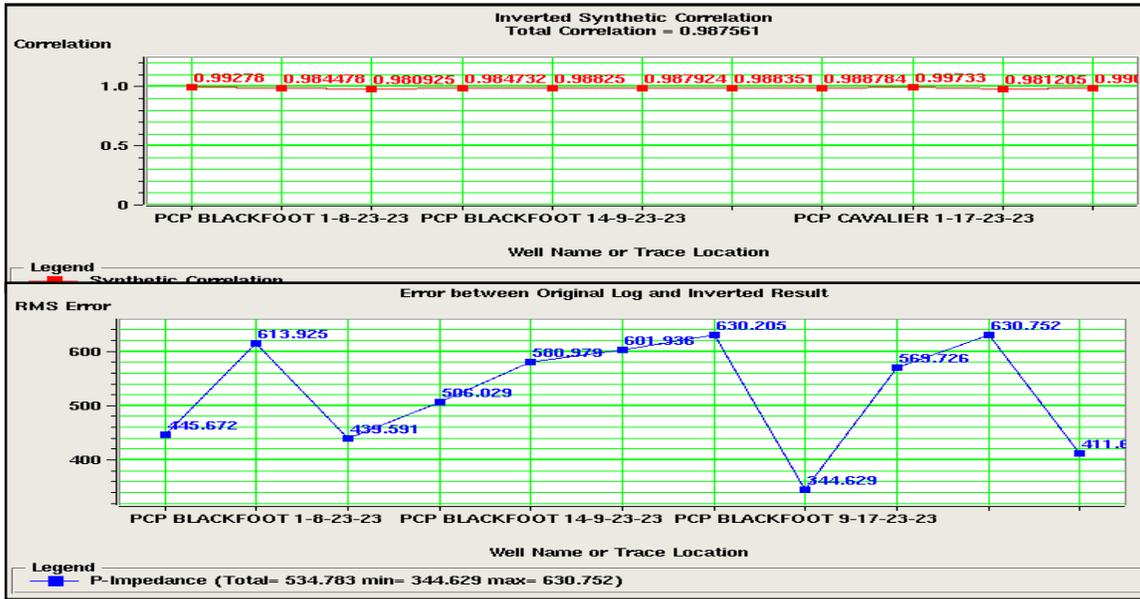
Figure 3.2.10. Quality control of the near-angle, model-based EI inversion: *Top*: **correlation of the predicted and real seismic reflectivity; Bottom: RMS errors between the well--log and inverted EI.**
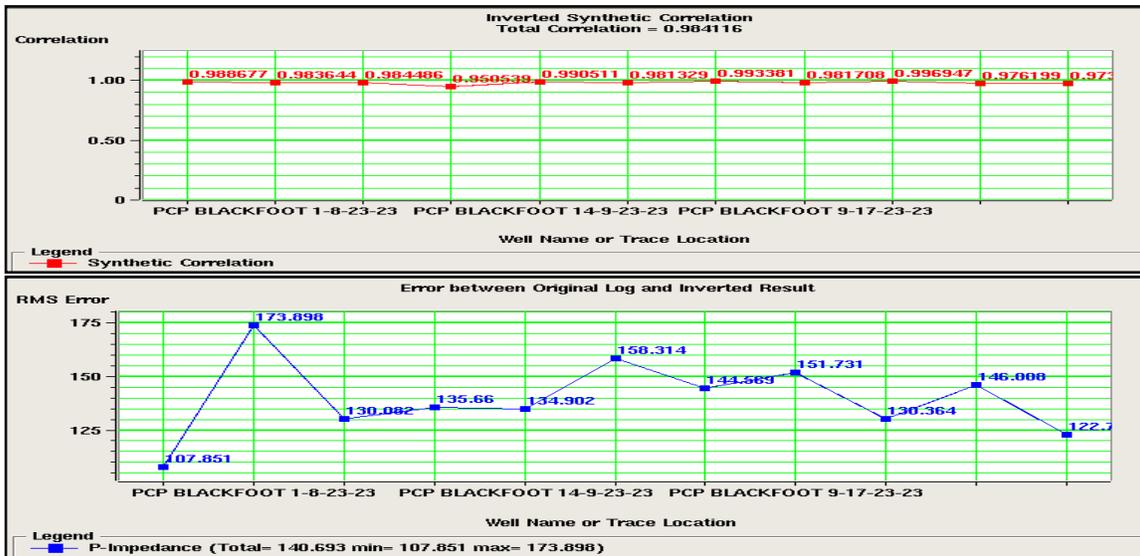
Figure 3.2.11. Quality control of the far-angle, model-based EI inversion: *Top*: **correlation of the predicted and real seismic reflectivity; Bottom: RMS errors between the well--log and inverted EI.**
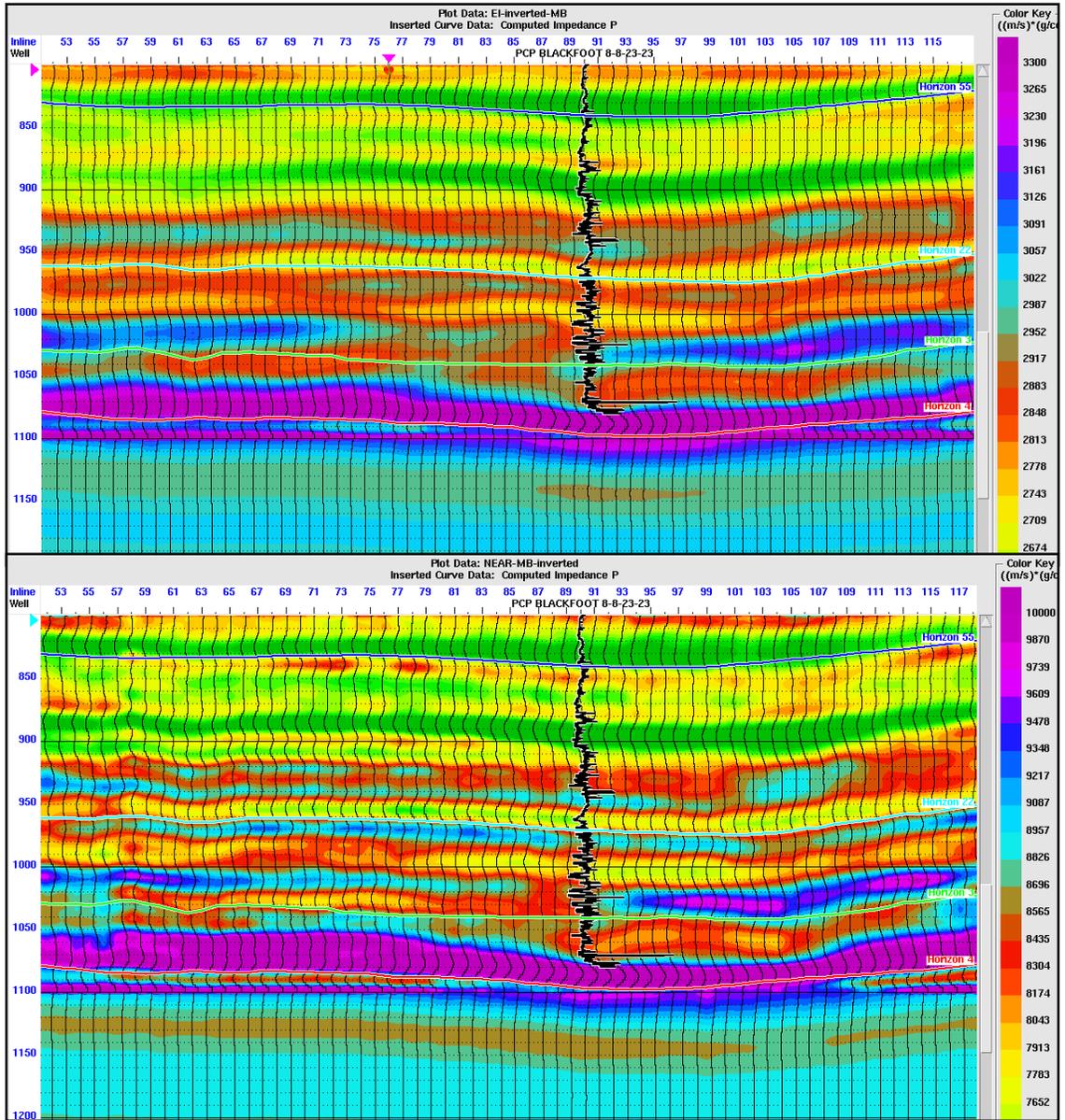
Figure 3.2.12. EI cross-sections of the EI using the model-based method: near-angle (top) and far-angle (bottom). P-wave log in well 8-8 is shown in black.
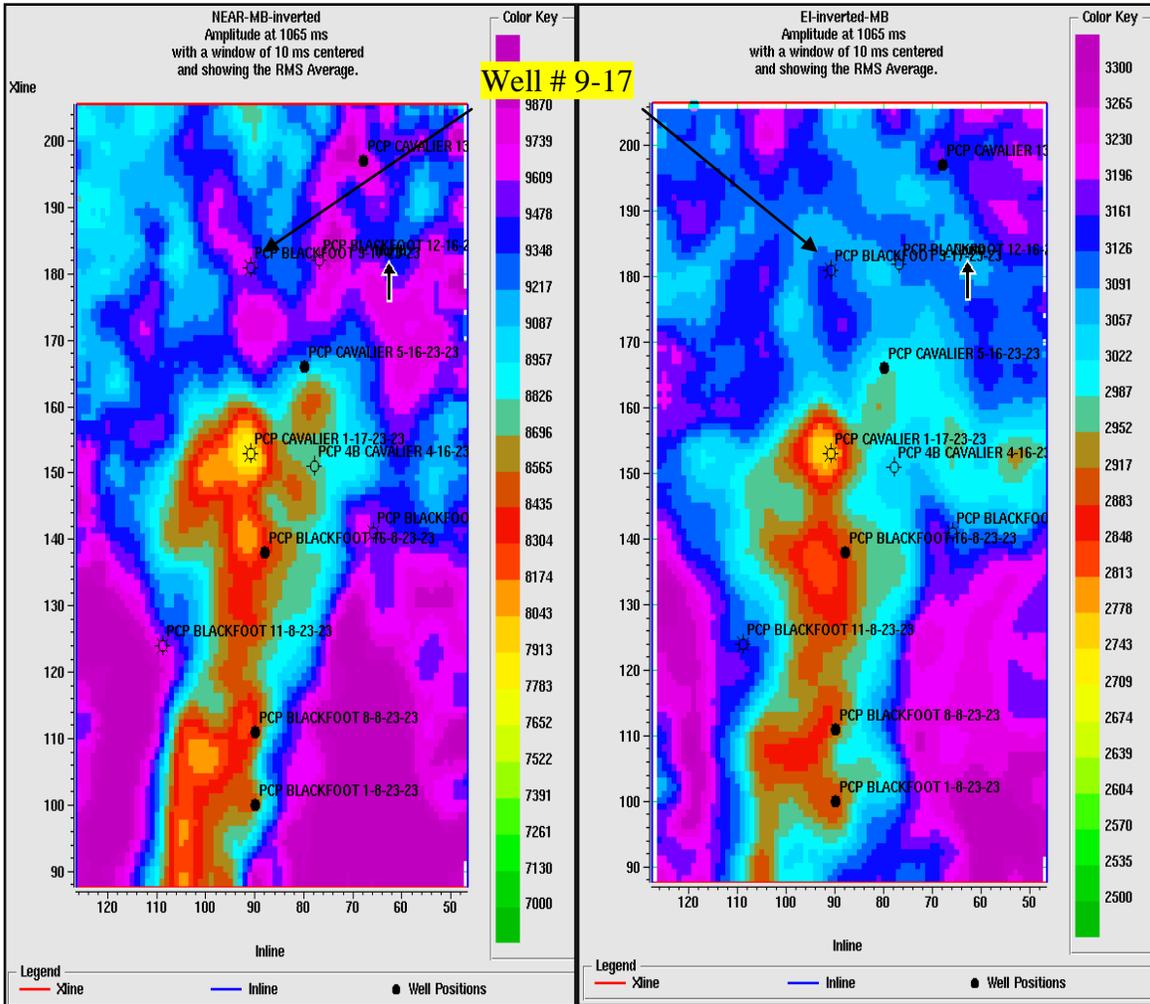
Figure 3.2.13. Slices of EI at time 1065 ms for model-based inversion: near-angle (left) and far-angle (right).

3.3   Simultaneous Inversion of pre-stack seismic data

In pre-stack simultaneous inversion, we invert the CMP gathers to obtain the compressional and shear-wave impedances. This type of inversion was performed by using the H-R STRATA software. Offset CMP gathers were converted to angle CMP gathers, as in EI inversion above, and the same set of horizons was used as in the preceding inversions.

As with other inversion types (except SILC), building an initial model is required. However, in this case, the model should include both the *P*- and *S*-wave impedances. The model was built by using the *P*-, *S*-wave, and density logs at well locations. From these

logs, I constructed the *S*- and *P*-impedance logs, which were further interpolated between the wells to build the models by using horizons as the structure guides for the interpolation. The models were filtered by using a 10-Hz low-pass filter to preserve the low-frequency component and remove the well-log heterogeneity at the seismic frequencies. Figure 3.3.1 shows four selected CMP gathers used in the inversion and the initial model in the form of a stacked seismic section.

Further, a wavelet is needed in order to model the effects of the source signature during the inversion and also for comparisons of the results at well locations. Consequently, a statistical wavelet is extracted, with similar parameters to the statistical wavelet used in post-stack AI inversion above. However, in the present case, it was extracted from NMO-corrected, pre-stack CMP data. The parameters of the wavelet extraction procedure in STRATA were:

- ➢ Start time: 800 ms;
- ➢ End time: 1100 ms;
- ➢ In-line range: 55 to 115;
- ➢ Cross-line range: 95 to 195;
- ➢ Wavelet length: 200 ms;
- ➢ Taper: 20 ms;
- ➢ Phase: zero.
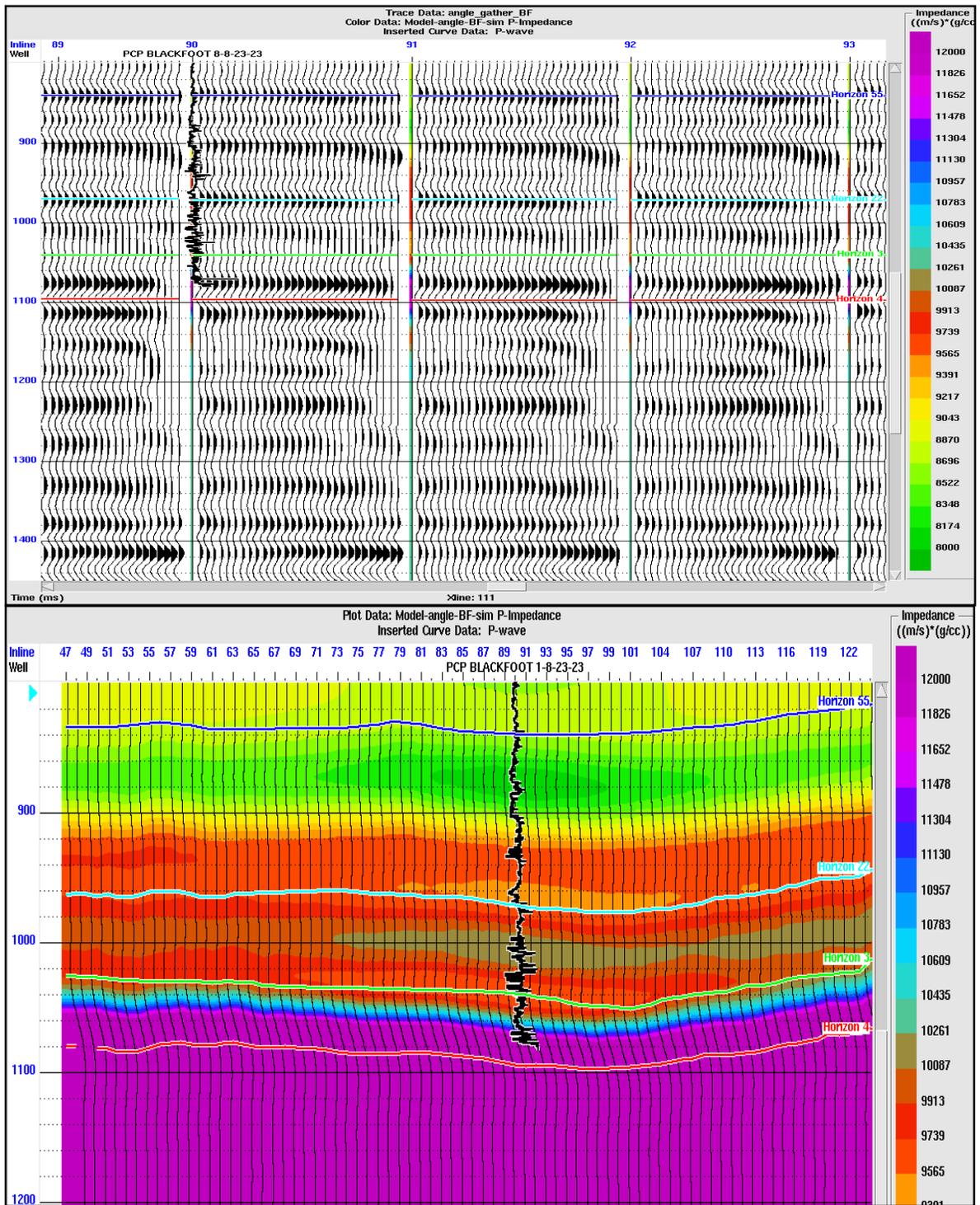
Figure 3.3.1. Top: CMP gathers; bottom: the initial AI model for inversion.

Simultaneous inversion relies on the background relationship between $\ln(Z_P)$, $\ln(Z_S)$, and $\ln(\rho)$ at the well locations, from which the coefficients (k, k_c, m and m_c) are calculated as described in equations (2.4 3) and (2.4 4) (Figure 3.3.2). Deviations of these values from the background Δl_S and Δl_D were calculated from the inversion itself, and therefore they were initialized equal to zero in the initial model. When the coefficients (k, k_c, m, and m_c) were calculated, they were utilized to determine the final inversion.
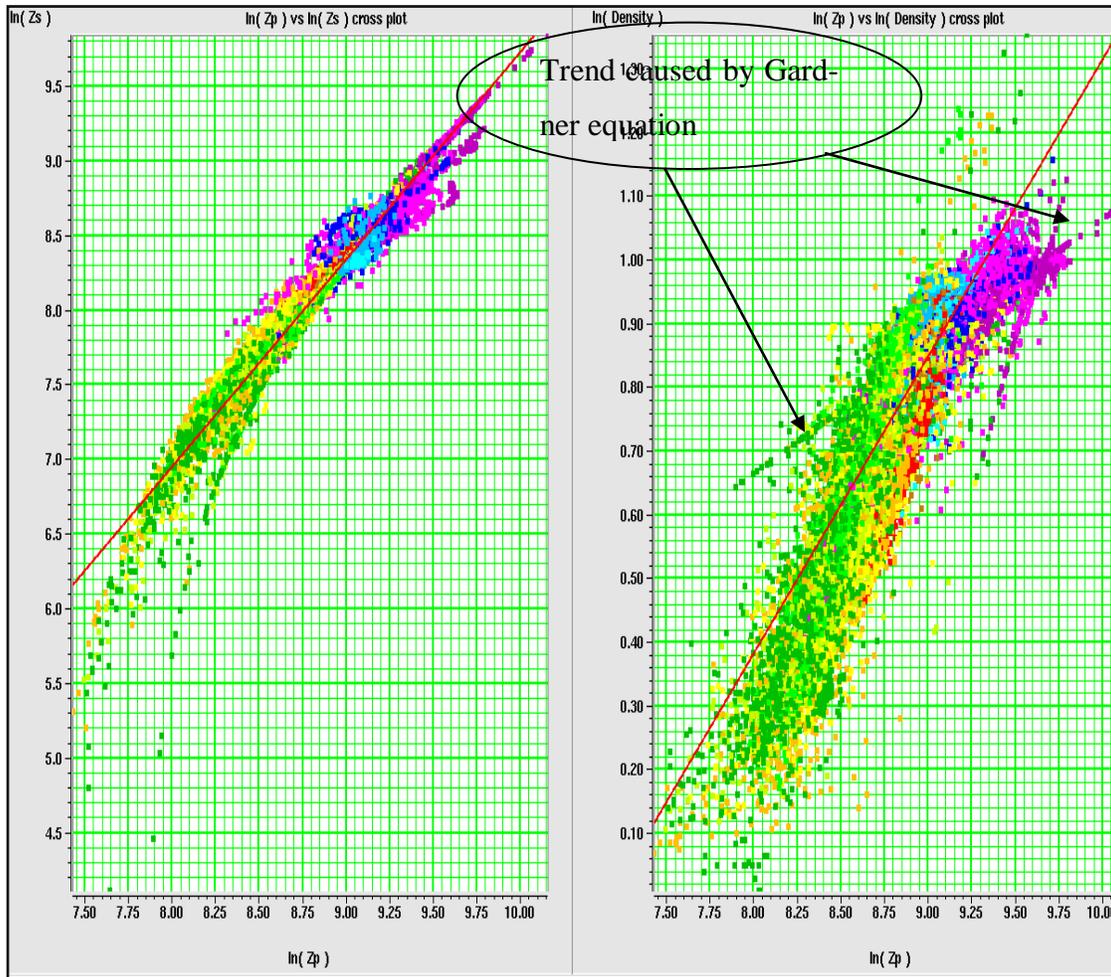
Figure 3.3.2. Well-log data (coloured dots) and the interpreted background relationships between $\ln(Z_P)$, $\ln(Z_S)$, and $\ln(\rho)$ (lines) using all wells in the area. These trends were used to calculate the coefficients (k, k_c, m, and m_c).

94

The wet-trend regression was picked from the cross-plot between the logs of P-and S-wave impedances and densities at different depths (Figure 3.3.2). In this cross-plot, differently coloured points represent crossplot the log values at different depths. For example, green points show logs at shallow depths while pink points are located at greater depths (Figure 3.3.2). The regression line (red) represents the interpreted linear relationship in the wet clastic, which is composed of wet sands and shale. The additional trends visible in Figure 3.3.2 (right) and indicated by arrows are caused by using Gardner's equation to fill several gaps in the density log. This equations resulted in exact linear relationships between the P-wave velocities and densities (eq 2.4.2) in the corresponding parts of the depth interval.

When the coefficients of simultaneous inversion were determined, I ran the inversion in two stages. First, I applied the inversion at the well locations to test the parameters and scale the seismic data. This procedure is also called "analysis quality control." Figure 3.3 3 shows the quality control display at well 5-16. This Figure compares the inversion result of the P-wave impedance (Z_P), S-wave impedance (Z_S) and the velocity ratio V_P/V_S with the corresponding parameters at one well. It also compares the synthetic CMP gathers produced from the inversion result to the corresponding CMP gathers from the seismic data. The correlations between the inverted synthetic and real CMP traces at well locations are shown in Figure 3.3.4, as well as the errors between the original logs and the inverted Z_P, and Z_S results.
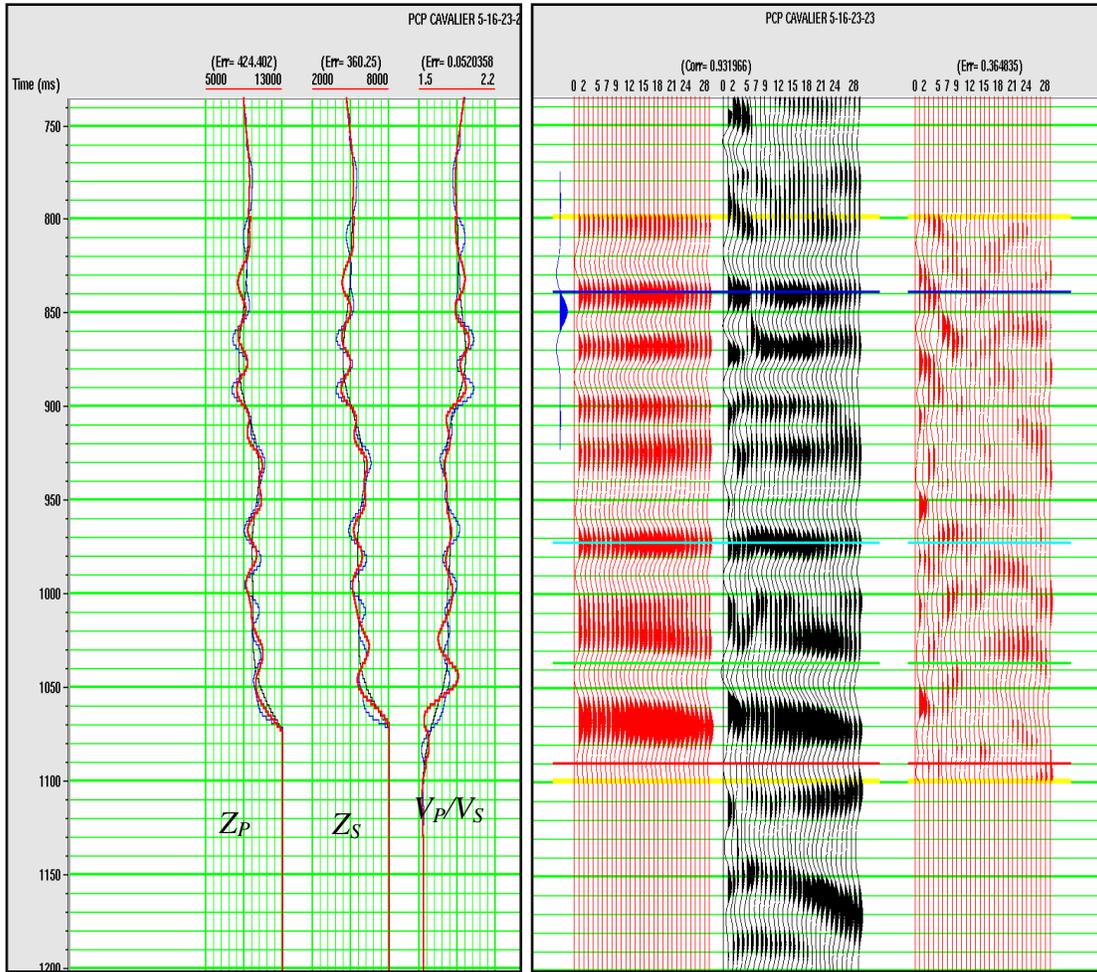
Figure 3.3.3. Left: quality control applied to compare the inverted of P-impedance, *S*-impedance and *V_P/V_S* ratio to the corresponding parameters of the well. Right: comparison of the CMP gather data to the synthetic CMP gather constructed from the inversion result, and the prediction error.
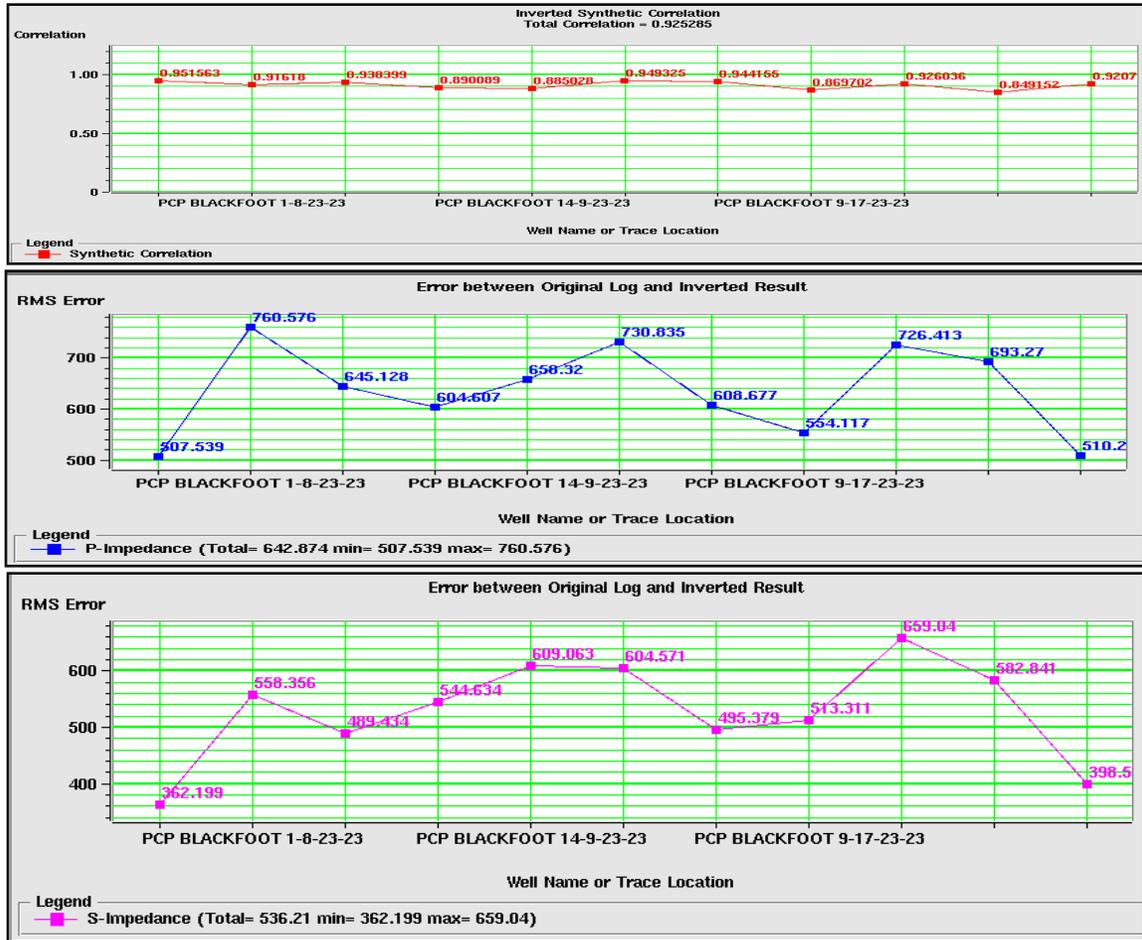
Figure 3.3.4. Red: correlation coefficients between the synthetic seismic traces using the inversion result and the corresponding gathers in the seismic data. Blue: RMS errors in Z_P between the original logs and inverted results for all wells, Z_P; purple: similar errors for Z_S.

When the inversion parameters were deemed correct and the data fit at well-log locations were satisfactory, the inversion was applied to the entire volume of seismic data. However, the density parameter was still excluded from the inversion because the maximum coverage of the angle range was limited to ~30°. At such angles, density has almost no independent effect on the AVA, and angles higher than 40° are typically required for robust inversion for density (Castagna and Smith, 1994). Other parameters of the inversion were as follows:

- ➢ Inversion time: from 800msec to 1100 ms;
- ➢ Range angle from CMP from 0 to 29 degree;
- ➢ Extract wavelet for each angle;
- ➢ Number of iterations: 10;

97

- Separate scales; separate scale for each CMP ;
- Coefficients $k = 1.38, k_c = -4.15, m = 0.46,$ and $m_c = -3.35.$

The inversion results for the *P*-wave (Z_P) and *S*-wave impedance (Z_S) are shown in Figure 3.3.5. In addition, the real and synthetic CMP traces, and the measured differences between them are shown in Figure 3.3.6. Slices of the *P*-impedance and *S*-impedance ratio at the 1065-ms time level, averaged within a 10-ms window in were also taken (Figure 3.3.7). Further analysis and comparison of these images to the results from their methods will be given in Chapter 4.
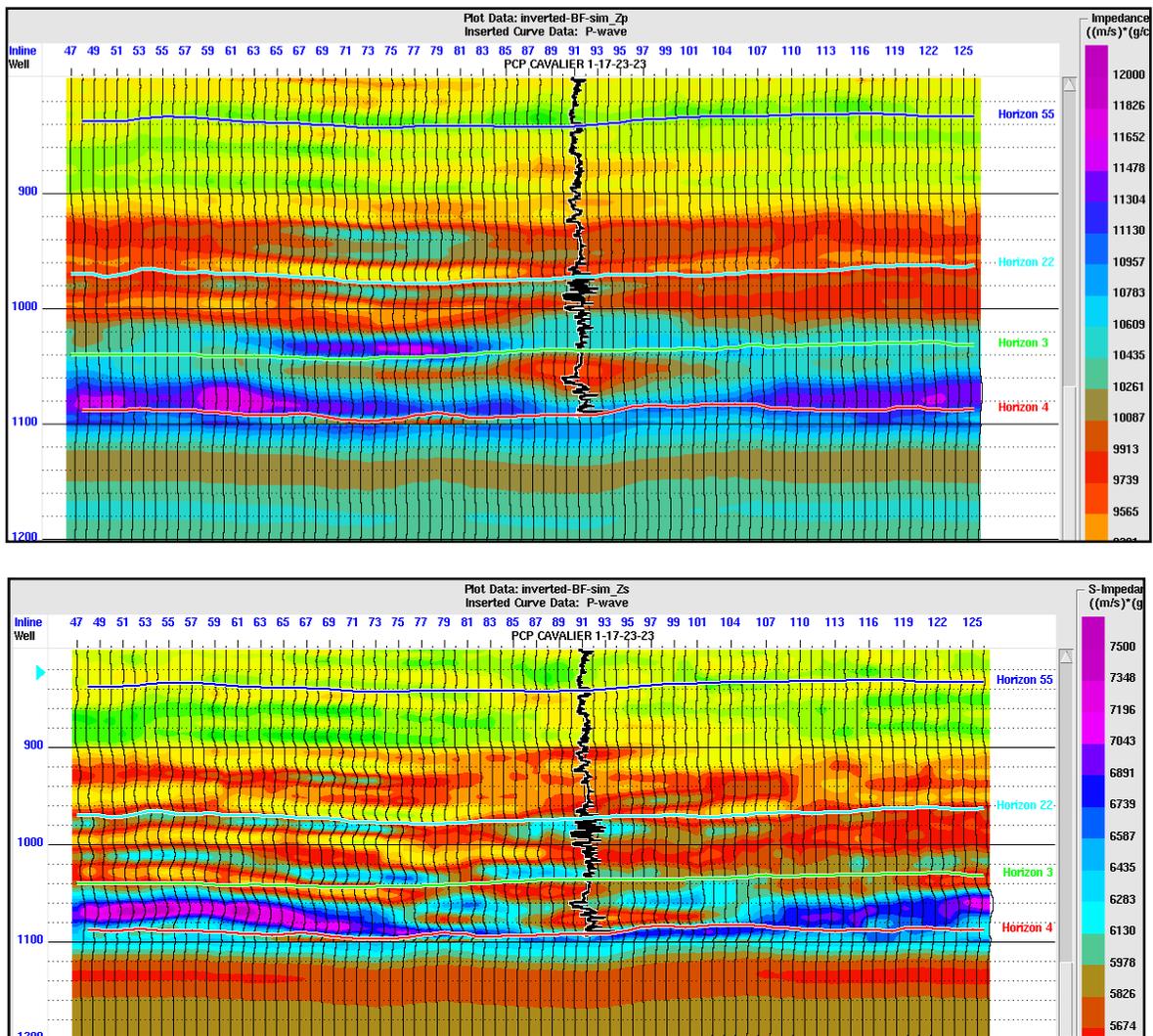
Figure 3.3.5. Cross-sections of the *P*-impedance (Z_P; top) and *S*-impedance (Z_S; bottom) inversion results.
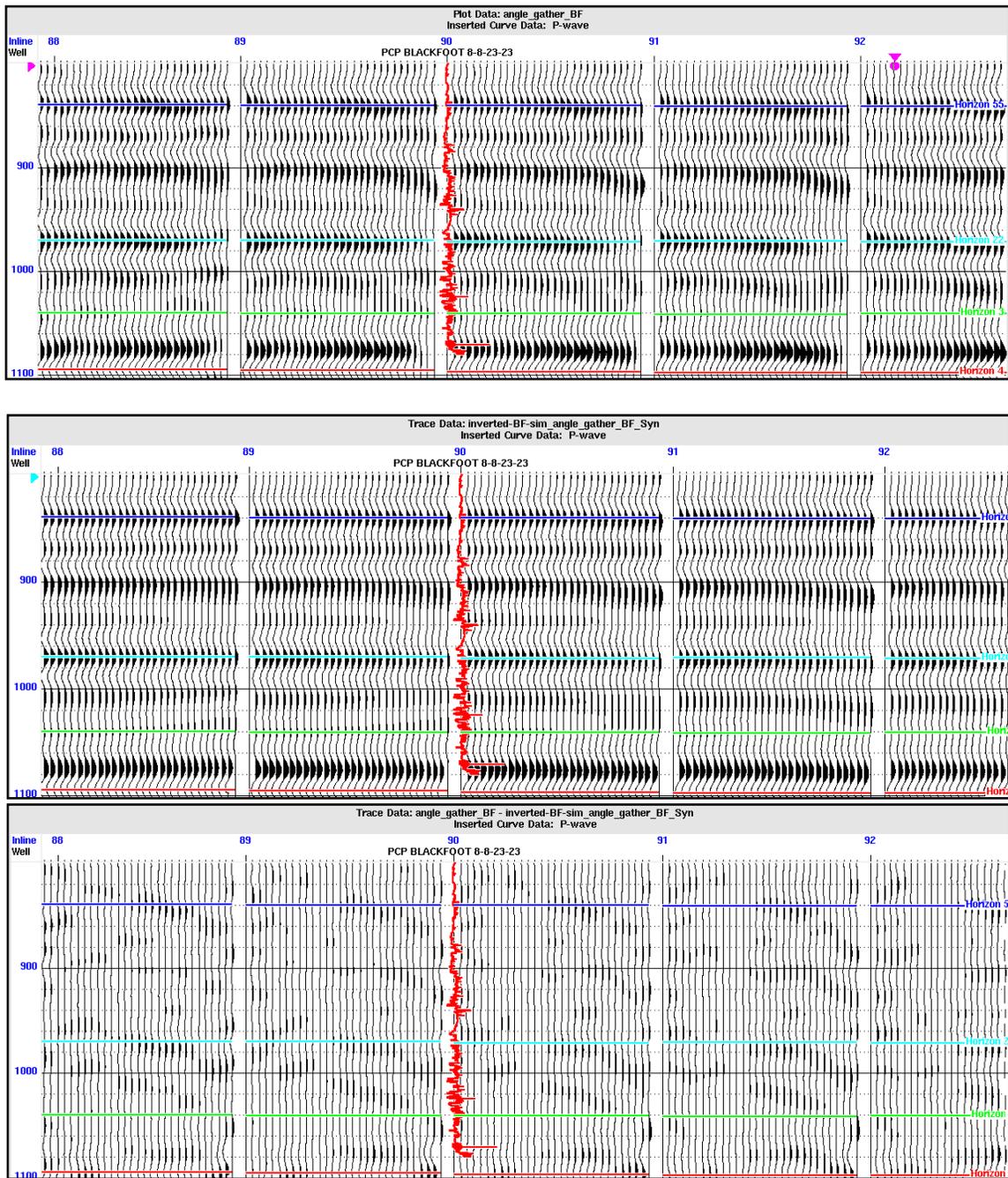
Figure 3.3.6. Top: Selected NMO-corrected CMP gathers from the seismic data; Middle: Synthetic gathers constructed from the inversion result; Bottom: the error (differences) between the real and synthetic CMP gathers. Red line shows the p-wave log in well # 8-8.

99
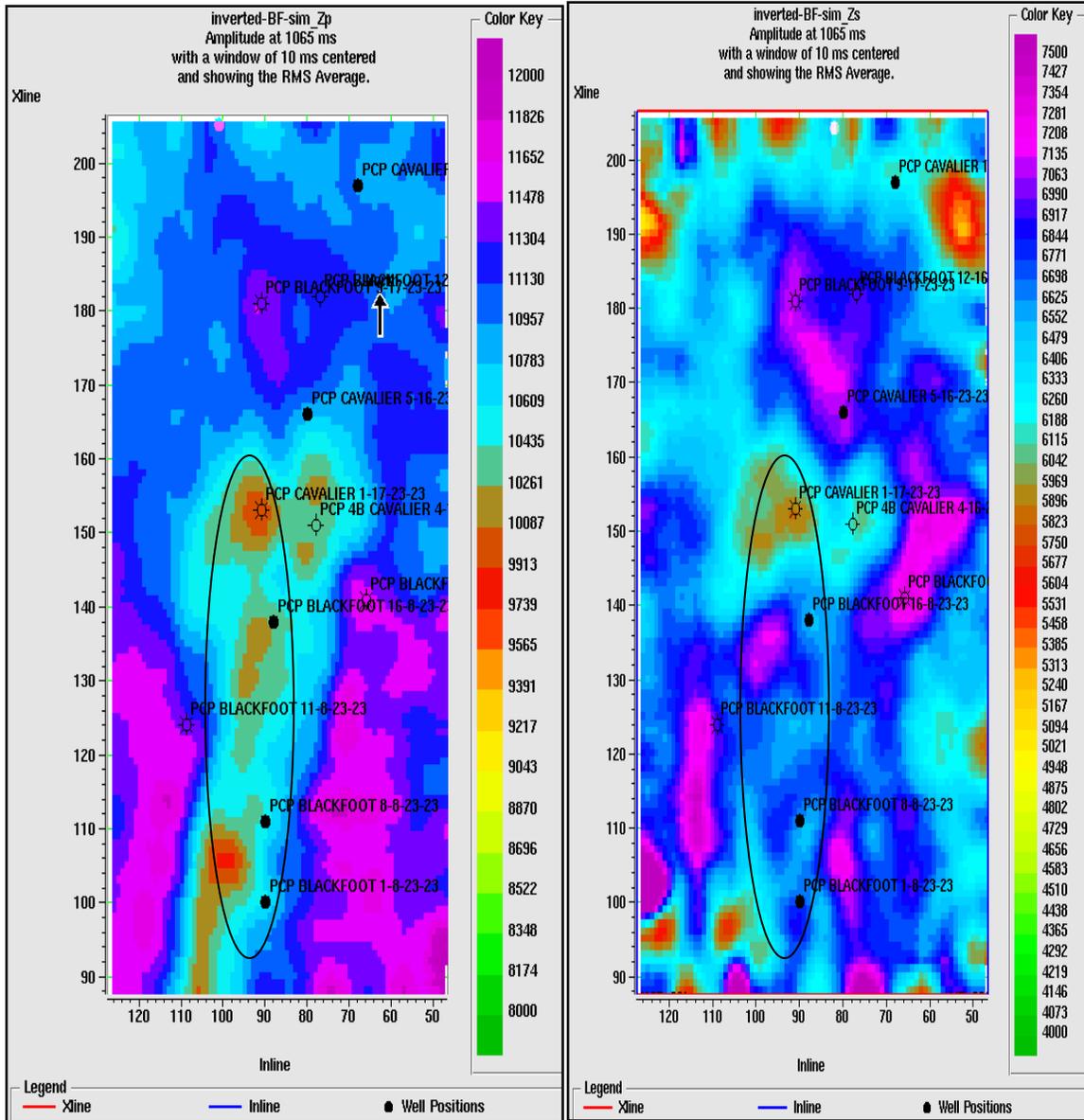
Figure 3.3.7. Time-slice of Z_P (left) and Z_S (right) inversion at 1065 ms. Ellipse shows the channel with low P- impedance and relatively high S-impedance.

3.4 Elastic rock parameters (λ, μ, ρ) and V_P/V_S ratios

LMR (λ, μ, ρ) and the ratio of the compressional- wave to shear-wave velocities (V_P/V_S) are useful attributes that can be extracted from the results of simultaneous inversion. In H-R software, the V_P/V_S ratio is extracted by dividing the P-wave impedance by

100

the corresponding *S*-wave impedance at the same point. Products of $\lambda\rho$ (referred to as the "LR" attribute) and $\mu\rho$ ("MR" attribute) are also extracted from the impedances by transforming them as described in expressions (2.5.3) and (2.5.5).

Cross-sections of these attributes and V_P/V_S ratio are shown in Figures 3.4.1 and 3.4.2, respectively. As above, slices of RMS average of LMR parameters and V_P/V_S ratios taken at 1065 ms time and averaged within 10-ms time windows are shown in Figures 3.4 3 and 3.4 4. These images will be further discussed in Chapter 4.
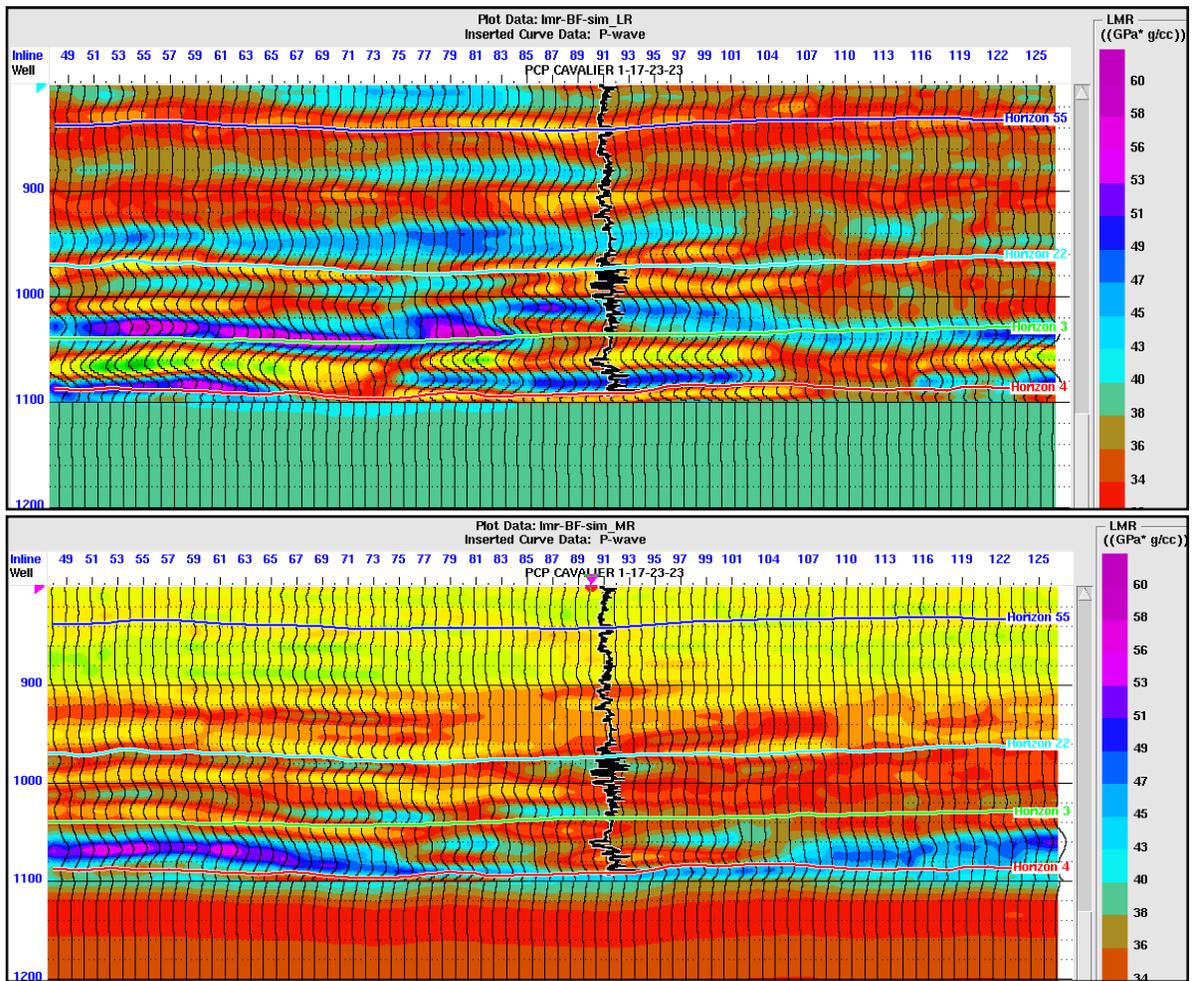
Figure 3.4.1. Cross-section of the LR attribute resulting from the simultaneous inversion. Cross-section of the MR attribute.
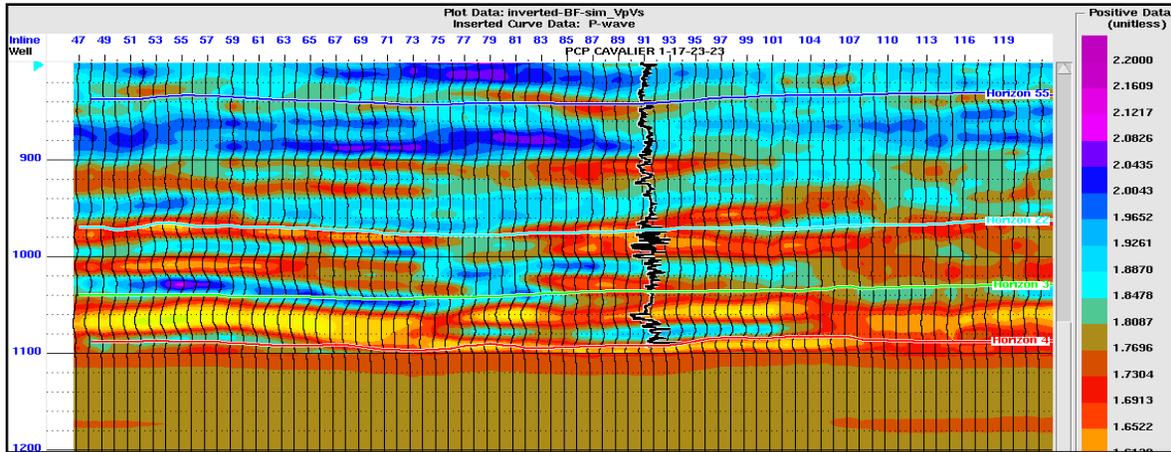
Figure 3.4.2. Cross-section of the V_P/V_S ratio derived from simultaneous inversion.
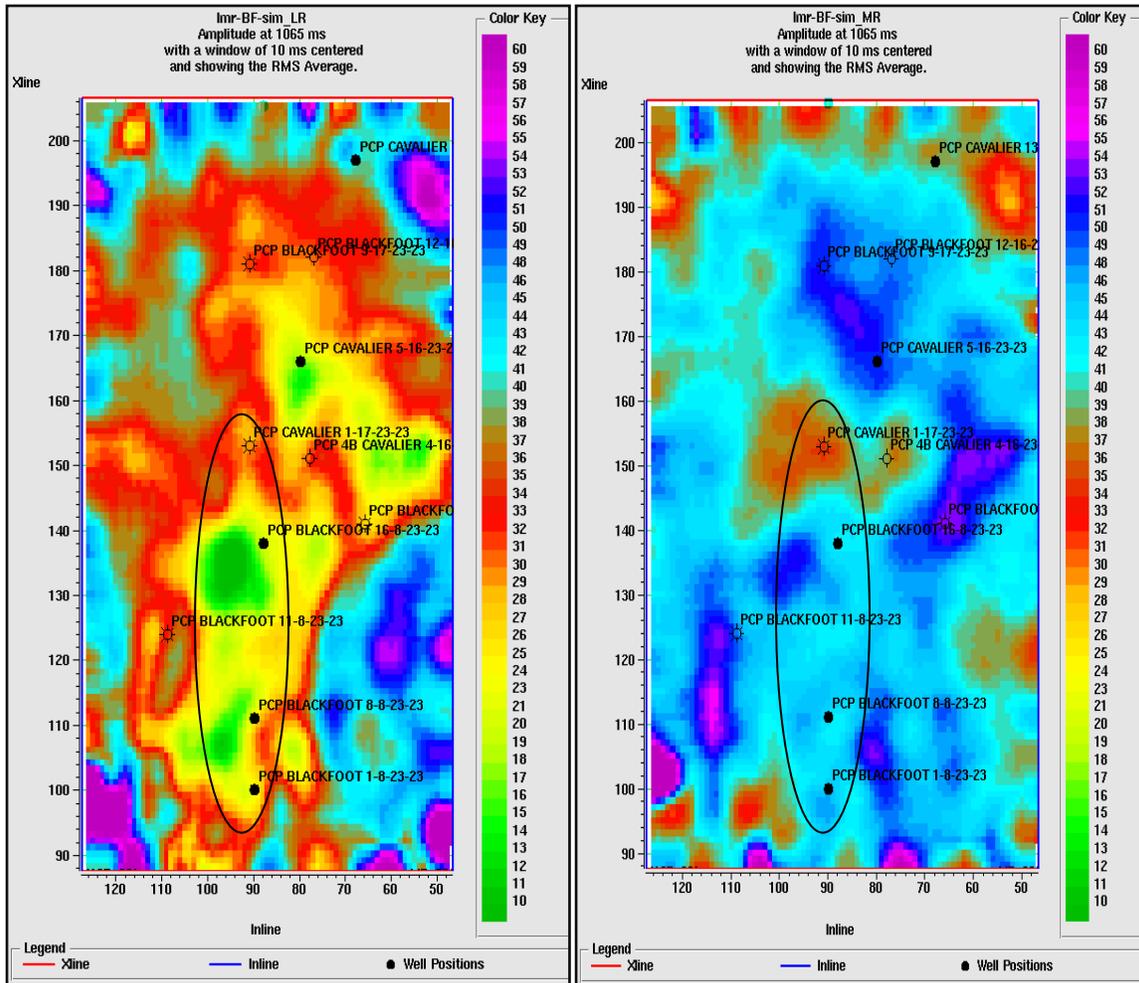
Figure 3.4.3. Left: Time slice of LR inversion at 1065 ms. Right: time slice of MR inversion at 1065 ms. The ellipse show the low LR (left) and high MR in the channel.
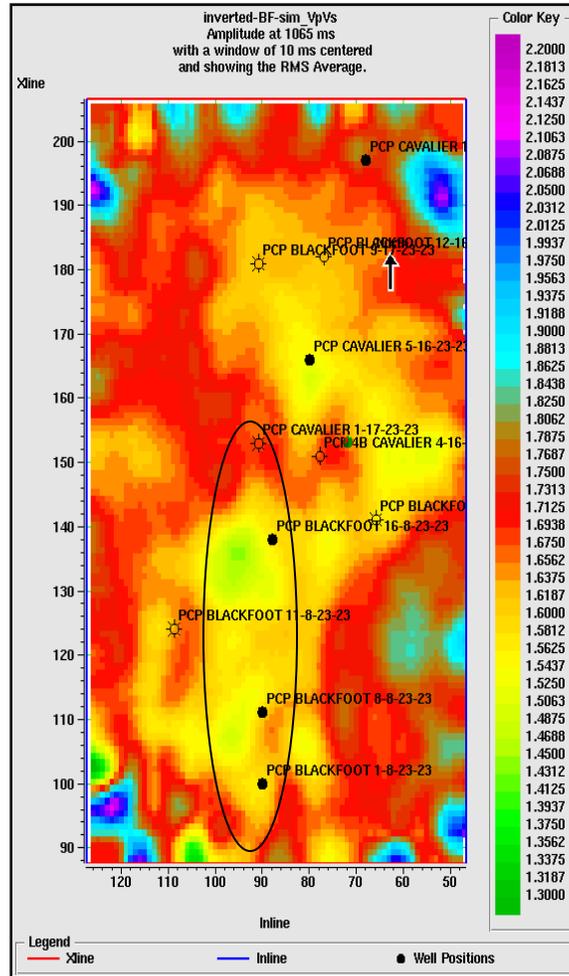
Figure 3.4.4. Time slice of V_P/V_S inversion result at 1065 ms time. The ellipse shows a zone of low V_P/V_S within the channel.

3.5 AVO attributes from Blackfoot CMP gathers

AVO attribute volumes, such as the intercept (*A*), gradient (*B*) and their combinations, such as the AVO product (*AB*), Poisson's ratio (*A+B*), shear reflectivity (*A-B*) and fluid factor (FF), are produced directly from NMO-corrected CMP-sorted pre-stack seismic data . Figure 3.5 1 shows the curves of the amplitude variations with incidence angles for several CMP gather selected from the dataset. These amplitude curves are utilized to estimate the intercept (*A*) and gradient (*B*) values. In the H-R software package, the AVO attributes volumes are built from the CMP angle gathers by using the following procedure:

➢ Attributes *A* and *B* are calculated for each sample time as described in equation (2.1 3) (Figure 3.5 2).

- ➢ From A and B, combinations (AB), ($A+B$) and ($A-B$) are produced (Figures 3.5 3, 3.5 4 and 3.5 5).
- ➢ P-wave reflectivity (R_P) and S-wave reflectivity (R_S) attributes also constructed by using equation (2.1.8) (Figure 3.5 6).
- ➢ From R_P and R_S attributes, Fluid Factor volumes are constructed as given in equations (2.1.13) (Figure 3.5 7).

The seismic parameters used for computing the attributes were as follows:
- ➢ Time window: 0 - 2000 ms;
- ➢ In-line range: 47 - 126;
- ➢ Cross-line range: 80 - 205;
- ➢ Angle range: 0 to 30°.

The AVO attribute volumes resulting from such combinations of the primary AVO intercept and gradient are further discussed in the following Chapter.
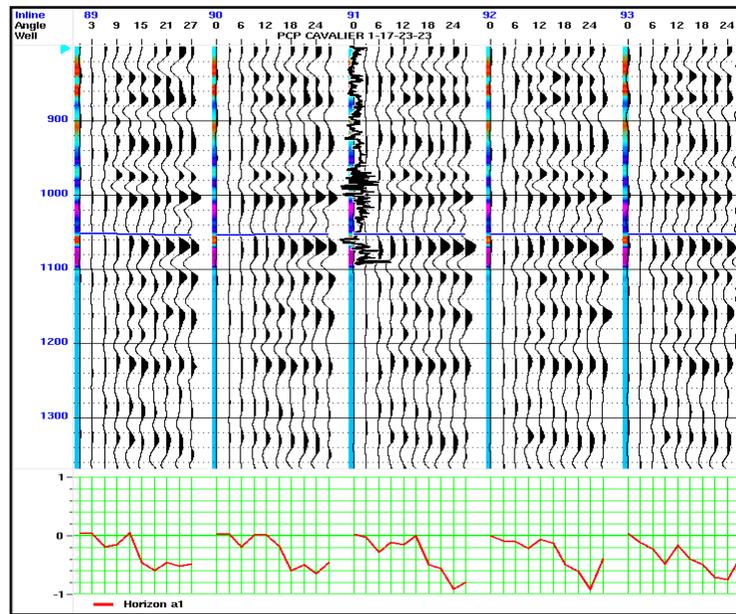
Figure 3.5.1. CMP gathers (top) and the variation of reflection amplitude with angles (bottom) at horizon a1. Horizons are shown in Figure 3.1.5.
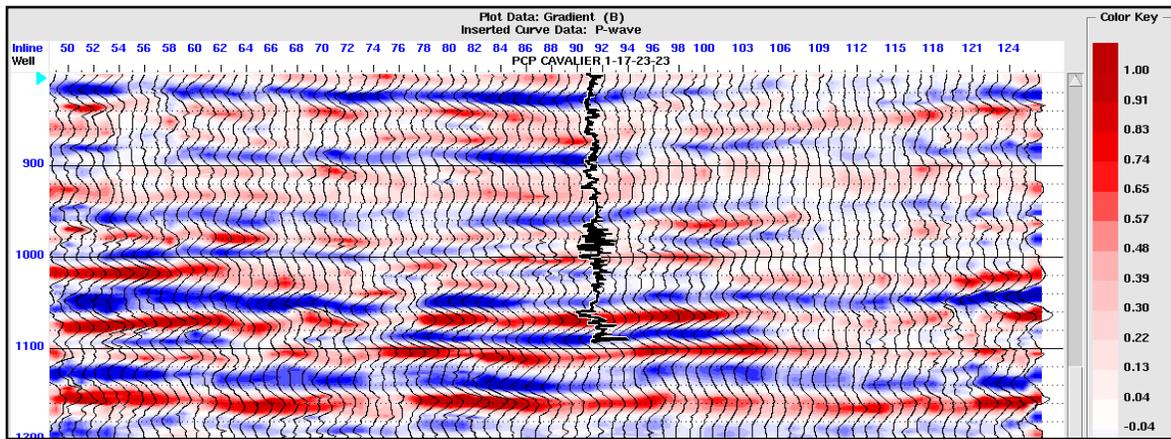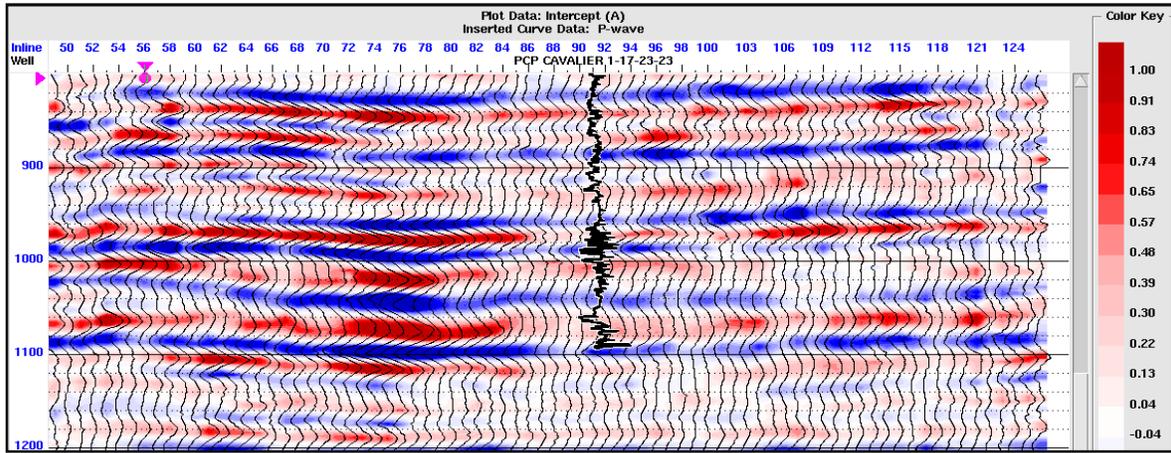
Figure 3.5.2. Intercepts *A* (top) and gradients *B* (bottom) in a line crossing gas well #1-17. Black line shows the *P*-wave log in the well.
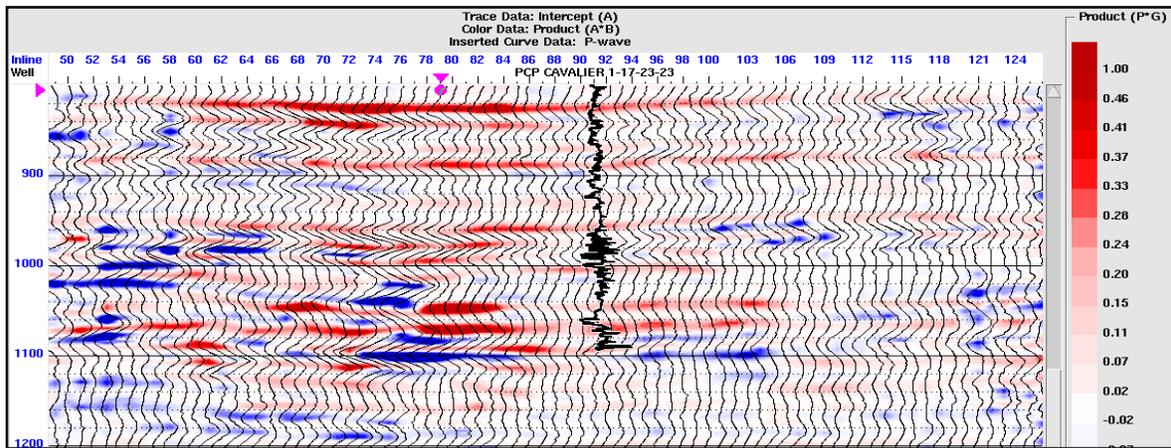
Figure 3.5.3. The same section as in Figure 3.5.2 showing product *AB*.
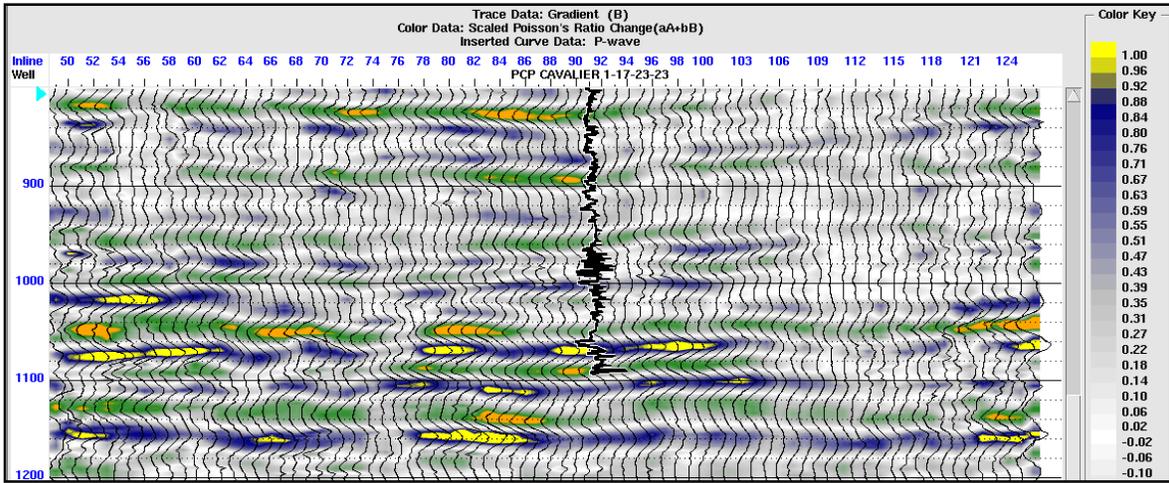
Figure 3.5.4. Poisson's ratio *A+B* section at the gas well # 1-17.
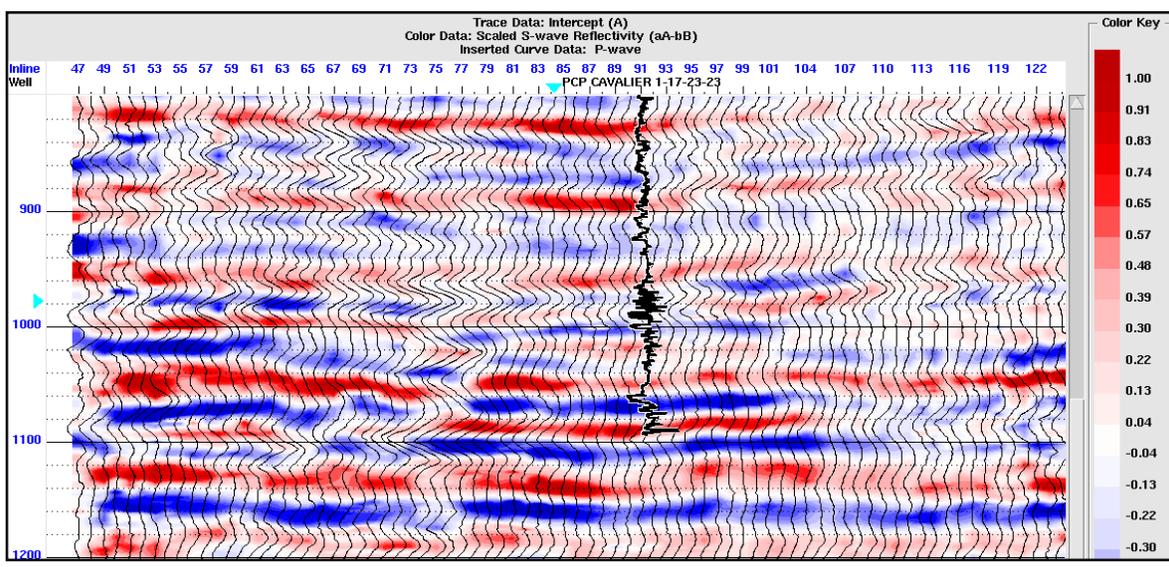
Figure 3.5.5. Scaled *S*-wave reflectivity *A-B* section near gas well # 1-17.

106
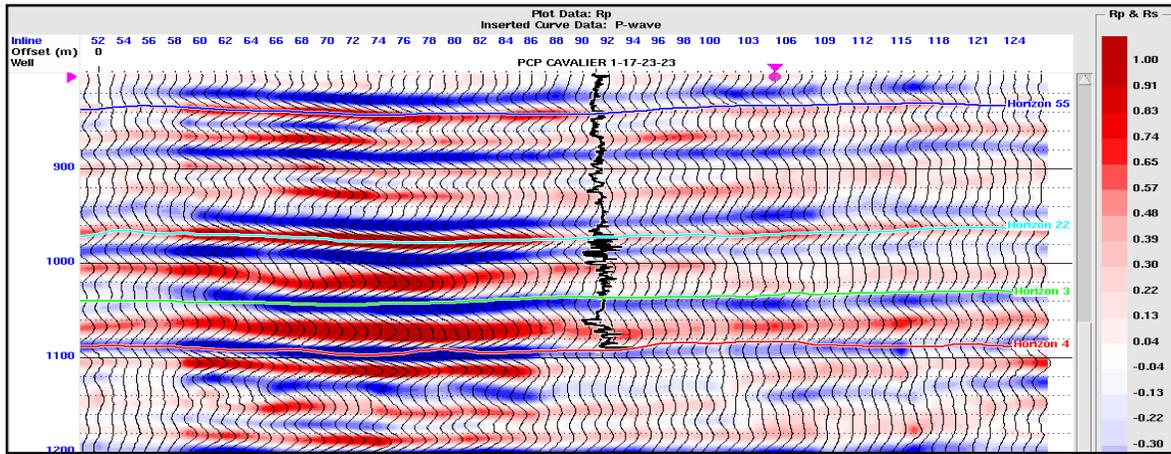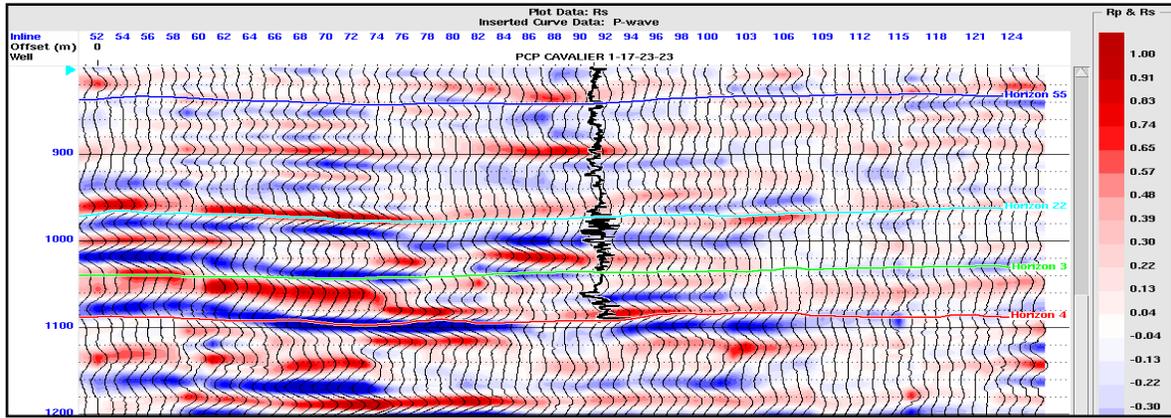
Figure 3.5.6. *P*-wave reflectivities (R_P) (top) and *S*-wave reflectivities (R_S) (bottom), used to extract the Fluid Factor (FF) near gas well #1-17.
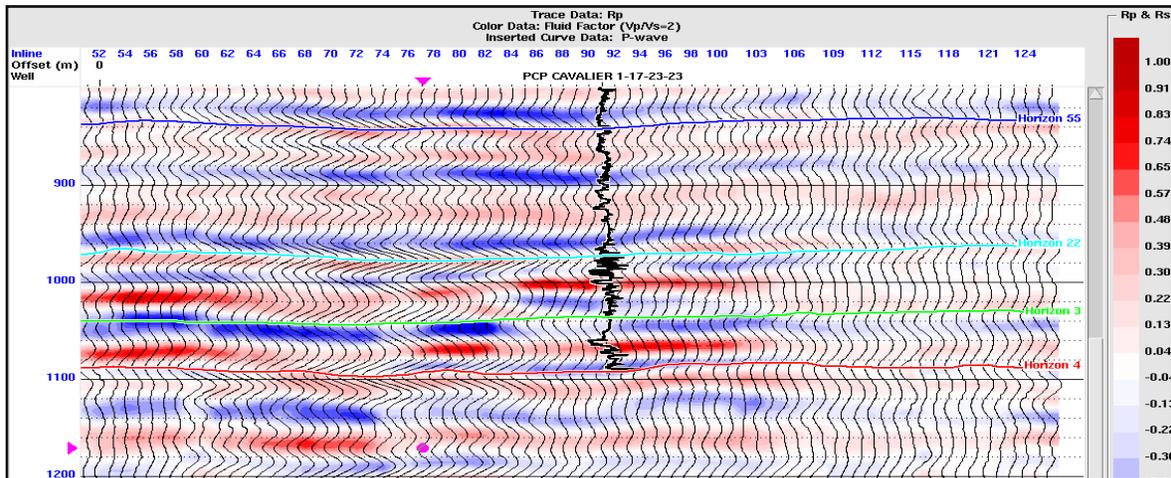
Figure 3.5.7. Fluid factor section near gas well # 1-17.

4   Results and discussion

As mentioned in Section 1.4, the primary target of interest in the Blackfoot field is the lower-Cretaceous age, Glauconitic sandstone incised valley deposits. This channel contains hydrocarbon sand plugged with shale. The hydrocarbon sand has lower impedance compared to the surrounding shale in the channel. Since the sand reservoir is thin, it is hard to see the corresponding reservoir horizon in the seismic data. However, from the correlation between seismic data and well logs, the reservoir is located at around 1065 ms time below horizon #3. This Chapter discusses the results of the different inversions and attributes applied to the dataset, and compares the results of these methods.

The first group of methods applied to the data was the post-stack AI inversion. Four algorithms were used, as described in Section 3.1. Three of these algorithms (band-limited, model-based and coloured inversions) were closely related and based on the H-R software. These algorithms were tested at the well locations to compare the AI inversion results to the log impedance at the wells as shown in Section 3.1(Figures 3.1.11, 3.1.15 and 3.1.20). These methods produced similar results, and the tests showed reasonable RMS average variations at the target depth, which ranged from 500 (m/s)·(g/cc) to 1000 (m/s)·(g/cc). For SILC inversion, there is no need to compare the inversion results at the wells, because in this algorithm the seismic inversion is derived from the well-log impedances and matches them at the wells automatically. In other words, the residual error cannot be used as a measure of inversion quality in this approach, and the method has practically no parameters to adjust. Three significant differences were found in comparing the SILC approach to the H-R based inversions: 1) it showed somewhat lower average impedance values compared to the other methods, 2) it appeared to give higher vertical resolution and improved horizontal layer consistency in terms of geology, and 3) the spatial distributions of AI inverted by SILC were significantly different from their H-R counterparts.

The similarities between the H-R inversions and their differences from SILC are likely related to the fundamental uncertainty of the impedance in respect to scaling. Seismic impedance values can be multiplied by a slowly-varying factor without changing the observed reflectivity. During any inversion, this factor is largely determined by the background impedance model and by the algorithm. The SILC algorithm explicitly exploits this

uncertainty in order to produce its images (Morozov and Ma, in press), whereas in H-R inversions, this uncertainty is controlled by construction of the initial model, scaling of the seismic data, selection of the wavelet, and regularization of the inversion. As Morozov and Ma (in press) argue, much of the process of "seismic inversion" is actually only a procedure for finding a plausible solution to the convolution equation by using a selected set of geological and algorithmic constraints. The most important of these constraints is the background (starting) model. It appears that all H-R algorithms introduce the background model in similar ways, which therefore result in similar images. Note that in H-R quality control (for example, Figure 3.1.10), only band-pass filtered log impedance is compared to the seismic impedance results, and therefore a bias toward higher average impedances in the model is still possible. By contrast, in SILC method, there is no background model, and the results are extrapolated directly from well-log impedances at all frequencies. Therefore, H-R results may produce exaggerated average impedances, and SILC may be more accurate in this regard. However, as shown below, all of these methods captured the vertical impedance variations similarly, and lead to similar interpretations. In addition, unfortunately, different methods of spatial interpolation should affect all of these techniques, which was clearly illustrated by the differences in the shapes of the time slices (Figure 3.1.23 and 3.1.24)

The resulting AI images were shown in Chapter 3.1 (Figure 3.1.12, Figure 3.1.16, 3.1.21 and 3.1.23). Enlarged views of the same section are shown in Figures 4.1 and4.2. The low-impedance zone was indicated by ellipses located near 1065-ms time level corresponding to the reservoir. This low AI varied from ~9300 to 9800 (m/s)·(g/cc). Note the high impedance of the Mississippian carbonate below the reservoir. The algorithms of the H-R package gave similar results, except that in the model-based method, the image appeared to be more spatially coherent. Although the SILC algorithm showed quite a different image and lower-AI background, the relative low impedance in the reservoir was also indicated.
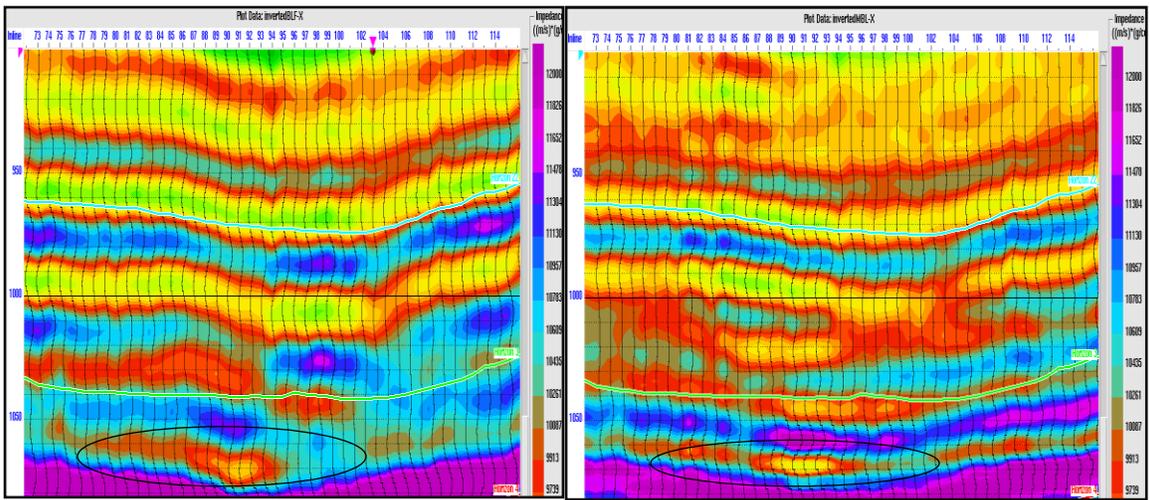
Figure 4.1. Cross-section of the AI across the channel, by using the band-limited (left) and model-based (right) inversion. Ovals indicate the interpreted zone of low AI related to the reservoir.
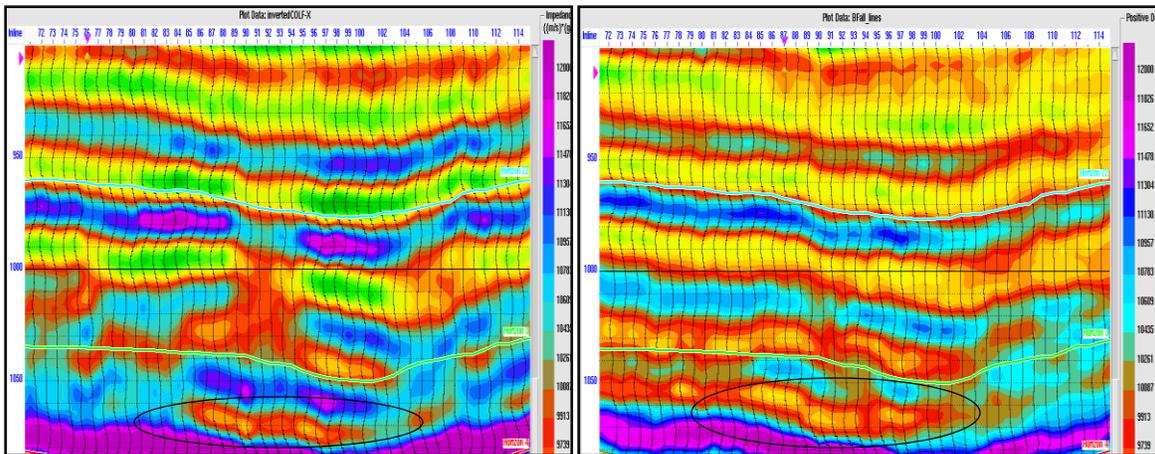
Figure 4.2. Cross-section of the AI across the channel, by using coloured (left) and SILC (right) inversion. Ovals indicate the zone of low AI related to the reservoir.

The areal distribution of the AI can be emphasized by taking its slices at the reservoir depth. Figures (Figures 3.1.17, 3.1.19 and Figure 3.1.22) in Section 3.1 show the RMS AI averages within a 10-ms window centred at the 1065-ms reflection time. The band-limited and model-based methods show similar distributions of the AI, because the low-impedance zone is located from ~1060 ms to ~1070 ms of two-way reflection travel time. However, the coloured inversion shows the low-impedance zone located between 1065 to 1075 ms (Figure 3.1.22), which leads to a different distribution of the window-averaged impedance. To elucidate this difference, I took another slice at 1070 ms time depth with no averaging time window (Figures 4.3 and 4.4). The low-impedance zone at this time-depth also shows the channel very nicely in H-R images, but the SILC method again gives quite a different distribution (right, Figure 4.4) The difference may be due to the higher depth resolution of SILC method causing more spatial detail as well. In addition, spatial interpolation schemes used in H-R and SILC are also strongly different.

The sand reservoir is thin, and therefore the 10-ms average RMS impedance distribution at depth 1065 ms could be dominated by the combined impedance of the sand and shale. However, the low-impedance distributions seen at ~1070 ms (without averaging), could be due to touching the sand reservoir. Note that the high impedance surrounding the channel should correspond to the Mississippian carbonate (Figure 4.1 and Figure 4.2).
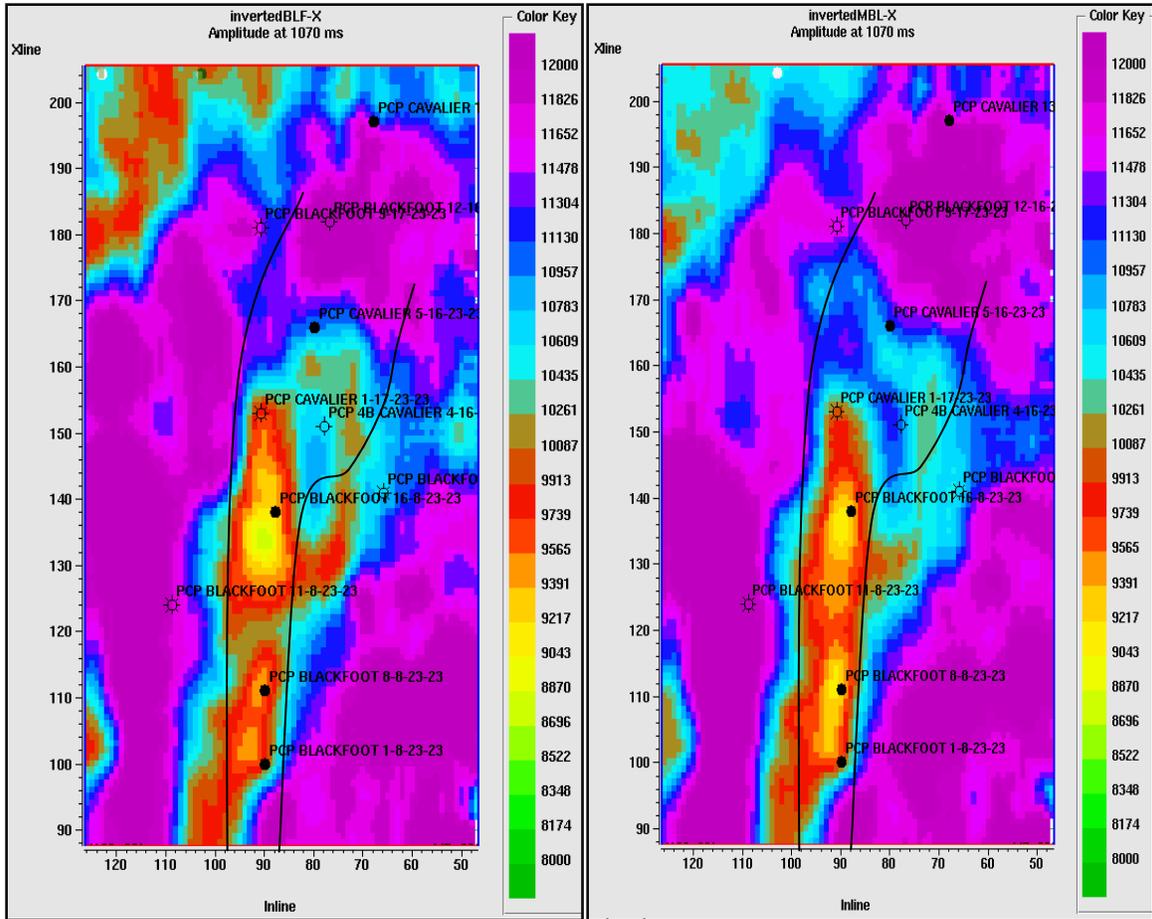
Figure 4.3. Impedance slices at 1070 ms time depth: band-limited (left) and model-based (right). The low-impedance zone is seen clearly in the channel. Purple colour corresponds to the Mississippian carbonates.

112
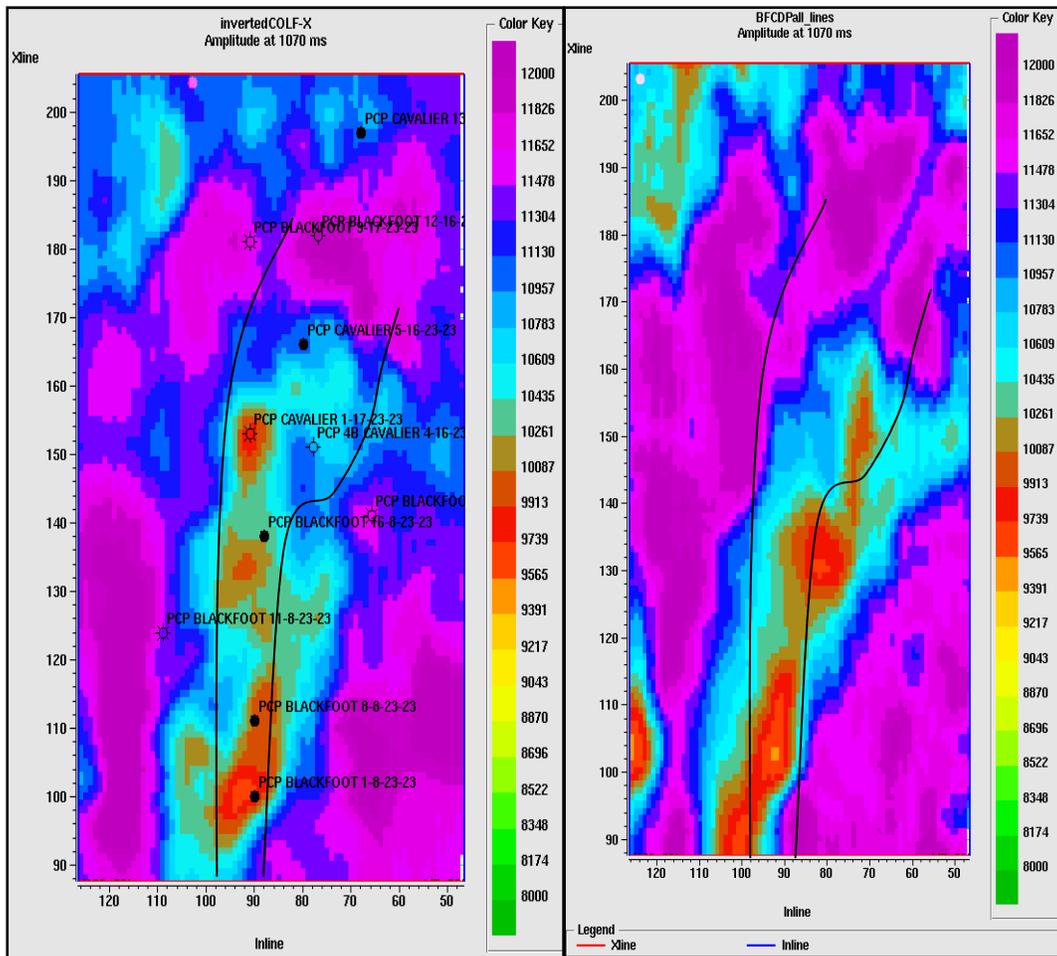
Figure 4.4. Impedance slices at 1070 ms time depth: coloured (left) and SILC (right). The low-impedance zones are shown clearly in the channel. Purple colour corresponds to the Mississippian carbonates.

SILC inversion result show lower average impedance values compared to the H-R methods, and this lower average may affect the visual perception of results when plotted in the same colour scales. Therefore additional cross-section plots were made with a different colour palettes tying to approximate similar distributions of colours. as in H-R plots, Instead of extending from 8000 (m/s)·(g/cc) to 12000 (m/s)·(g/cc), the new plotted AI ranges start from 8300 (m/s)·(g/cc) and extend to 11800 (m/s)·(g/cc) which is comparable to H-R methods (Figure 4.5). The resulting colour image shows a more similar impedance distribution to the AI patterns from H-R inversions. The new image still shows the higher vertical and horizontal resolution of SILC technique.

113

The impedance distribution for the area was also taken at 1065 ms time-depth with 10 ms time window and at 1070ms with. The plot now indicates the low-impedance areas within the channel more clearly (ellipses), which were invisible when using the H-R colour range (Figure 4.6). Note that the low impedance trend in the channel correlates with the negative RMS amplitude anomaly in the channel in Figure 1.5.7, which show the same trend related to reservoir.
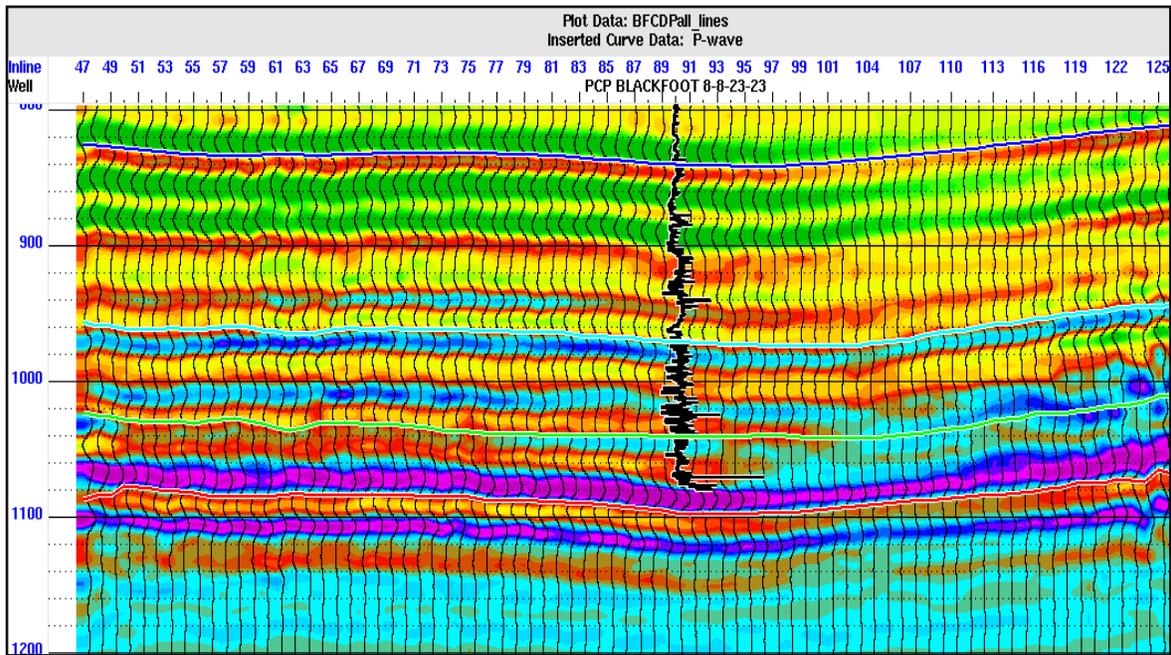
Figure 4. 5. Cross-section of the AI across the channel with average values from 8300 (m/s)·(g/cc) to (m/s)·(g/cc)11800.
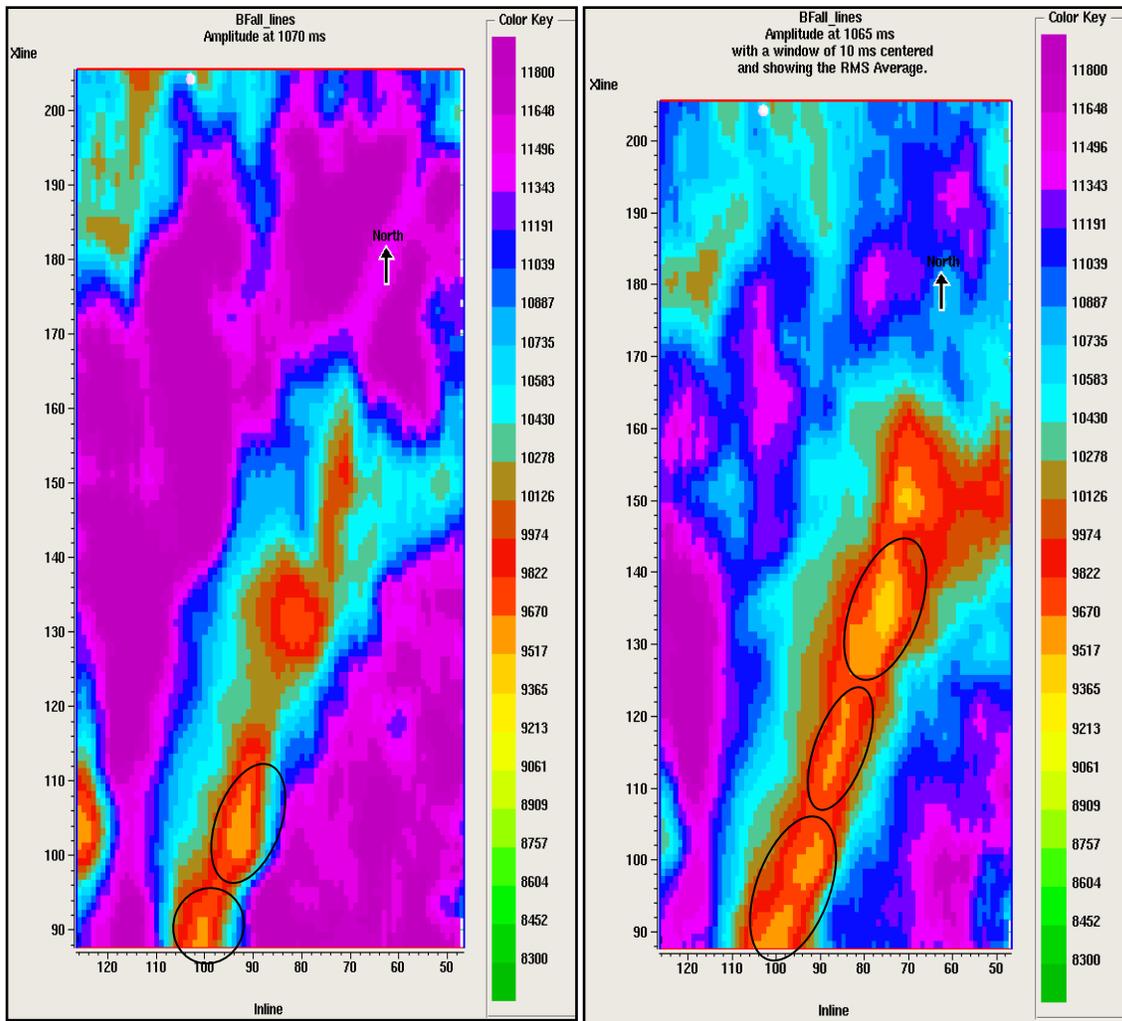
Figure 4. 6. Impedance slices with colour palettes modified to match the H-R results: at 1065 ms time depth with average of 10 ms time window (left) and 1070 ms time depth (right). The low-impedance zones are shown more clearly in the channel (ellipses).

The Elastic Impedance inversion was applied to the range-limited stacked data by using band-limited and model-based inversion methods as described in (Section 3.2). The values of the RMS impedance variations from the background at the depth of interest ranged from 500 (m/s)·(g/cc) to 700 (m/s)·(g/cc) for near-angle stacks and from 110 (m/s)·(g/cc) to 170 (m/s)·(g/cc) for the far-angle stack for both band-limited and model-based inversion methods. Cross-sections of elastic impedance resulting images were shown in Section 3.2 (Figure 3.2.7 and 3.2.13). The same sections in larger scale and centred on the channel are shown in the Figures 4.7 (band-limited) and 4.8 (model-based). The low-impedance zones indicated by the ellipses near 1065-ms times correspond to the target reservoir. The reser-

115

voir shows somewhat lower EI from the model-based inversion compared to the band-limited method. In the model-based method, the match between the created synthetic and real seismic data is higher than in the band-limited method (Figures 3.2.5 and Figure 3.2.9). This could be due to the fact that in the band-limited method, the model within the seismic band is derived entirely from the seismic data (similarly to SILC method), whereas in model-based inversion, the model is influenced by the initial model and by the process of iterative inversion (Section 2.2).

The Mississippian carbonates below the reservoir confirm their high elastic impedances at both near and far angles. The far-angle inversion usually indicates a significant contrast in the impedance for gas reservoirs; however in our case, this contrast was not observed. Such limited success of EI could be explained by the narrow maximum aperture (29°) at the reservoir level in this data, which was not sufficient to produce a significant EI contrast at the gas reservoir. However, the far-angle inversion still supports the low-impedance contrast in the reservoir, similarly to the near-angle inversion.
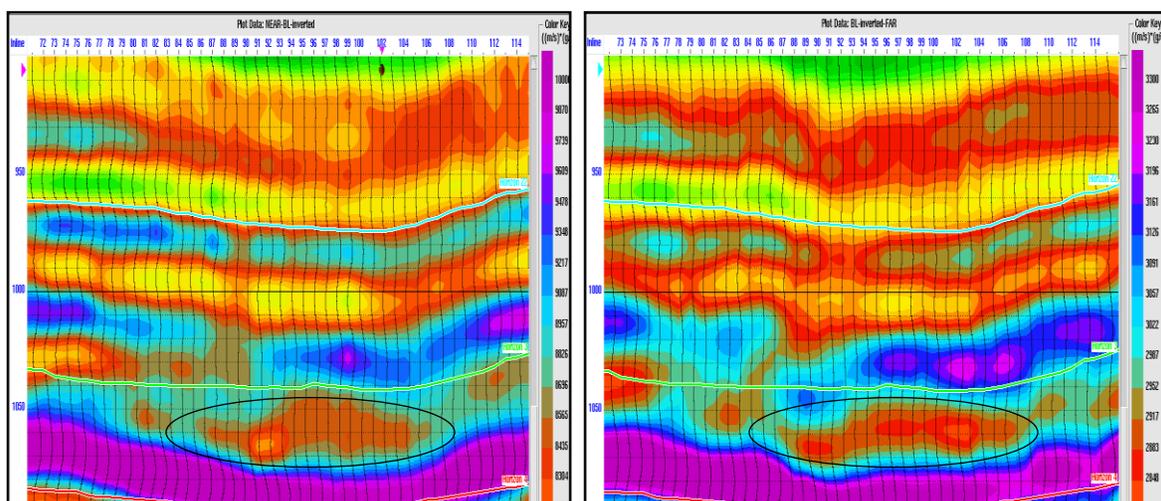
Figure 4.7. Cross-sections of the near-offset (left) and far-offset (right) EI across the channel, using the band-limited inversion method

116
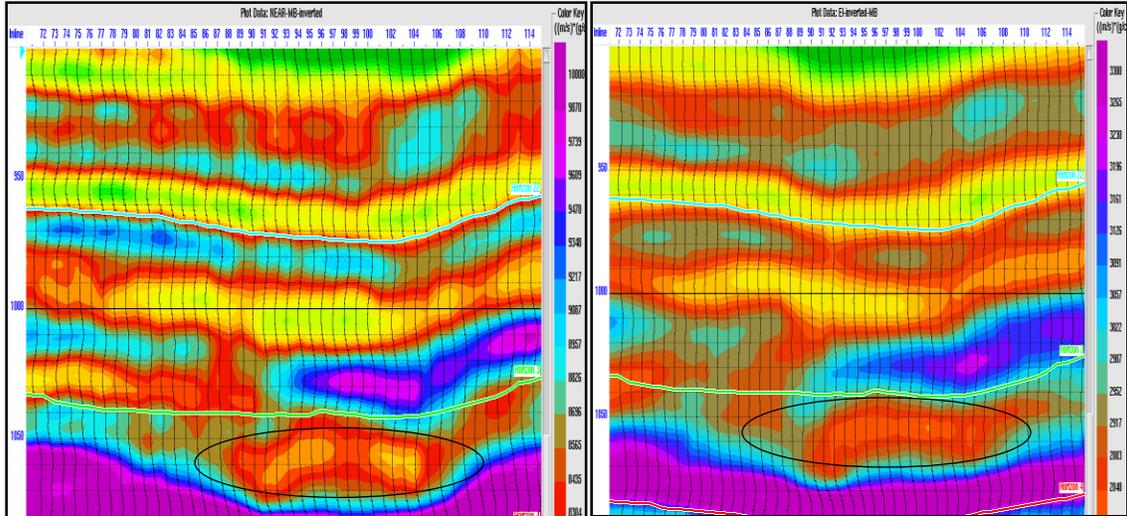
Figure 4.8. Cross-section of the EI across the channel using the model-based method at near (left) and far angles (right).

The complete EI distributions were shown in Section 3.2 (Figures 3.2.9 and Figure 3.2.13). In the band-limited inversion method, the far-angle inversion, showed slightly lower impedance values at 1065-ms reflection times compared to the near-angle inversion in the area around well 9-17. However, in model-based inversion, it showed higher impedance at far angles in the same well (Figures 3.2.9 and Figure 3.2.13). To investigate this effect, I took additional impedance slices at 1070 ms time depth which confirmed the lower impedance values in band-limited, far-angle inversion (Figure 4.9). In addition, the slices confirmed the low impedance of the sand reservoir in the channel, as indicated by the ellipses Figure 4.9. This low impedance is surrounded by high impedances of the Mississippian carbonates (Figures 4.9 and 4.10).
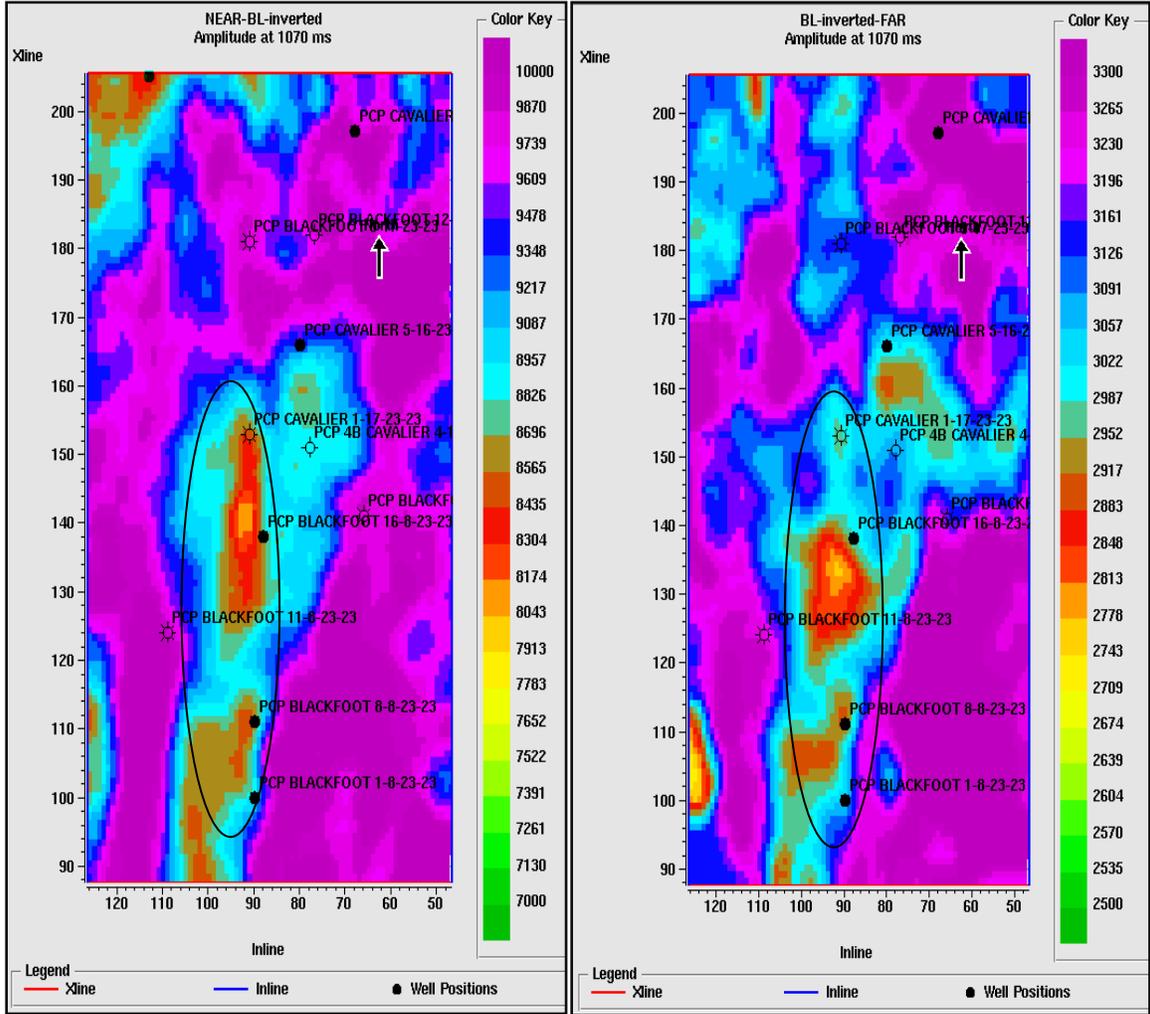
Figure 4.9. Near-offset (left) and far-offset (right) Elastic Impedance slice at 1070 ms time depth using the band-limited inversion. The low-impedance areas in the channel are indicated by ellipses.
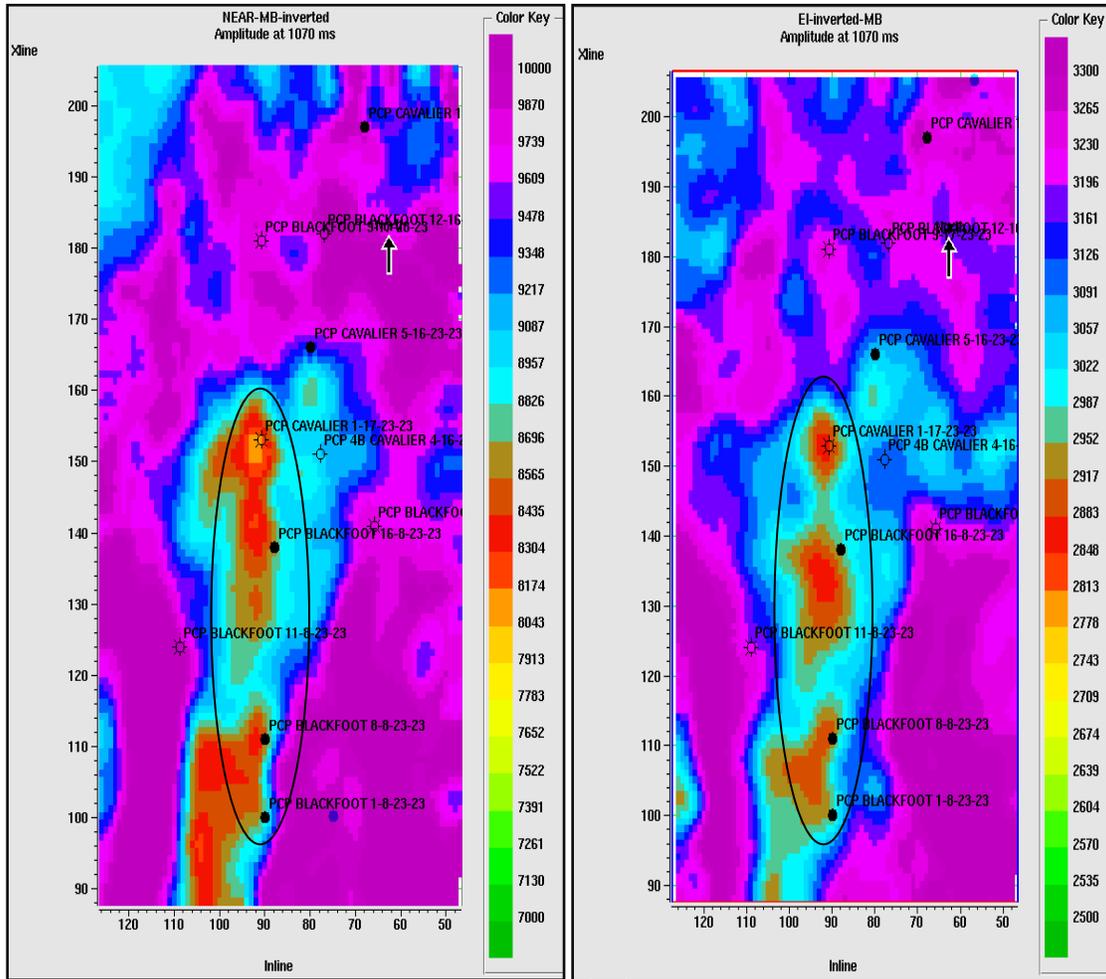
Figure 4.10. Elastic impedance slice at 1070 ms time depth using mode-based, near (left) and far (right). The low-impedance zones in the channel are seen clearly (ellipses).

In the **Simultaneous Inversion,** we inverted for Z_P and Z_S and ignored the density variations (judging them unrecoverable as a result of the narrow angular coverage of CMP gathers). The RMS data errors (Figure 3.3.4) are lower compared to those of the post-stack inversion. However, a comparison of the inversion results to the real logs is not quite satisfactory. The reasons for this is likely that our CMP gathers have comparatively low resolution which does not allow capturing the details of such a thin reservoir clearly, as well as to

119

measure the coefficients that are used for background relationship (eqs. 2.4.3 and 2.4.4) more accurately. Nevertheless, the method still shows a good result for Z_P and Z_S, especially at the gas well 1-17, as shown in Figure 3.3.5.

Cross-sections zoomed in around the gas well are shown in Figure 4.11. Note the difference between the P- and S-impedance sections in this Figure. The S-wave impedance shows relatively high impedance compared to the P-wave impedance, because the shear wave velocity slightly increases within a hydrocarbon reservoir, unlike the compressional wave, whose velocity decreases dramatically within a gas reservoir (Gassmann, 1951).
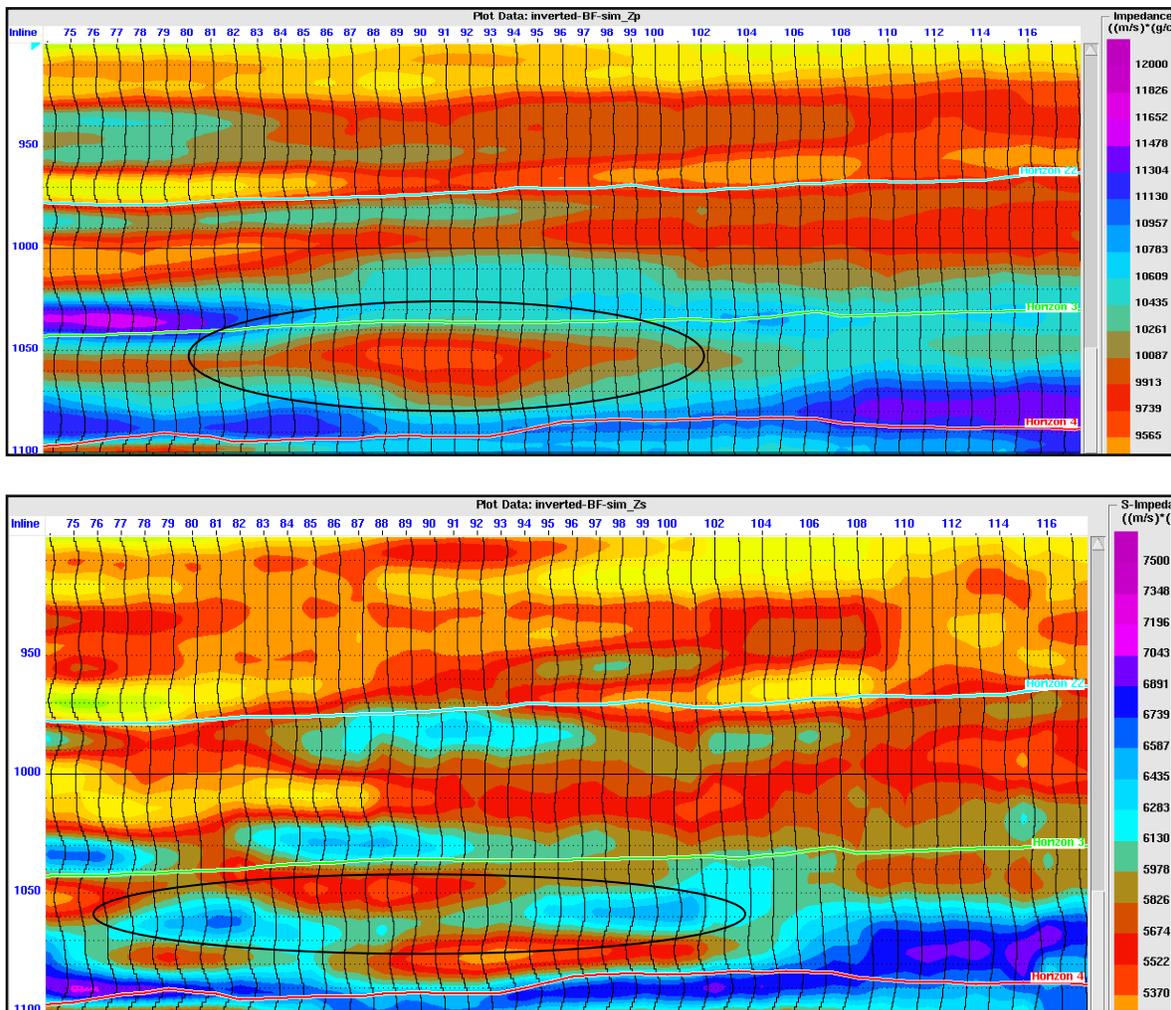
Figure 4.11. *P*-**impedance (top) and** *S*-**impedance (bottom) near the gas reservoir. Ellipses indicate the zone of low** *P*-**impedances related to the gas reservoir (above) and relatively high** *S*-**impedance (bottom).**

The RMS impedance distributions averaged within 10-ms time windows centred at 1065 ms (Figure 3.3.7) showed that the simultaneous inversion resulted in higher P-impedance (Z_P) values compared to those derived from post-stack AI inversion (Section 3.1) in the channel area. The S-impedance is quite high within the channel, except around the gas well 1-17. An additional impedance slice was also taken at 1070-ms time-depth (Figure 4.12) to illustrate these differences.

Summarizing the AI and EI results, pre-stack inversion (EI) results appear not as satisfactory as those of the post-stack (AI) inversion. Several reasons may have caused this deficiency. First, narrow angular apertures (relatively deep reservoir and short source-receiver offsets) and seismic data quality (such as the limited bandwidth) limit the data resolution of any inversion. Second, as this study showed, inversion results depend on the types of algorithms and initial models used. The most high-resolution and model-independent post-stack algorithm (SILC) is still not available for pre-stack data. Therefore, it is likely that with its extension to pre-stack inversion and EI, this situation may change. Third, only standard seismic processing was employed in this study, and potentially there may exist ways to improve the data quality and to produce higher resolution. For example, the residual surface-consistent static correction in ProMAX gave unsatisfactory results and was excluded from the processing sequence. Paucity of well-log data may be another reason, especially of the S-wave logs, which were utilized to calculate the inversion coefficients $.k, k_c, m$ and m_c. There are only two S-wave logs within the study area, and both with limited depth ranges. This could lead to inaccurate inversion coefficients, and consequently insufficiently inaccurate results. Pre-stack inversion is also stronger affected by the errors in NMO velocities and by the presence of intra-bed multiples and P/S wave mode conversions.
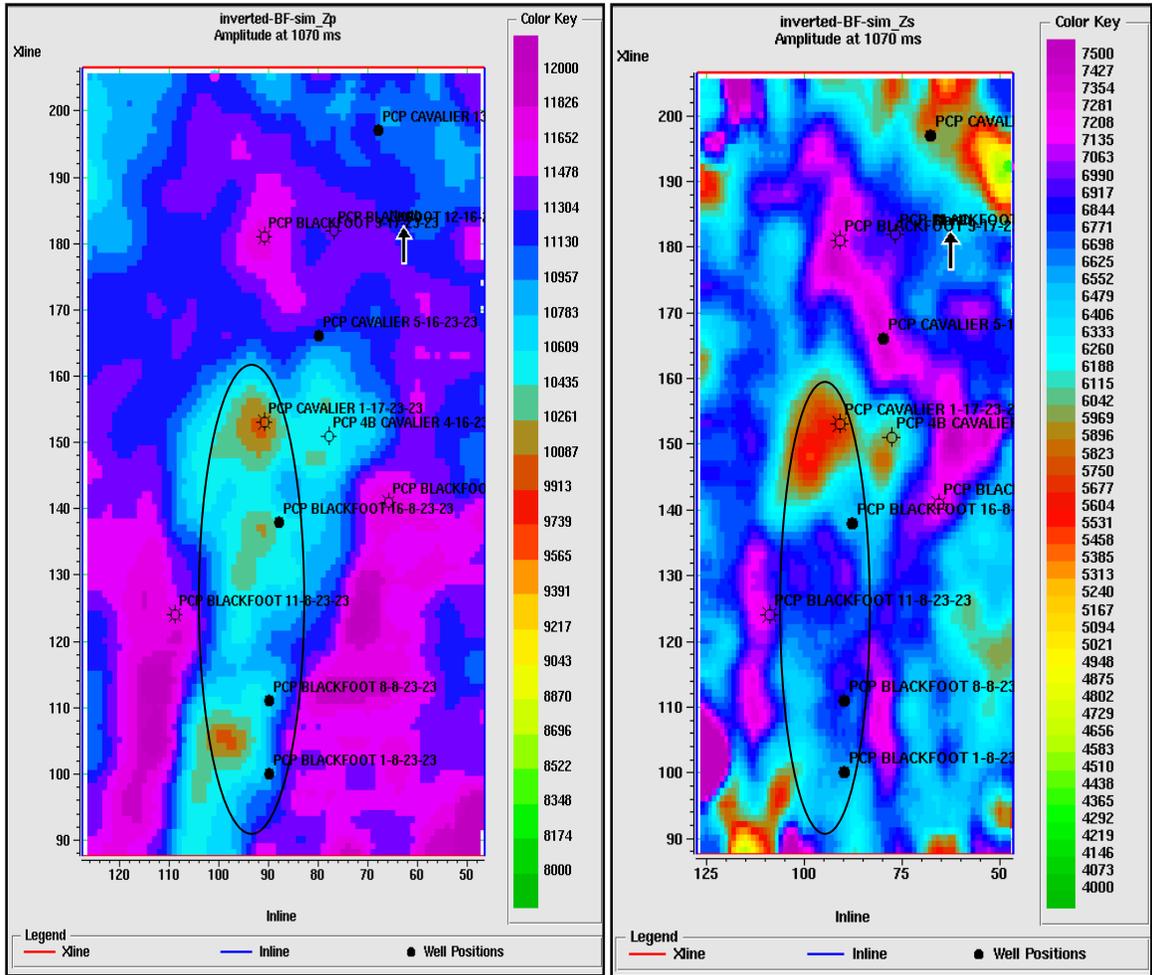
Figure 4.12. *P*-impedance (left) and *S*-impedance (right) slices at 1070 ms time depth. The ellipse indicates the channel. The low *P*-impedance and relatively high *S*-impedance are visible in the channel.

Further, let us consider the **LMR and the V_P/V_S ratio attributes** extracted from the *P*- and *S*-impedances obtained by the simultaneous inversion. As mentioned in the end of Section 2.1, theoretically, the $\lambda\rho$ attribute should be sensitive to pore fluids, whereas $\mu\rho$ is sensitive to the rock matrix. Specifically, we expect to see lower values of $\lambda\rho$ and higher values of $\mu\rho$ within the gas reservoir (Figure 3.4.1 and 3.4.2). Therefore, the sections were zoomed in to show the $\lambda\rho$ and $\mu\rho$ in the vicinity of the gas reservoir (Figure 4.13). Note the low $\lambda\rho$ and high $\mu\rho$ anomalies indicated by the ellipses in the Figure. The corresponding V_P/V_S ratio section is shown in Figure 4.14. As expected, V_P/V_S decrease significantly within these anomalies. The gas-reservoir anomalies are clearly indicated at 1060-ms reflection time.

122
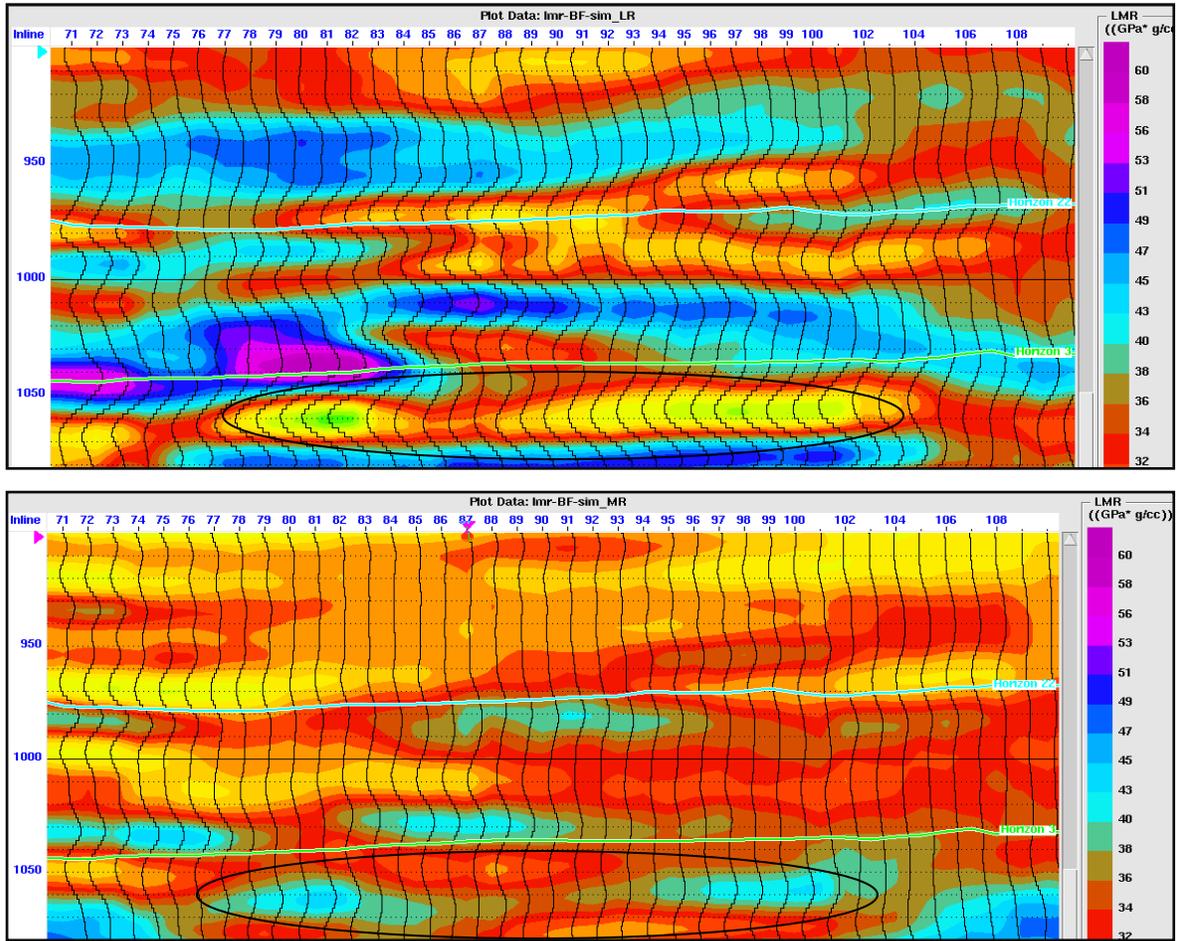
Figure 4.13. $\lambda\rho$ (top) and $\mu\rho$ (bottom) attributes near the reservoir. Ellipses indicate the gas reservoir.
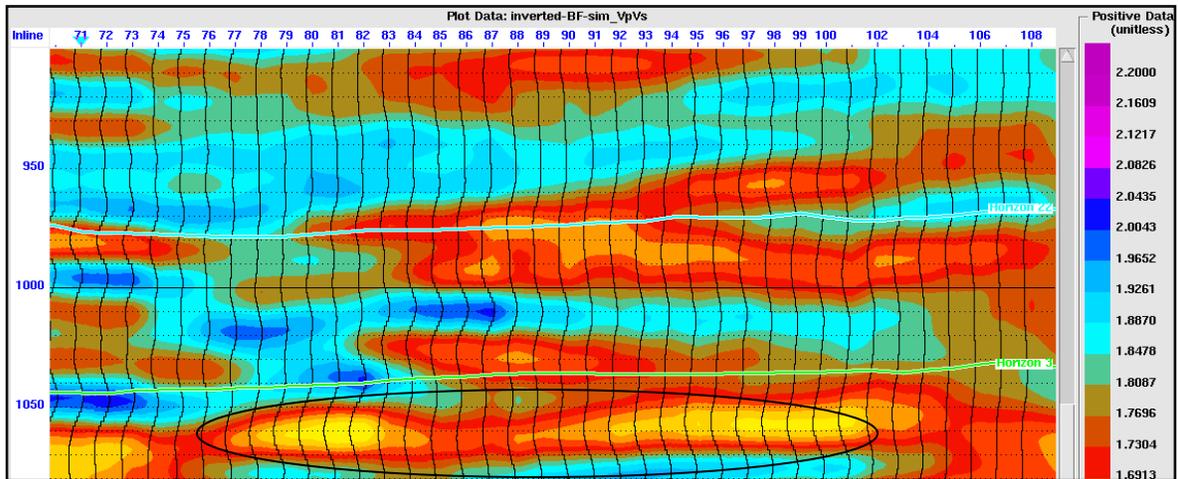
Figure 4.14. V_P/V_S ratios appear to emphasize the reservoir best. Ellipse indicates the gas reservoir.

Slices of the LMR attributes and V_P/V_S ratios show the horizontal distributions of these parameters at the reservoir level (Figures 3.4.3 and 3.4.4). As before, these images show the RMS average taken within the 1060 – 1070-ms time windows. The LMR distributions show a strong decrease in the $\lambda\rho$ values and a large increase in $\mu\rho$, especially within the channel. I also took slices at 1070 ms shown in Figure 4.15 for $\lambda\rho$ and $\mu\rho$ and Figure 4.16 for the V_P/V_S ratios. The $\lambda\rho$, $\mu\rho$ and V_P/V_S anomalies described above show characteristic shapes, likely dominated by the shape of the channel. Note that the $\lambda\rho$, $\mu\rho$ and V_P/V_S anomalies at gas well 1-17 do not show gas reservoir clearly because these slices are located beneath the gas reservoir (Figure 4.15).
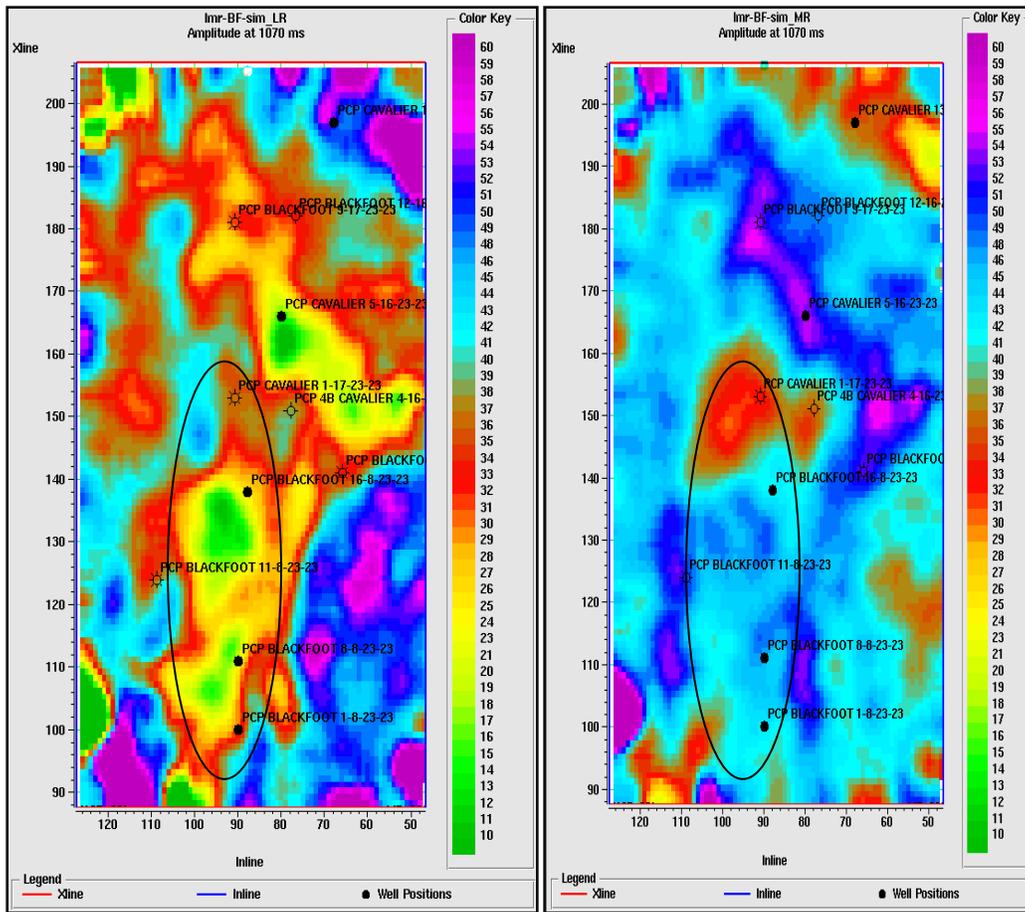
Figure 4.15. Slices of LMR parameters 1070-ms time-depth: $\lambda\rho$ (left) and $\mu\rho$ (right). The ellipses indicate the channel area. The low-$\lambda\rho$ and high-$\mu\rho$ anomalies are shown clearly within the channel.
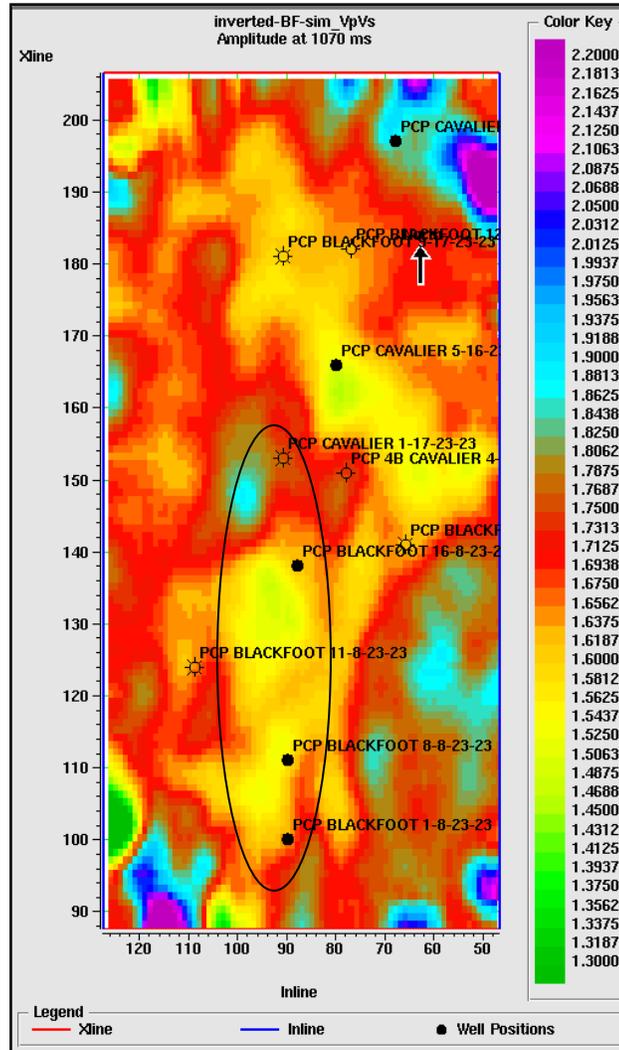
Figure 4.16. V_P/V_S ratio distribution at 1070-ms time-depth. Note the low V_P/V_S ratio within the channel.

Finally, pre-stack CMP gathers were also utilized to create the **AVO attribute volumes** from the seismic data. Here, the complete intercept (*A*) and gradient (*B*) cross-sections are shown in Figure 3.5.2. The section is also zoomed-in onto the reservoir (Figure 4.17). The AVO intercept shows a reasonable result in the section containing the gas well 1-17; however, the gradient seems clearer in showing the top and bottom of the gas in the section. This could be due to the gradient depending on the changes in density, *P*-wave velocity and *S*-wave velocity with offset (angle) while intercept (*A*) controlled by the

125

changes in density, *P*-wave velocity at zero offsets. *P*-wave velocities decrease dramatically in the case of sand gas whereas *S*-wave velocity increases only slightly, leading to increased *B* values.

Several combinations of *A* and *B* are also commonly accepted as AVO attributes (Section 2.1). A snapshot of the AVO product (*AB*) taken in the same section confirmed the gas reservoir very closely (Figure 4.18). When both *A* and *B* have large values the AVO product shows a large positive response at the top and base of the reservoir as indicated in this Figure. The AVO sum (*A+B*), which is approximately proportional to the Poisson's ratio (Section 2.1) shows a negative response at the top of the reservoir (decrease in σ) and a positive response at the base (increase in σ) (Figure 4.19). The third AVO attribute is the AVO difference (*A-B*), which is related to the shear impedance (Z_S). This attribute increases at the top of the reservoir (Figure 4.20). The last extracted attribute is fluid factor (FF), which is related to the deviation from Castagna's wet trend equation at the top and bottom of the reservoir (Section 2.1). The FF is shown in Figure 3.5.10, which is also zoomed in on the reservoir in Figure 4.21. As expected, there appears to be a reasonable deviation of the FF from Castagna's wet trend within the gas reservoir.

In summary, AVO attribute volumes produce reasonable results for the gas reservoir, particularly in the area near the gas well 1-17. However, the results of pre-stack attribute inversions largely depend on the density and apertures of the CMP gathers data, presence of multiples and overall resolution of the seismic data. Unfortunately, it appears that with the present seismic dataset, this data quality was not sufficient enough to give us reliable AVO results for the whole area, and our results are focused on the centre where the angular coverage is the best.
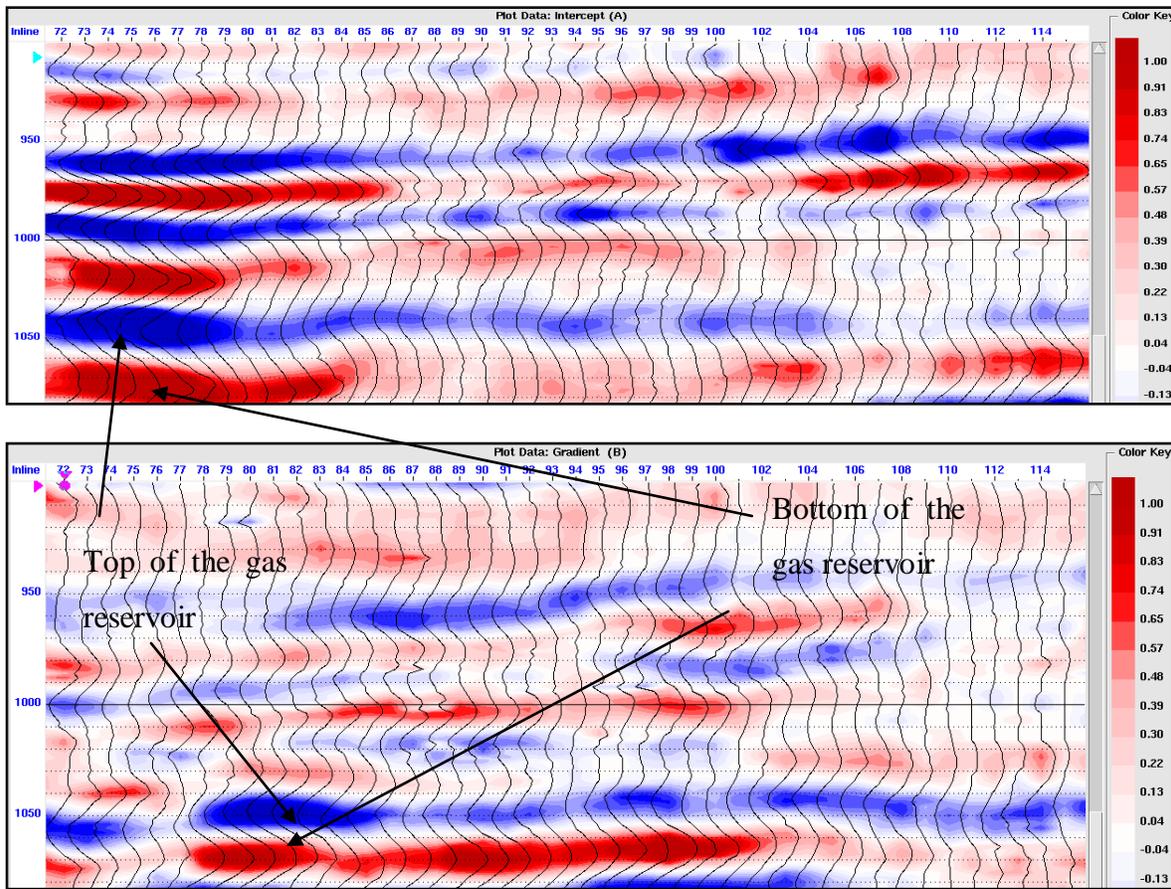
Figure 4.17. The AVO intercept *A* (top) and gradient *B* (bottom) sections indicate the gas reservoir. Note that the gradient appears to show a better result (more localized horizontally) than the intercept.
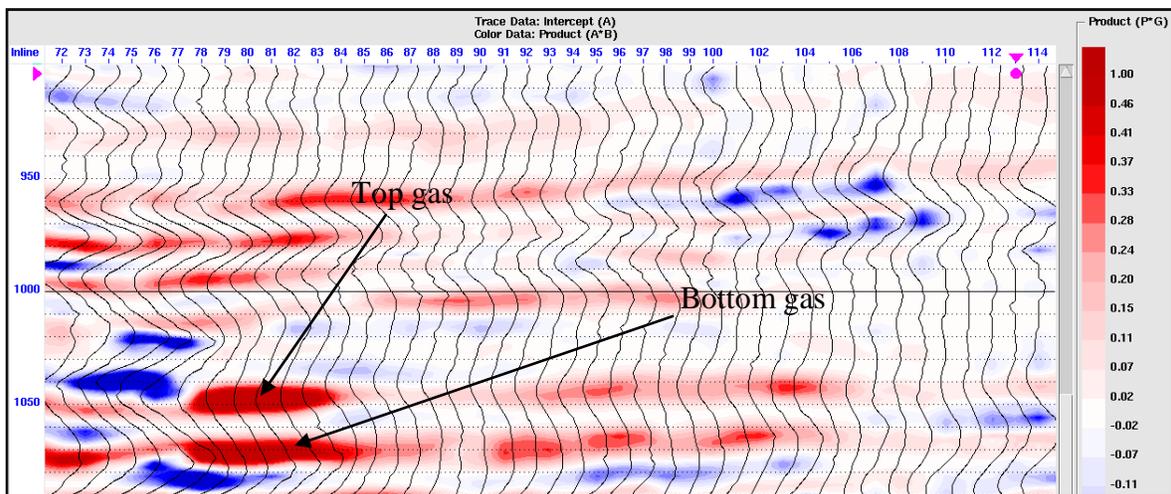
Figure 4.18. AVO product (*AB*) indicates the top and the base of the reservoir.

127
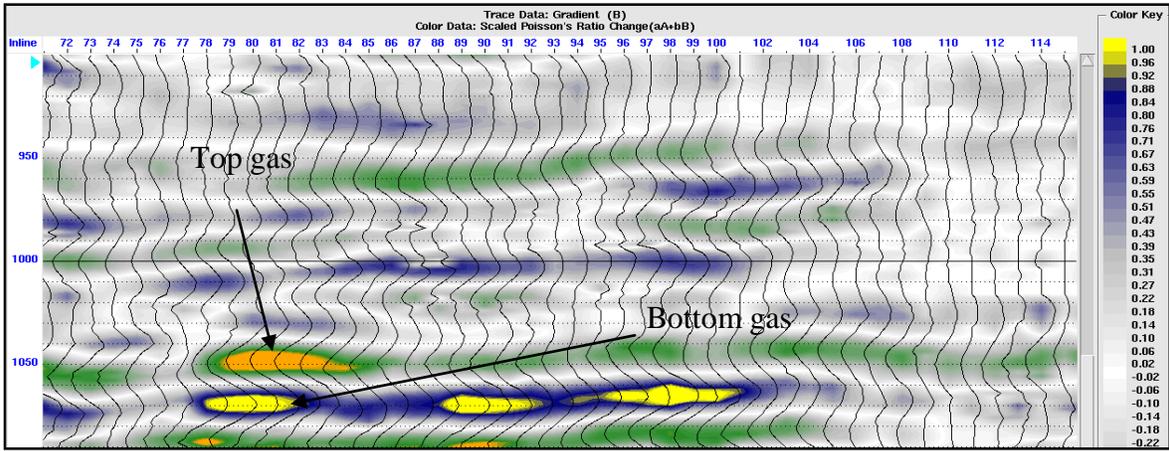
Figure 4.19. Poisson's ratio at the top and base of the gas reservoir.
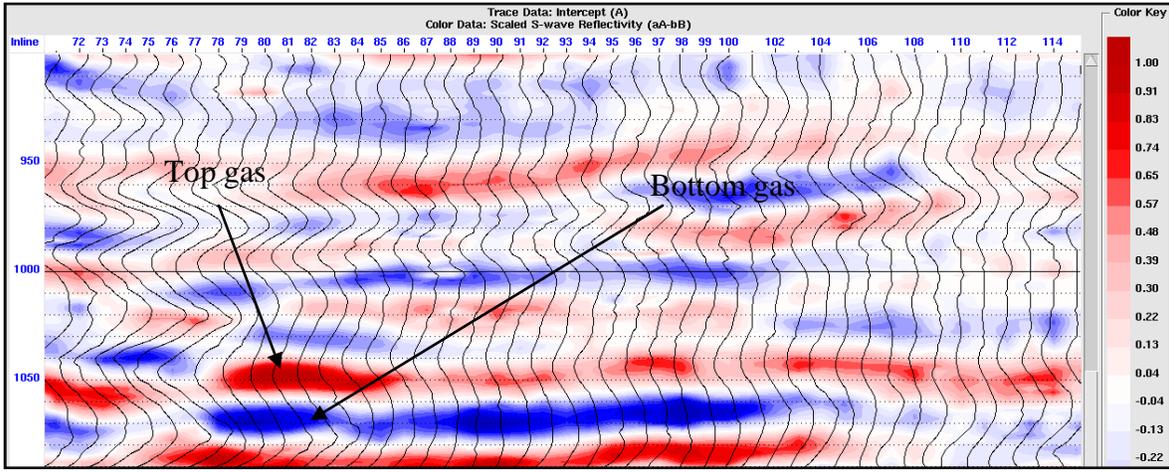
Figure 4.20. *S*-wave reflectivity (*A-B*) indicates the top and bottom of the reservoir.
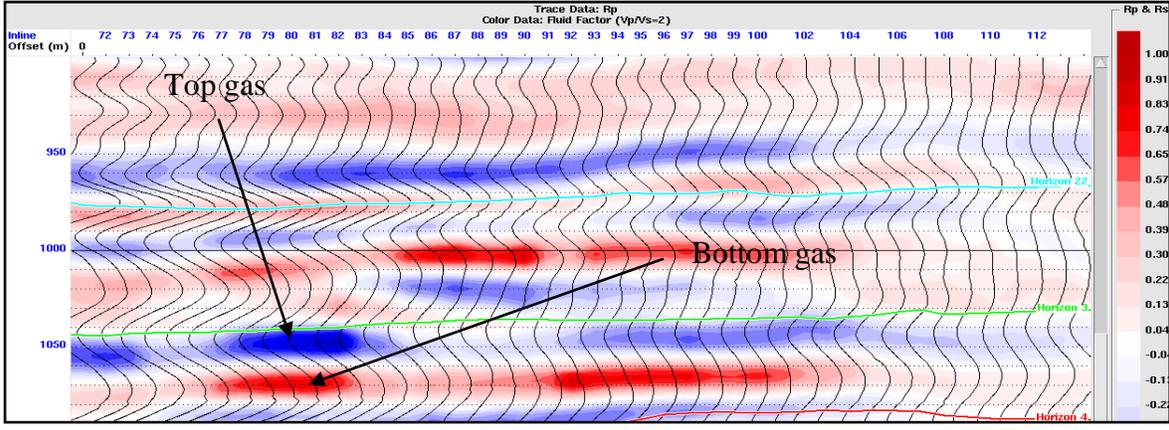
Figure 4.121. Fluid factor (*FF*) indicates the deviation from Castagna's equation at top and bottom of the reservoir.

128

Figure 4.22 show the interpretation of the channel according to a CREWES report (Lawton, 1995). The channel encounters good sand in the south area around well #8-8. In this area, the sand is thicker (around 35 meters) while in the north the plugged shale is encountered in the channel, and the sand is thinner. The images from post-stack inversions (Figures 4.3 and 4.4) show improved results compared to CREWES interpretation (Figure 4.22). The channel in Figures 4.3 and 4.4 shows low impedance values corresponding to the thick hydrocarbon sand in the south area. The impedance in northern part of the study area is higher, likely as a result of plugged shale with sand.

Comparing the performance of the different techniques studied in this Thesis, the Elastic Impedance corroborated most of the results of post-stack inversion: with the southern part of the area showing low impedances while the impedances in the northern part being higher. Simultaneous inversion results were comparatively unsatisfactory in this study, except at the center of the area where the gas reservoir is located. AVO attribute inversion was also satisfactory only at the center of the study area with the best angular coverage and highest CMP fold. However, the V_P/V_S image derived from simultaneous inversion showed clear indication of the gas reservoir in the middle of the study area.

Finally, based on the above interpretations, I considered a question where a hypothetical new well for gas could be drilled in the study area. According the combined post-stack inversion results corroborated by the pre-stack inversions, the best place for a potential gas find would be at the center of low-impedance area south of well # 16-8 (Figures 4.3 and 4.4). In this area, most of the methods studies in this Thesis show low impedance indicating high porosity, and the sand is thicker.
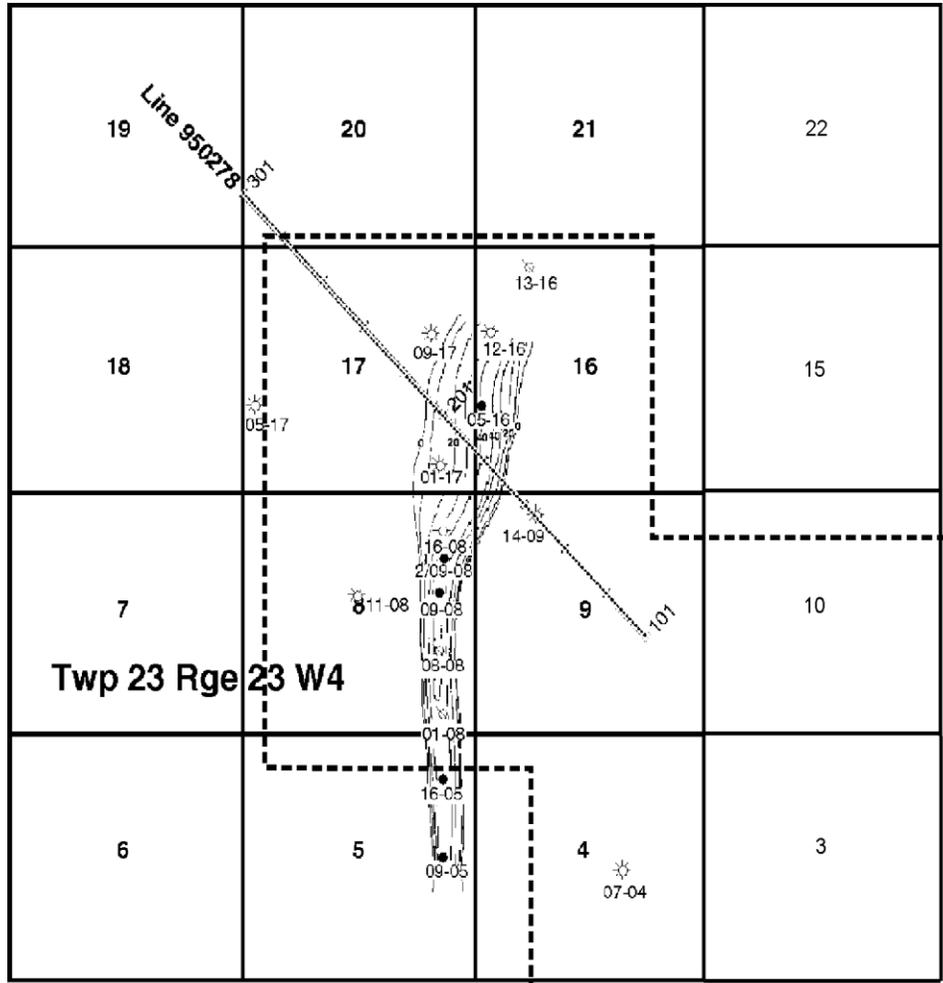
Figure 4. 22. Valley of the Blackfoot area extracted from well information (Lawton, 1995).

4.1   Conclusions

This study used the Blackfoot 3D seismic dataset for comparative analysis of several types of AVO attributes and inversions. The seismic data were processed by using ProMAX seismic processing software. Pre-stack and stacked data were further utilized to perform several types of inversions and to extract a variety of AVO attributes. The final stacked sections showed good images within the time-depth ranges of 1000 to 1200 ms, where the target Glauconitic channel is located.

Post-stack inversion was studied by using four methods, three of which utilized the popular Hampson-Russell (H-R) software, and the fourth (SILC) was included in our in-

130

house package. The results showed that model-based, band-limited and coloured H-R inversion methods give good and mutually consistent results, with low-impedance zones corresponding to the target hydrocarbon sand within the channel. SILC inversion also revealed a low-impedance zone related to the sand in the channel, and demonstrated higher resolution and improved layer consistency. At the same time, SILC inversion resulted in somewhat lower background impedances and suggested that merging the seismic and background models may lead to over-estimated impedances in H-R inversions. Because of this lower average impedance, colour ranges in plotting the SILC images had to be adjusted in order to reveal the details of the reservoir. SILC inversion also better correlated with the RMS amplitude time slices of the original reflection data. In addition, spatial interpolation was performed differently by the H-R and SILC methods, leading to significant differences in reservoir details.

In the Elastic Impedance (EI) inversion, the near-angle inversion results were similar to those of the post-stack inversion (AI). However, the resulting EI values were slightly lower than I expected from published EI interpretations. The far-angle inversion result also showed similar results and did not produce the strong EI anomaly, which was also unexpected. This relative failure of EI was explained by the insufficient angular aperture of the seismic data.

Pre-stack inversion was also applied to the CMP gathers to construct the compressional- and shear-wave impedances (Z_P and Z_S). LMR (λ, μ ρ) attributes and V_P/V_S ratios were subsequently extracted from these impedances. The inversion within the gas channel showed that Z_P was higher than the post-stack AI, even though the inversion still gave good results near the gas well # 1-17 located near the center of the study area and reasonable values at other locations within the channel. LMR results also showed good results near the same well.

AVO attributes were also extracted from the processed CMP gathers. Some of these attributes also allowed a good discrimination of the reservoir near well # 1-17. In particular, the AVO product (*AB*), Poisson's ratio (*A+B*) and fluid factor (FF) attributes were effective in delineating the top and bottom of the gas in this area. The other attributes also showed reasonable behaviours in the same section. However, generally, it appears that the AVO attributes suffered from the same limitations as the pre-stack EI inversion, and they

were successful only in the center of the study area where the angular coverage was the best.

In an overall conclusion, post-stack inversion produced the best results suitable for provisional "targeting" a gas well. Since this method confirm reservoir in the channel area clearly and comparable to the CREWES result (Lawton, 1995). Pre-stack methods suffer from the limited quality of the seismic data as well as from paucity of well-log data. The new SILC method showed good, high-resolution, yet unfortunately distinctly different results in comparison to the other post-stack methods. It appears that this approach needs to be further substantiated in other applications and may be very promising in extending to pre-stack inversion.

4.2 Suggestions for future research

Several ways for extending this study and particularly for improving the pre-stack results can be suggested. First, the SILC approach (Morozov and Ma, in press) can be extended to pre-stack analysis. In combination with other advanced current studies of the impedance such as the exact "Zoeppritz" Elastic Impedance and the full *P/S* impedance (Morozov, in press), this method could offer great improvements in pre-stack inversion. As this approach is robust, almost entirely data-driven, and provides high-resolution images, it holds good promise for improved pre-stack attribute analysis.

As illustrated by the results of this study, the methodology of seismic inversion and attribute interpretation still needs additional investigations and improvement. My comparison of the three popular post-stack inversion schemes to SILC suggested that although generally mutually consistent, they differ in some important detail of the images. In addition, they differ significantly from SILC, which is much less dependent on algorithmic nuances. These differences increase away from the wells, showing that spatial interpolation also has a significant impact on the impedance solutions. This suggests that initial models and algorithms still determine much of the inverted images, and methods need to be sought for making the inverse models less dependent on the subjective parameters of the algorithms. Once again, one possible approach to this appears to be SILC (Morozov and Ma, in press).

By using new methodologies, principally new AVO impedance attributes can also be derived. For example, (Morozov, in press) recently proposed a new definition of the exact *P/S* impedance which represents a true medium property. This impedance is of a matrix form and incorporates the *P-* and *S*-wave reflections and mode conversions. It is also accurate and does not rely on the traditional approximations to the Zoeppritz equations and summations of reflectivity series. This accurate form of impedance should be particularly advantageous with 3C data.

Another significant enhancement could be achieved with Blackfoot 3D-3C data would be by using the horizontal-component records. In the present study, only the vertical-component data were used in combination with a fairly conventional seismic processing sequence. Full 3C processing requires rotation of the horizontal components, 3C surface-consistent deconvolution and amplitude calibration, and removal of the near-surface reflection and *P/SV* conversion effects. Such operations are difficult with the conventional software, such as Halliburton ProMAX used in this study. Progress in the direction of consistent 3D-3C seismic processing and inversion is also being made in our group (e.g., Morozov and Gao, 2009), and such analysis should become feasible in the near future.

Improved seismic waveform processing to increase its resolution could also help imaging the thin Blackfoot reservoir. A more accurate determination of the seismic wavelet should lead to improved resolution of the inversion and all attributes. Also, a more precise suppression of multiples and mode conversions (compared to the present NMO correction and CMP stacking) could improve the correspondence of the wavefield to the convolutional model used in inversion.

REFERENCES

Aki, K., and Richards, P., 2002. Quantitative seismology: theory and methods,, Second Edition, University Science Books, Sausalito, CA.

Connolly, P., 1999. Elastic impedance. The Leading Edge, 18, 438-452.

Castagna, J. P., Batzle, M. L., and Eastwood, R, L., 1985. Relationships between compressional-wave and shear-wave velocities in clastic silicate rocks Geophysics, 50, 571-581.

Castagna, P. J., and Smith, S. W., 1994. Comparison of AVO indicators: A modeling study. Geophysics, 59, 1849-1855.

Castagna, J. P., Swanz, H. W., and Foster, D. J., 1998. Framework for AVO gradient and intercept interpretation. Geophysics, 63, 948-956.

Fatti, J. L., Smith, G. C., Vail, P. J., Strauss, P. J., and Levitt, P. R., 1994. Detection of gas in sandstone reservoirs using AVO analysis: A 3-D seismic case history using the Geostack technique. Geophysics, 59, 1362-1376.

Gassmann, F., 1951. Elastic waves through a packing of spheres: Geophysics, 16, 673-685.

Gardner, G. H. F., Gardner, L.W., and Gregory, A. R., 1974. Formation velocity and density - The diagnostic basics for stratigraphic traps, Geophysics, 39, 770-780.

Goodway, B., Chen, T. and Downton, J., 1997. Improved AVO fluid detection and lithology discrimination using Lamé petrophysical parameters; ``lambda rho'',``mu rho'',&``lambda/mu fluid stack'', from P and S inversions, SEG Expanded Abstracts 16, 183-186.

Gulati, J. S., Stewart, R. R., Peron, J., and Parkin, J. M., 1997. 3C-3D VSP: Normal moveout correction and VSPCDP transformation. CREWES Research Report- 9

Lawton, D. C., 1996. Design review of the Blackfoot 3C-3D seismic program. CREWES Research Report –38.

Lawton, D.C., Stewart, R. R., Cordsen, A and Hrycak, S, 1995. Advances in 3C-3D design for converted waves. CREWES Research Report –43.

Larsen, J. A., Margrave. G. F., Lu, H., and Potter, C. C., 1998. Simultaneous P-P and P-S inversion by weighted stacking applied to the Blackfoot 3C-3D survey. CREWES Research Report – 50

Lindseth, R. O., 1979. Synthetics sonic logs- a process for stratigraphic interpretation: Geophysics, 44, 3-26.

Lancaster, S., Whitcombe, D., 2000. Fast-track 'coloured' inversion. SEG Expanded Abstracts, 19, 1572-1575.

Ma, J., 2003. Forward modeling and inversion methods based on generalized elastic impedance in seismic exploration. Journal of Chinese Geophysics, 46,159-168.

Margrave, G. F., Lawton, D. C., Stewart, R. R.. 1998. Interpreting channel sands with 3C-3D seismic data. The Leading Edge, 17,509-513.

Martins, J. L., 2006. Elastic impedance in weakly anisotropic media, Geophysics, 71, D73-D83.

Morozov, I. B., and Ma, J. in press, Accurate post-stack acoustic impedance inversion by well-log calibration, Geophysics, in press.

Morozov, I. B., and Gao, L., 2009. Pre-stack calibration of 3-C 3-D time-lapse seismic data, 2009 CSPG/CSEG/CWLS Convention, May 4-6, 2009, Calgary, AB.

Morozov, I. B., Exact Elastic P/SV impedance, Geophysics, in press..

Miller, S. L. M., Aydemir, E. O., and Margrave, G. F., 1995. Preliminary interpretation of P-P and P-S seismic data from the Blackfoot broad-band survey. CREWES Research Report-42.

Ostrander, W. J., 1982. Plane wave reflection coefficients for gas sands at non-normal angles of incidence: SEG Expanded Abstracts, 1, 216-218.

Pendrel, J, 2006, Seismic inversion- Still the best tool for reservoir characterization, CSEG, Recorder, 5-12.

Rutherford, S. R., and Williams, R. H., 1989, Amplitude-versus-offset variations in gas sands: Geophysics, 54, 680–688.

Russell, B., and Hampson, D., 1991. Comparison of Poststack Seismic Inversion Methods, SEG Expanded Abstracts,10, 876-878.

Russell, B., 1988, Introduction to seismic inversion methods: The SEG course notes Series, 2.

Santos, L. T. and Tygel, M., 2004. Impedance-type approximations of the P–P elastic reflection coefficient: Modeling and AVO inversion. Geophysics, 69, 592-598.

Sheriff, R.E., and Geldart, L. P, 1995. Exploration Seismology. Cambridge ; New York : Cambridge University Press, 1995, 592.

Shuey, R.T., 1985, A simplification of the Zoeppritz equations: Geophysics, 50, 609-614.

Smith, G. C., and Gidlow, P. M., 1987. Weighted stacking for rock property estimation and detection of gas: Geophysical Prospecting, 35, 993-1014.

Simin, V., Harrison, M. P., and Lorentz, G. A., 1996. Processing the Blackfoot 3C-3D seismic survey. CREWES Research Report-39.

Simin, V., Margrave, G. F., and Yang, G. Y.C., 1996. AVO measurements for P-P and P-S data in the Blackfoot 3C-3D dataset. CREWES Research Report-42.

Singh, Y., 2007, Lithofacies detection through simultaneous inversion and principal component attributes. The Leading Edge, 26,1568-1575.

Stewart, R. R., Gaiser, J. E., Brown, R. J., and Lawton, D. C., 1999. Converted-wave seismic exploration: a tutorial. CREWES Research Report -3.

VerWest, B., 2004, Elastic Impedance revisited, 66th EAGE Conference and Exhibition Extended Abstracts, Paris, France, P342.

VerWest, B., Masters, R., and Sena, A., 2000. Elastic impedance inversion: 70th Ann. Intern. Mtg. Soc. Expl. Geophys. Expanded Abstracts, 1580-1582.

Whitcombe, D. N. 2002. Elastic impedance normalization, Geophysics, 67, 60-62.

Whitcombe, D. N., Connoly, P., Reagan, P. L., and Redshaw, T. C., 2002. Extended elastic impedance for fluid and lithology prediction, Geophysics, 67, 63-67.

Wiggins, R., Kenny, G.S., and McClure, C.D., 1983. A method for determining and displaying the shear-velocity reflectivities of a geologic formation: European patent Application 0113944.

Xu, Y and Bancroft, J. C., 1997. Joint AVO analysis of PP and PS seismic data CREWES Research Report -34.

Yalmaz, O., 2006. Seismic data analysis: processing, Inversion and Interpretation of seismic data: Society of exploration geophysics. 1793-1999.

Zhang. Q., Stewart, R. R., Parkin, J. M., and Sun. Z., 1996. Analysis of the Blackfoot 3C-3D VSP survey. CREWES Research Report-40.